UC Irvine

UC Irvine Electronic Theses and Dissertations

Title

Ice grounding zone processes in Antarctica from satellite SAR interferometry and other data

Permalink

https://escholarship.org/uc/item/9xg934d5

Author

Chen, Hanning

Publication Date

2024

Copyright Information

This work is made available under the terms of a Creative Commons Attribution-NonCommercial License, available at https://creativecommons.org/licenses/by-nc/4.0/

Peer reviewed|Thesis/dissertation

eScholarship.org Powered by the California Digital Library
University of California

UNIVERSITY OF CALIFORNIA,
IRVINE

Ice grounding zone processes in Antarctica from satellite SAR interferometry and other data

DISSERTATION

submitted in partial satisfaction of the requirements
for the degree of

DOCTOR OF PHILOSOPHY

in Earth System Science

by

Hanning Chen

Dissertation Committee:
Professor Eric Rignot, Chair
Professor Francois Primeau
Professor Isabella Velicogna

2024

Chapter 2 © 2023 American Geophysical Union
All other materials © 2024 Hanning Chen

DEDICATION

To those who support and accompany me.

TABLE OF CONTENTS

Page

LIST OF FIGURES **v**

ACKNOWLEDGMENTS **ix**

VITA **x**

ABSTRACT OF THE DISSERTATION **xiii**

1 Introduction **1**
- 1.1 Background . . . 3
  - 1.1.1 Grounding line migration . . . 3
  - 1.1.2 Ice grounding zone mapping . . . 5
  - 1.1.3 Ice dynamics . . . 8
  - 1.1.4 Glacier mass balance . . . 10
  - 1.1.5 Ice shelf basal melting . . . 12
- 1.2 Dissertation objectives . . . 13
- 1.3 Chapter overviews . . . 14

2 Grounding zone of Amery ice shelf, Antarctica, from differential synthetic-aperture radar interferometry **16**
- 2.1 Abstract . . . 16
- 2.2 Introduction . . . 17
- 2.3 Data and Methods . . . 19
  - 2.3.1 Sentinel-1 interferogram . . . 19
  - 2.3.2 Tide model and atmospheric pressure . . . 21
  - 2.3.3 Surface, bed and thickness slopes . . . 21
  - 2.3.4 Grounding zone length from flotation . . . 22
  - 2.3.5 Subglacial channels . . . 22
- 2.4 Results . . . 22
  - 2.4.1 Grounding line migration and seawater intrusion . . . 22
  - 2.4.2 Grounding zone length and slopes . . . 24
- 2.5 Discussion . . . 28
- 2.6 Conclusions . . . 31

3 Rapid retreat of Berry Glacier, West Antarctica, from satellite radar interferometry and other data **32**
3.1 Abstract . . . 32
3.2 Introduction . . . 33
3.3 Data and Methods . . . 34
3.3.1 Double-difference interferogram . . . 34
3.3.2 Tidal height calculation and correction . . . 37
3.3.3 Grounding zone length from hydrostatic equilibrium . . . 38
3.3.4 Ice velocity and surface height data . . . 38
3.3.5 Ice mass balance calculation . . . 39
3.3.6 Ice bottom and bed topography . . . 39
3.3.7 Ice basal melt rates . . . 40
3.4 Results . . . 41
3.4.1 Grounding line migration . . . 41
3.4.2 Ice dynamics . . . 43
3.4.3 Implications for bed topography . . . 45
3.4.4 Basal melting regime . . . 47
3.5 Discussion . . . 48
3.6 Conclusions . . . 50

4 Melt rates in the kilometer-size ice grounding zone of Amery ice shelf, East Antarctica **51**
4.1 Abstract . . . 51
4.2 Introduction . . . 52
4.3 Data and Methods . . . 56
4.3.1 Ice grounding zone mapping . . . 56
4.3.2 Ice velocity . . . 56
4.3.3 Ice melt rates . . . 56
4.4 Results . . . 57
4.4.1 Ice grounding zones . . . 57
4.4.2 Basal melting and ice dynamics . . . 57
4.5 Discussion . . . 62
4.6 Conclusions . . . 63

5 Conclusions **65**
5.1 Summary of results . . . 65
5.1.1 Chapter 2 main findings . . . 67
5.1.2 Chapter 3 main findings . . . 67
5.1.3 Chapter 4 main findings . . . 68
5.2 Future outlooks . . . 69

Bibliography **71**

Appendix A Supplemental Information: Rapid retreat of Berry Glacier, West Antarctica, from satellite radar interferometry and other data **81**

LIST OF FIGURES

Page

1.1 **Diagram of the grounding line.** The grounding line (GL), where ice on land meets the ocean and begins to float, is retreating or will retreat in many regions of Antarctic Ice Sheet, primarily because of ocean-induced melting under floating ice shelves. GL retreat is governed by the interplay among ocean circulation, ice dynamics, and bed topography. This figure was taken from NSIDC, NASA. 4

1.2 **Grounding line position from DInSAR interferometric fringes.** Ice grounding zone of Petermann Glacier, Greenland, with the limit of tidal flexing (F), the grounding line (G), the line of first hydrostatic equilibrium (J), the break in surface slope (I), the maximum extent of the flexure zone (H), ice surface elevation above mean sea level from laser altimetry (thin black line), bed topography from radio echo sounding (thick black line), bed depth calculated from hydrostatic equilibrium (dashed black line), the unknown seafloor (over-deepening likely exceeds 800 m) and tidal flexing measured with ERS-1 DInSAR in millimeter of vertical motion (red thick line). The color inset on top shows the DInSAR interferometric fringes, color coded from 0 and 2π, from blue to yellow, red and blue, and delineates F (dotted white line near G), G (white line), and H (dotted white on floating ice). Ice flows from left (grounded ice) to right (floating ice). This figure was taken from Rignot et al. (2011). 6

1.3 **Grounding line delineation from deep learning.** Different steps of the pipeline for (a) a sample interferogram with hand-drawn grounding line in white; (b) output of the neural network in raster format with a variable width that is a measure of uncertainty of the output. The gray mask in the background represents training (white) and testing (gray) sites; (c) Vectorized output and uncertainty contours; (d) zoomed-in region highlighted by the maroon box in panel (c) showing both manual and ML results and uncertainty bars; (e) Comparison of the manual and ML performances in the area outlined in blue in panel (c). The interferograms are obtained from Sentinel-1a/b data in 2018. This figure was taken from Mohajerani et al. (2021). 7

1.4 **Ice dynamics of Antarctica.** (A) Ice speed of the Antarctic Ice Sheet derived from multisensor data for the time period 2014–2016 with 18 subregions A–K (black thin lines) delineated from surface slope and ice flow direction data. (B) Change in flow speed from the time period 2007–2008 to 2014–2015. Grey areas have no data. (C) Change in grounding line ice discharge, D, for 1979–2017 for the 18 major subregions in billions of tons per year with percentage change in speed and circle radius proportional to change. (D) Total change in mass of major basins for 1979–2017 with circle radius proportional to the absolute mass balance. This figure was taken from Rignot et al. (2019). 9

1.5 **Ice mass balance of Antarctica.** Ice mass balance of Antarctica using the component method (SMB, on grounded ice minus ice discharge, D, at the grounding line) for (A) 1979-1990, (B) 1989-2000, (C) 1999-2009, and (D) 2009-2017. The size of the circle is proportional to the absolute magnitude of the anomaly in D ($\delta D = SMB_{1979-2008}$ - D) or SMB ($\delta SMB = SMB$ - $SMB_{1979-2008}$). The color of the circle indicates loss in δD (dark red) or δSMB (light red) versus gain in δD (dark blue) or δSMB (light blue) in billions of tons (10^{12} kg) per year. Dark color refers to δD; light color refers to δSMB. Plots show totals for Antarctica, Antarctic Peninsula, West Antarctica, and East Antarctica. Background is the total mass balance spread into the drainage basins. This figure was taken from Rignot et al. (2019). 11

2.1 **Grounding line positions of Amery Ice Shelf, East Antarctica.** (a) 68 GL positions (black) of the Lambert, Fisher and Mellor glacier system, Amery Ice Shelf in year 2018 from S1 DInSAR data and one reference GL (white) in year 1996 from ERS-1/2 data [72] overlaid on the BedMachine bed topography [53]. Star in the inset map of ice speed denotes the location where tidal height is calculated; (b) grounding zone (red) in year 2018 overlaid on a map of height above flotation. Double-difference interferograms for the most c) upstream d) downstream positions of the GL (black line) overlaid on radar brightness; (e-f) tidal height (red dot) at the time of acquisitions used to form the interferograms in (c-d). 20

2.2 **Grounding line migration of Amery Ice Shelf, East Antarctica.** (a) Grounding zone (red) and location of 7 profiles (blue) along Lambert Glacier (LG), Lambert estuary (LE), Mellor estuary (ME), Mellor Glacier (MG), Fisher Glacier South (FGS), Fisher Glacier (FG), and Fisher Glacier North (FGN) overlaid on BedMachine bed topography starting at the black dot. Inset chart compares observed IGZ length versus modeled from flotation; (b) water column thickness within the IGZ in Fig. 2.1c; (c) modeled differential tidal height versus observed with interferometry. GL position versus (d) maximum tidal height during the 3 to 4 acquisition times at LE, ME, MG, and FG profiles and (e) versus time. 25

2.3 **Grounding zone length versus bed, surface, and thickness slopes.** (a-c) Comparison of IGZ length versus bed, surface, and thickness slopes using BMv2; (d-j) surface, ice draft, and bed elevations along the seven profiles with IGZ boundary (red dotted line) and domain of calculation of slopes (black dotted line). For bed elevation, we separate areas where mass conservation has been applied (brown solid) versus bed elevation from IBCSO2 (brown dotted). 27

3.1 **Grounding line from machine learning covering Antarctica.** Antarctic grounding line delineation (yellow) from machine learning with Sentinel-1 double-difference InSAR in year 2019. 35

3.2 **Grounding line positions of Berry Glacier, West Antarctica.** (a) 88 GLs (location in inset) from year 1996 (white) from ERS-1/2, 2008 (blue)/2009 (cyan) from ALOS-2 PALSAR, 2019 (yellow) from Sentinel-1, and 2020 (orange)/2021 (red) from CSK radar interferometry overlaid on bed topography from BedMachine v3.7 (outside IGZ) [53] and derived from a WorldView DEM (inside IGZ) assuming flotation color coded from -2000 m (blue) to 0 m (white). Star in inset shows where we calculate tides [61] and inverse barometer effect. Black lines are Operation IceBridge (OIB) tracks from 2011-2016. Pink lines are flux gates for ice discharge. White dash lines delineate the drainage basin. (b-d) CSK-derived GL positions (black line) between three states; (e-g) SSH (red dot) at the time of acquisitions in (b-d). Insets shows SSH 12 hours prior and after the 3 (to 4) acquisition times. 36

3.3 **Grounding line migration of Berry Glacier, West Antarctica.** (a) GL density and IGZ (red dotted line) in 2019-2021 and center flowline (green) overlaid on bed topography; (b) Sentinel-1 double-difference InSAR with GL position (black) and deformation fringes upstream revealing that water trapped in the previous cycle is moving out; (c) modeled differential SSH versus InSAR observations; (d) GL position versus maximum SSH for three states during the 3 (to 4) acquisition times. 42

3.4 **Spatial and temporal changes in surface elevation, h, and speed, V, of Berry Glacier, West Antarctica.** (a) h and (b) V between 2006 and 2022 with GLs in 1996 (white)/2008 (blue)/2009 (cyan) and IGZ boundaries in 2019 (yellow)/2020 (orange)/2021 (red). Year 2006 is the reference for (a-b); (c,d) h along profiles G-H and C-D from 1996 to 2022 with IGZ boundaries (vertical and horizontal bars); (e,f) V along profiles G-H and C-D for year 1996 to 2022 (gaps in 1997-2005, 2007 and 2013). 44

3.5 **Cumulative anomalies in ice discharge (D), surface mass balance (SMB), and mass balance (M) of Berry Glacier, West Antarctica from 1996-2022.** (a) Annual anomalies in D, SMB and M with error bars in gigatons. Linear interpolation is used to fill discharge gaps (dashed) in 1997-2005, 2007 and 2013; (b) cumulative anomalies in D, SMB and M for 1996-2022. The balance discharge is $SMB_{1979-2004} = 4.3 \pm 0.2$ Gt/yr. 45

3.6 **Surface elevation, h, and bed topography, b, along the profiles.** (a,b) h (grey line) from WorldView (WV) (a) and Airborne Topographic Mapper (ATM) (b), ice draft (blue line) deduced from WV (a) and a DEM (b), and bed elevation, b (brown line) from BMv3.7 along G-H and C-D. Blue dash line marks flotation from ICESat-2 on Jan 1, 2020; blue solid line is ice bottom deduced, respectively, from WV on Sep 6, 2019 (a) and a DEM from ICESat-2 (b); dark blue line is ice bottom deduced from ATM in 2012 (b); blue dot is ice bottom from OIB. Dots in (a) are respectively for Nov 5, 2016 (state 1), Oct 27, 2012 (near state 2), Nov 2, 2016 (between states 2 and 3, and outside IGZ) and Oct 17, 2011 (state 3). Acquisition time of the dots in (b) is Oct 27, 2012 as well. 46

3.7 **Height-change rate, $\partial h/\partial t$, and basal melt rate, $\dot{b}$, of Berry Glacier, West Antarctica from 2019-2022.** (a) $\partial h/\partial t$ from 2019 to 2022 color-coded from -6 to 0 m/yr with the GL positions of 1996 and 2019-2021; (b) $\dot{b}$ from 2019 to 2022 with the GL positions and limit of viability of the calculation (translucent grey) overlaid on bed topography with 100-m contours. 47

4.1 **Multi-year grounding line positions of Amery Ice Shelf, East Antarctica.** (a) Ice grounding zone color-coded from 2018 to 2019 with one GL reference from 1996 overlaid on surface topography from BedMachine v3.7 (BMv3.7) [53]; (b) bathymetry from BMv3.7 color-coded from 0- (white) to 3000-m depth (dark blue), with 200-m depth contours and subglacial channels (blue); differential radar interferograms and corresponding grounding line positions from (c) 2018 and (d) 2019 from Sentinel-1. 55

4.2 **Basal melt rate, $\dot{b}$, of Amery Ice Shelf, East Antarctica from 2019-2022.** $\dot{b}$ in meters per year on the floating ice of Amery Ice Shelf, East Antarctica for 2019 to 2022 with ice grounding zone (IGZ, dotted black), limit of viability (LV, translucent blue band), subglacial channels (blue), and profiles for Fisher Glacier (FG, dotted yellow), Mellor Glacier (MG, dotted blue), Mellor Esturary (ME, green), Lambert Esturary (LE, dotted red), and Lambert Glacier (LG, dotted light green). 59

4.3 **Basal melt rate, $\dot{b}$, along profiles.** (a–e) are $\dot{b}$ calculated along profile (a) FG, (b) MG, (c) ME, (d) LE, and (e) LG. Profile locations are color-coded in Fig. 4.2. In (a–e), the green forward diagonal-hatched column is the ice grounding zone (IGZ), the vertical light blue band is limit of viability (LV), and the grey dotted-hatched column is grounded ice (GI). 60

4.4 **Basal melt rate, $\dot{b}$, height-change rate, dh/dt, and flux divergence, $\nabla \cdot (H\mathbf{u})$, of Amery Ice Shelf, East Antarctica from 2019-2022.** (a) $\dot{b}$ near the ice grounding zone of Lambert-Mellor-Fisher Glaciers from 2019-2022 with the position of the ice grounding zone (dotted line) and limit of viability (blue) for the calculation of melt rates where ice is floating; (b) dh/dt from 2019-2022 color-coded from -2 m/yr to +2 m/yr; (c) $\nabla \cdot (H\mathbf{u})$ from 2019-2022; (d-g) time series of surface elevation at points LG, MG, ME, and FG in (b) to document the ice surface evolution on floating ice (points LG, MG, and FG) vs. grounded ice (point ME). 61

ACKNOWLEDGMENTS

I would like to extend my heartfelt gratitude to my PhD advisor, Dr. Eric Rignot, for his continued support and patience for my stubbornness. I also want to thank him for giving me the opportunity to shape the past five colorful years. I am profoundly grateful for the opportunity to have worked with such a remarkable scientist and a supportive research group.

I would like to thank my committee members, Dr. Francois Primeau and Dr. Isabella Velicogna, for their valuable advice, feedback, and different perspectives of thinking.

My sincere appreciation goes to my co-authors, Dr. Mathieu Morlighem, Dr. Shivani Ehrenfeucht, and Dr. Enrico Ciracì, whose expertise and help were invaluable and irreplaceable. Your help greatly improved the quality of this work. I would also like to thank Dr. Pietro Milillo, Dr. Paola Rizzoli, and Luigi Dini for providing the data to support this study.

I am grateful to the past and present members of my research group for their friendship and support. In particular, I would like to thank Dr. Lu An, Jae Hun Kim, and Ratnakar Gadi. You have accompanied me through many happy and difficult times. I truly value these friendships as my life's treasure.

Special thanks to Dr. Bernd Scheuchl for his support, encouragement, and listening on whatever matters I have, all the time.

Thanks to the support of my family and girlfriend, and the company of my friends, I can focus on pursuing the various things I want to explore.

This work took place at the University of California, Irvine, with financial support from the University of California, Irvine, Data Science Fellowship, and the National Aeronautics and Space Administration grants: the Earth Venture Mission Ocean Melting Greenland (OMG) and the FINESST Fellowship Program (Grant 80NSSC20K1618).

Chapter 2 is reprinted with permission from the American Geophysical Union (Geophysical Research Letters).

"Let this be my last word, that I trust in thy love.".

VITA

Hanning Chen

EDUCATION

Doctor of Philosophy in Earth System Science **2024**
University of California, Irvine *Irvine, California*

Master in Electronics and Communications Engineering **2019**
University of Electronic Science and Technology of China *Chengdu, Sichuan*

Bachelor in Spatial Information and Digital Technology **2016**
Chengdu University of Technology *Chengdu, Sichuan*

RESEARCH EXPERIENCE

Graduate Research Assistant, Earth System Science **2019–2024**
University of California, Irvine *Irvine, California*

Graduate Research Assistant, Resources and Environment **2016–2019**
University of Electronic Science and Technology of China *Chengdu, Sichuan*

TEACHING EXPERIENCE

Teaching Assistant, Earth System Chem **2022**
University of California, Irvine *Irvine, California*

Teaching Assistant, Earth's Atmosphere **2022**
University of California, Irvine *Irvine, California*

Teaching Assistant, Remote Sensing **2022**
University of California, Irvine *Irvine, California*

Teaching Assistant, Catastrophes **2021**
University of California, Irvine *Irvine, California*

Teaching Assistant, On Thin Ice **2021**
University of California, Irvine *Irvine, California*

REFEREED JOURNAL PUBLICATIONS

Rapid retreat of Berry Glacier, West Antarctica, from satellite radar interferometry and other data **2024**
H. Chen, E. Rignot, B. Scheuchl, P. Milillo, M. Morlighem, R. Gadi, E. Ciracì, J. Kim, L. Dini
Nature Geoscience, under review

Grounding zone of Amery ice shelf, Antarctica, from differential synthetic-aperture radar interferometry **2023**
H. Chen, E. Rignot, B. Scheuchl, S. Ehrenfeucht
Geophysical Research Letters

CONFERENCE PUBLICATIONS

H. Chen, E. Rignot, B. Scheuchl, P. Milillo, M. Morlighem, E. Ciracì, J. Kim (2023), Study of the grounding zone of Getz Ice Shelf, Antarctica using differential synthetic-aperture radar interferometry, Poster. *American Geophysical Union, Fall Meeting 2023*, San Francisco, CA.

E. Rignot, E. Ciracì, B. Scheuchl, R. Gadi, S. Ehrenfeucht, J. Kim, **H. Chen**, D. Holland, K. Nicholls, V. Tolpekin (2023), Deep seawater intrusions beneath Thwaites Glacier as a vehicle for rapid retreat, Oral. *American Geophysical Union, Fall Meeting 2023*, San Francisco, CA.

B. Scheuchl, J. Mouginot, E. Ciracì, E. Rignot, M. Morlighem, **H. Chen**, J. Barré, R. Millan, S. Jeong, Y. Mohajerani, V. Brancato (2023), A virtual SAR constellation to generate ice sheet geophysical information products for earth system science, Oral. *American Geophysical Union, Fall Meeting 2023*, San Francisco, CA.

H. Chen, E. Rignot, B. Scheuchl, J. Mouginot, S. Ehrenfeucht (2022), Study of the grounding zone of Amery Ice Shelf, Antarctica using differential radar interferometry, Oral. *American Geophysical Union, Fall Meeting 2022*, Chicago, IL.

B. Scheuchl, S. Jeong, E. Rignot, J. Mouginot, **H. Chen**, P. Milillo, V. Brancato, Y. Mohajerani, E. Ciracì (2021), MEaSUREs Ice Velocity and Grounding Line for Antarctica - an update, Poster. *American Geophysical Union, Fall Meeting 2021*, New Orleans, LA.

H. Chen, Y. Mohajerani, E. Rignot, B. Scheuchl, S. Jeong (2020), Detection of grounding line migration in Antarctica using InSAR and machine learning methods, Poster. *American Geophysical Union, Fall Meeting 2020*, Online.

B. Scheuchl, S. Jeong, Y. Mohajerani, **H. Chen**, J. Mouginot, E. Rignot (2020), Differential SAR interferometry-based, machine learning-supported delineation of grounding zones around Antarctica, Poster. *American Geophysical Union, Fall Meeting 2020*, Online.

AWARDS

Future Investigators in NASA Earth and Space Science and Technology **2024**
University of California, Irvine

CalSpace Fellowship **2023**
University of California, Irvine

Data Science Fellowship **2021**
University of California, Irvine

ABSTRACT OF THE DISSERTATION

Ice grounding zone processes in Antarctica from satellite SAR interferometry and other data

By

Hanning Chen

Doctor of Philosophy in Earth System Science

University of California, Irvine, 2024

Professor Eric Rignot, Chair

This dissertation presents a comprehensive study on the dynamics of ice grounding zones in Antarctica's ice shelves, with a particular focus on the Amery Ice Shelf and Berry Glacier. Using satellite radar interferometry and other data, this research examines the intricate processes of grounding line migration, ice dynamics, and basal melting. The findings highlight the significant impact of bed topography, subglacial hydrology, and seawater intrusions on ice grounding zone dynamics, challenging traditional models that assume static grounding line positions. In the Amery Ice Shelf region, the study investigates the Lambert, Mellor, and Fisher glaciers, where the analysis of Sentinel-1 data reveals extensive tide-induced grounding line migrations, with movements far exceeding previous estimates. Moreover, high speed of the seawater intrusions brings impressive basal melting in the ice grounding zone. These results underscore the importance of including detailed ice grounding zone processes in ice sheet models to better predict the glaciers' responses to ocean warming. For Berry Glacier in West Antarctica, the study documents a rapid ice grounding zone retreat over a 25-year period, driven by increased basal melting from warm Circumpolar Deep Water incursions. This retreat has resulted in a marked increase in ice discharge and surface elevation changes, demonstrating the glacier's accelerated response to oceanic forces. The research presented here contributes to a deeper understanding of the ice grounding zone processes in Antarc-

tica and emphasizes the need for refined modeling approaches that account for the complex interactions between ice, ocean, and subglacial environments. These insights are crucial for improving sea level rise projections and assessing the broader impacts of climate change on polar ice sheets.

Chapter 1

Introduction

Antarctica contains a volume of ice equivalent to a global sea level rise (SLR) of 57 meters. In a state of mass equilibrium, accumulation of snowfall inland balances surface ablation and ice discharge in the ocean at the periphery. Recent studies highlight that it is losing mass and contributing to SLR [95]. The contribution of Antarctic to future SLR also remains a large source of uncertainty [67]. Scenarios allowing 3°C of warming give an abrupt jump in Antarctica ice loss after around 2060 [17], but still with large uncertainty due to limitations of the physical models, e.g. poor observational constraints and not-well known physics. To reduce these uncertainties, we need to understand the processes taking place at the grounding line (GL), i.e. where ice detaches from the bed and becomes afloat [97].

Ice grounding zones (IGZ) are areas where the GL migrates back and forth with changes in oceanic tides. Ice in IGZ experiences the largest melt rates by the ocean [75, 74]. Accurately mapping IGZ is critical for several reasons. First, IGZ dynamic reveals the retreat and advances of glaciers. Thinning ice shelves reach floating sooner [107]. With a surface slope of 1%, a tide of 1 m or thinning of 1 m, migrates the IGZ by 100 m. Hence, changes in IGZ position are sensitive indicators of ice thinning. Second, the calculation of ice-sheet mass

balance depends on the accurate delineation of the IGZ since ice melts vigorously in contact with the ocean [77]. Third, information about the IGZ position helps us understand the physical processes that control the glacier retreat, e.g., ocean-induced ice melt, basal friction, and internal dynamics. Last, numerical models require this information to constrain basal ice conditions. Basal stress conditions vary drastically between floating and grounded ice [44]. The size and shape of the sub-ice ocean cavity near the IGZ affects sub-ice circulation, basal melt, and in turn the glacier speed [75].

East Antarctica, encompassing the vast expanse of the East Antarctic Ice Sheet (EAIS), represents a critical region for understanding ice dynamics and potential SLR. This region is predominantly characterized by its relatively stable ice sheet, which accounts for the majority of the Antarctic ice volume [79]. A key feature within this expanse is the Amery Ice Shelf, one of the largest ice shelves in East Antarctica. The Amery Ice Shelf plays a significant role in regulating ice flow from the interior to the ocean due to its buttressing effect, which slows glacier movement by providing resistance along the side walls of the bay and valley that confine it [24]. Recent studies indicate that the Amery Ice Shelf is experiencing changes due to atmospheric warming, leading to surface melting, as well as oceanic warming, which increases basal melting [98]. Understanding the dynamics of the Amery Ice Shelf is essential for predicting the future stability of the EAIS and its potential contribution to global SLR.

West Antarctica, in contrast, is characterized by its more dynamic ice sheet and the presence of several large, fast-flowing glaciers that terminate in floating ice shelves. The Getz Ice Shelf, located along the central coast of West Antarctica, is a prominent feature in this region. It spans over 300 kilometers and plays a critical role in stabilizing the ice flow from the inland glaciers it buttresses [35]. The Getz Ice Shelf is particularly sensitive to changes in ocean temperatures. The ice shelf has been observed to be thinning at an accelerated rate due to increased basal melting driven by the incursion of warmer ocean waters [63]. This process not only reduces the buttressing effect of the ice shelf but also enhances glacier discharge into

the ocean, contributing to SLR [78]. The dynamic response of the Getz Ice Shelf to climatic and oceanographic changes highlights the vulnerability of West Antarctica's ice sheet and underscores the importance of monitoring and modeling these changes to improve projections of future SLR.

The work described in this dissertation is focused on three main tributary glaciers of Amery Ice Shelf: the Lambert, Mellor and Fisher Glaciers, and the Berry Glacier of Getz Ice Shelf. The Lambert-Mellor-Fisher Glacier system is a key feature of East Antarctica, representing one of the largest glacier systems on the continent. The Lambert Glacier, which is the primary component of this system, extends over 400 km inland from the Amery Ice Shelf. The glacier system collectively drain a significant portion of the EAIS [78]. The Berry Glacier is characterized by its significant contribution to the mass balance of the Getz Ice Shelf, controlling 10% of the ice flux that feeds Getz. Both of the two study areas display fast GL migration driven by the tidal cycle, and exhibits IGZ length exceeding 10 km, making them good cases study for understanding short/long timescale glacier dynamics.This work explores GL migration characteristics over multiple timescales, glacier dynamcis responding to the GL migration, and basal melting of grounded ice.

1.1 Background

1.1.1 Grounding line migration

GL migration, a critical process in the dynamics of ice sheets, is significantly influenced by tidal height and the pressure exerted by tides. The GL is the point where the ice sheet transitions from resting on bedrock to floating on the ocean, and its position can fluctuate due to changes in external forces, including tidal variations [87]. Tidal forces affect the GL by modulating the buoyant support provided to the ice shelf. As tidal height increases, the

pressure from the rising tide can lift the ice shelf, reducing the contact between the ice and the bedrock, and causing the GL to retreat. Conversely, as the tide falls, the ice shelf settles back onto the bedrock, and the GL advances [7]. This process of GL migration is dynamic and occurs over tidal cycles, influencing the stability and flow of ice streams.

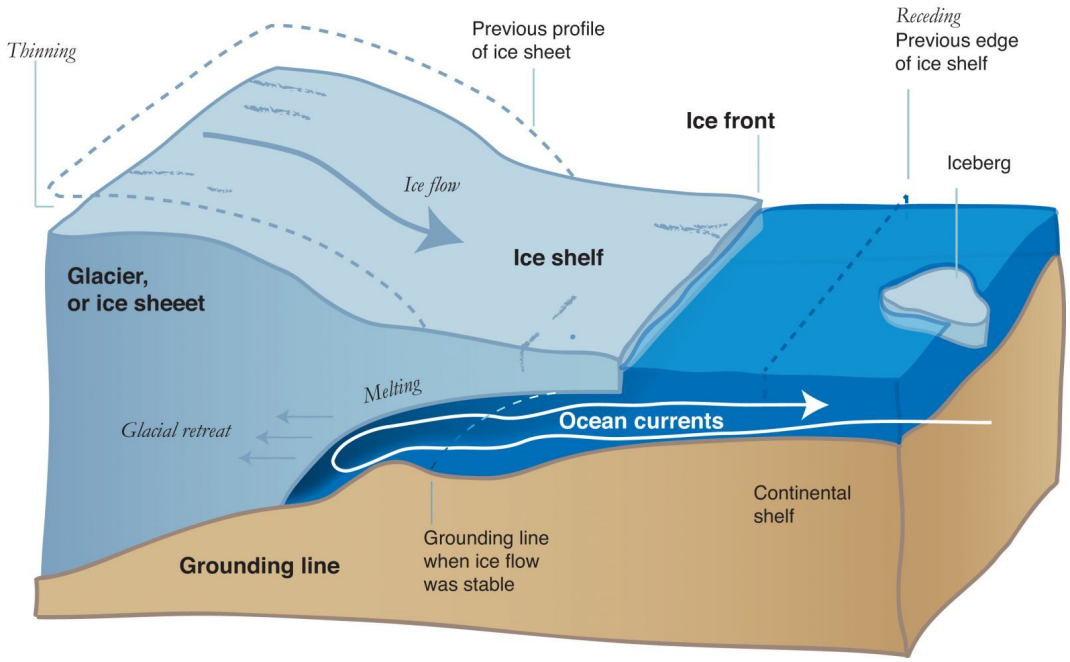


Figure 1.1: **Diagram of the grounding line.** The grounding line (GL), where ice on land meets the ocean and begins to float, is retreating or will retreat in many regions of Antarctic Ice Sheet, primarily because of ocean-induced melting under floating ice shelves. GL retreat is governed by the interplay among ocean circulation, ice dynamics, and bed topography. This figure was taken from NSIDC, NASA.

The interplay between tidal height and GL migration is complex and is influenced by several factors, including the geometry of the ice shelf, the subglacial topography, and the physical properties of the ice and bedrock. For example, in regions where the bedrock is sloped, tidal variations can have a more pronounced effect on GL migration. This is because the sloped bedrock allows for more significant changes in ice shelf buoyancy with tidal fluctuations [3]. An analysis of IGZ width in the Amundsen Sea sector reveals a strong relationship between IGZ width and thickness gradients [48]. This relationship is modulated by uncertainties in thickness slopes. The physical interpretation is that seawater pressure at the IGZ is

modulated by tide, by about 10 kPa per meter of tidal signal. This seawater is injected at high pressure beneath the glacier at high tide [6]. If the thickness gradient is negative, i.e. ice is getting thinner inland, seawater will infiltrate at greater distances, until the bed elevation drops (thickness increases). Conversely, if the thickness increases, the intrusion will be limited.

Observations and modeling studies have shown that GL migration due to tidal forces can lead to significant variations in ice discharge rates. For instance, in the Pine Island Glacier in West Antarctica, tidal-induced GL fluctuations were found to be up to several kilometers [9]. These fluctuations can enhance basal melting and influence the rate at which ice flows into the ocean. Tidal flexure, the bending of the ice shelf due to tidal forces, also contributes to increased fracturing and crevassing, further impacting ice dynamics [82].

Understanding the mechanism of GL migration is crucial for predicting future changes in ice sheet behavior and their contributions to SLR, as the GL controls the flow of ice from the interior of the ice sheet to the ocean, impacting overall mass balance and SLR.

1.1.2 Ice grounding zone mapping

The IGZ mapping technique (differential InSAR, DInSAR) combines two InSAR interferograms acquired along the same orbit, with the same time interval, to reveal the differential ice motion associated with tidal flexure and other processes, which could include ice subsidence associated with the drainage of subglacial lakes or channels, or subtle changes in glacier speed [76]. To maintain fringe visibility, the processing involves the pre-registration of images based on pixel offsets due to ice motion [45]. This process has been implemented routinely in the MEaSUREs processor [77]. Topographic correction is done with the TanDEM-X DEM of Antarctica. Data noise includes residual errors, signal associated with the draining and filling of small cavities by water, or subtle changes in speed with tide. As interferograms

acquired more than a couple of weeks apart are excluded, the method is not sensitive to speed up. Relative changes in dielectric path length associated with snowfall, ionosphere, or atmospheric water vapor are not to be excluded, but the dominant signal is the differential tidal motion. This approach has been used to detect IGZ positions [71, 77] and multi-year IGZ migrations.

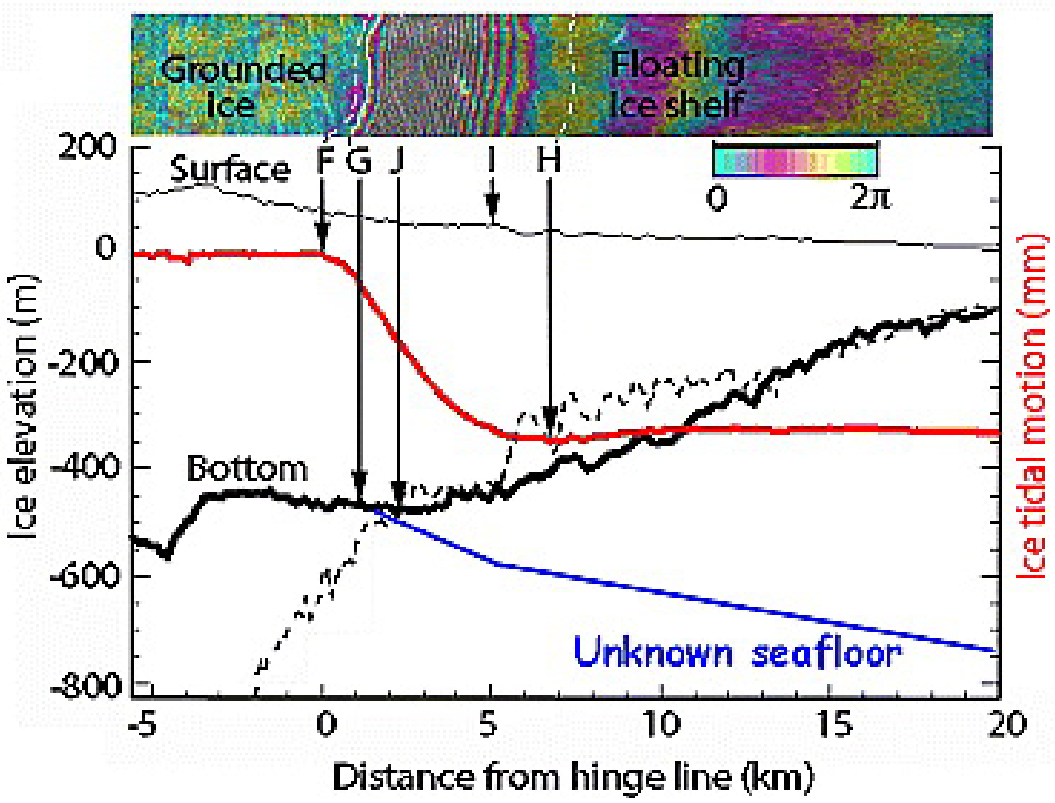


Figure 1.2: **Grounding line position from DInSAR interferometric fringes.** Ice grounding zone of Petermann Glacier, Greenland, with the limit of tidal flexing (F), the grounding line (G), the line of first hydrostatic equilibrium (J), the break in surface slope (I), the maximum extent of the flexure zone (H), ice surface elevation above mean sea level from laser altimetry (thin black line), bed topography from radio echo sounding (thick black line), bed depth calculated from hydrostatic equilibrium (dashed black line), the unknown seafloor (over-deepening likely exceeds 800 m) and tidal flexing measured with ERS-1 DInSAR in millimeter of vertical motion (red thick line). The color inset on top shows the DInSAR interferometric fringes, color coded from 0 and 2π, from blue to yellow, red and blue, and delineates F (dotted white line near G), G (white line), and H (dotted white on floating ice). Ice flows from left (grounded ice) to right (floating ice). This figure was taken from Rignot et al. (2011).

The performance of the ML approach for GL mapping is proved that it's comparable to that

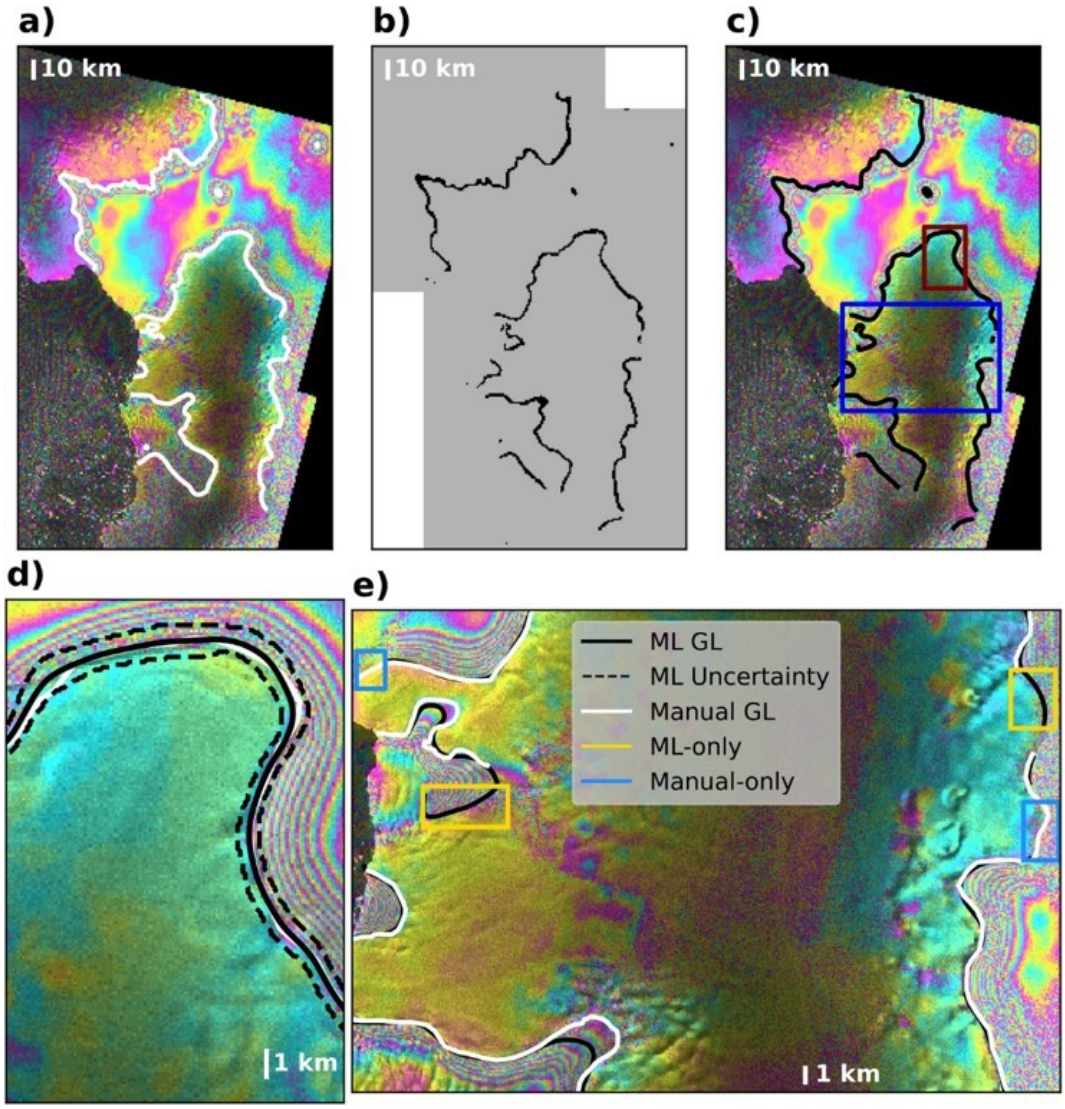


Figure 1.3: **Grounding line delineation from deep learning.** Different steps of the pipeline for (a) a sample interferogram with hand-drawn grounding line in white; (b) output of the neural network in raster format with a variable width that is a measure of uncertainty of the output. The gray mask in the background represents training (white) and testing (gray) sites; (c) Vectorized output and uncertainty contours; (d) zoomed-in region highlighted by the maroon box in panel (c) showing both manual and ML results and uncertainty bars; (e) Comparison of the manual and ML performances in the area outlined in blue in panel (c). The interferograms are obtained from Sentinel-1a/b data in 2018. This figure was taken from Mohajerani et al. (2021).

of a human interpreter, sometimes even better in noisy area, except over small grounded areas, e.g., ice rises, due to the limited grid spacing of the data (100 m) [51]. The approach was applied to all the year 2018 and 2019 S1 data. Meanwhile, adding ice velocity, DEM and tidal model to the training part of the algorithm can further improve the accuracy and stability of the algorithm. With consecutive S1a/b images acquired every 12 days, 20-30 DInSAR can be derived per year. With CSK, one DInSAR can be got every 16 days, or 20 /yr.

1.1.3 Ice dynamics

Ice dynamics in Antarctica, encompassing ice velocity and surface height change, are critical factors in understanding the behavior and stability of the Antarctic ice sheet (AIS). Ice velocity is a key parameter that measures the rate at which ice is transported from the interior regions toward the ocean, the location of preferred channels of ice transport, and how ice mass evolves with time. The spatial and temporal variations in ice velocity provide insights into the dynamic processes governing ice flow and the response of the ice sheet to external forcings, such as changes in atmospheric and oceanic conditions [55].

Ice velocity is influenced by several factors, including basal friction, ice thickness, and the presence of subglacial water. Regions with low basal friction, often due to the presence of subglacial water, exhibit higher ice velocities. For example, ice streams in West Antarctica, such as the Pine Island and Thwaites Glaciers, flow at velocities of several kilometers per year due to reduced basal resistance [38]. Conversely, the interior regions of the ice sheet exhibit much lower velocities, typically on the order of tens of meters per year, due to colder basal temperatures and higher basal friction [78].

Surface height change in Antarctica is another critical component of ice dynamics, reflecting the balance between ice accumulation and ablation processes, as well as dynamic thinning

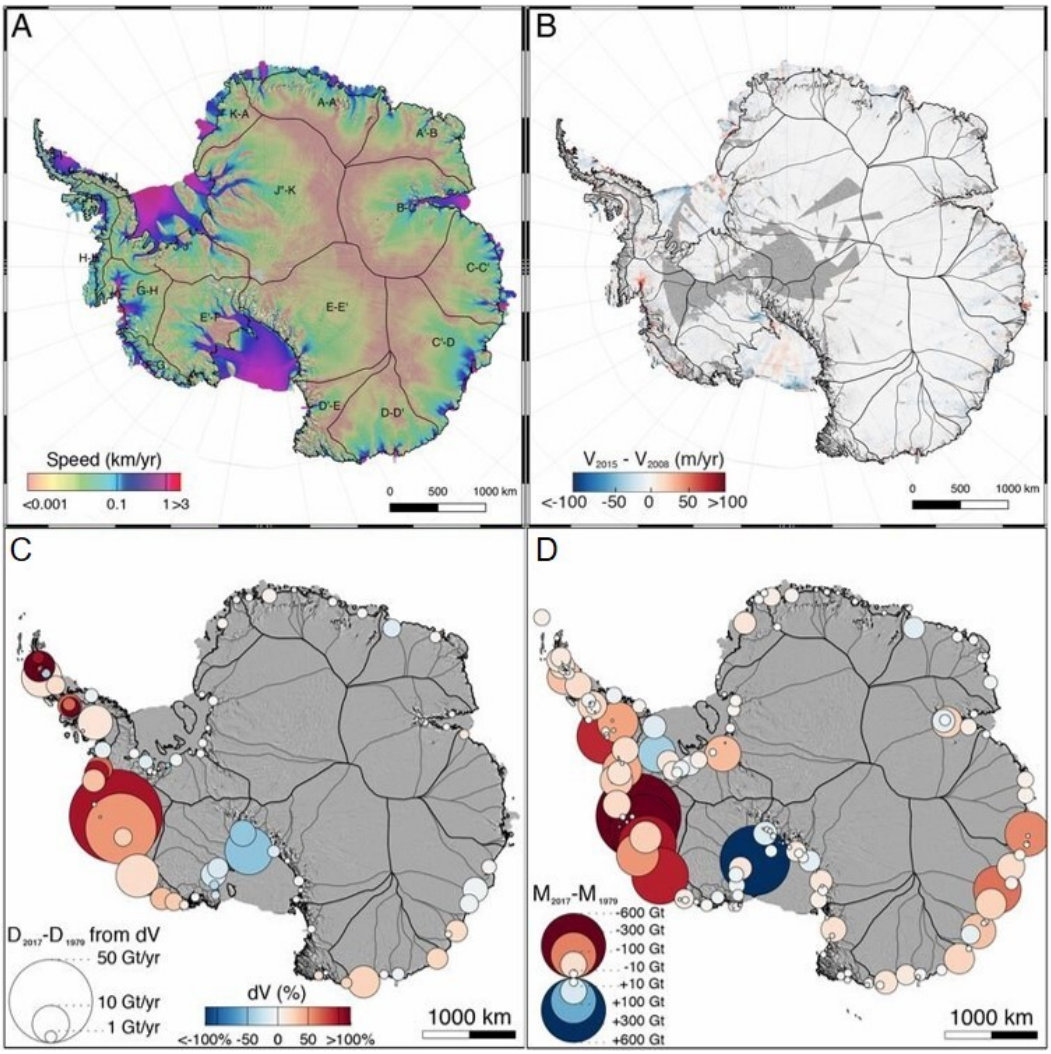


Figure 1.4: **Ice dynamics of Antarctica.** (A) Ice speed of the Antarctic Ice Sheet derived from multisensor data for the time period 2014–2016 with 18 subregions A–K (black thin lines) delineated from surface slope and ice flow direction data. (B) Change in flow speed from the time period 2007–2008 to 2014–2015. Grey areas have no data. (C) Change in grounding line ice discharge, D, for 1979–2017 for the 18 major subregions in billions of tons per year with percentage change in speed and circle radius proportional to change. (D) Total change in mass of major basins for 1979–2017 with circle radius proportional to the absolute mass balance. This figure was taken from Rignot et al. (2019).

or thickening due to ice flow. Studies have shown that significant surface height changes are occurring in key regions of Antarctica, driven by dynamic thinning and GL retreat. For instance, the Amundsen Sea sector of West Antarctica has experienced substantial dynamic thinning, with surface height reductions of up to several meters per year in some areas [96]. This thinning is largely driven by increased ice discharge and basal melting due to the intrusion of warm Circumpolar Deep Water (CDW) [79]. In contrast, East Antarctica shows a more heterogeneous pattern of surface height change. While some regions, such as Wilkes Land, are experiencing thinning, other areas, particularly in the interior, exhibit slight thickening due to increased snowfall [79].

1.1.4 Glacier mass balance

The total mass balance of an ice sheet is determined by the difference between the Surface Mass Balance (SMB) and ice discharge (D) at the periphery of the ice sheet. The observed mass loss of the AIS is attributed to both increased ice discharge and decreased SMB [73, 112]. SMB is computed as the net balance of surface processes, including snow accumulation, runoff, sublimation, evaporation, and wind-blown snow, among others. In contrast, ice discharge is calculated as the total mass flux crossing the GL, the point at which the glacier ceases to be in contact with bedrock and begins to float on the ocean. Glacier discharge accounts for both calving and the basal melting of floating ice. The primary contributor to Antarctica's mass loss is ice discharge. Specifically, the mass loss from West Antarctica is three to four times greater than that from East Antarctica and the Antarctic Peninsula. Throughout the study period, the AIS has consistently been in a state of negative mass balance, with snowfall accumulation insufficient to offset mass loss, including in East Antarctica [79].

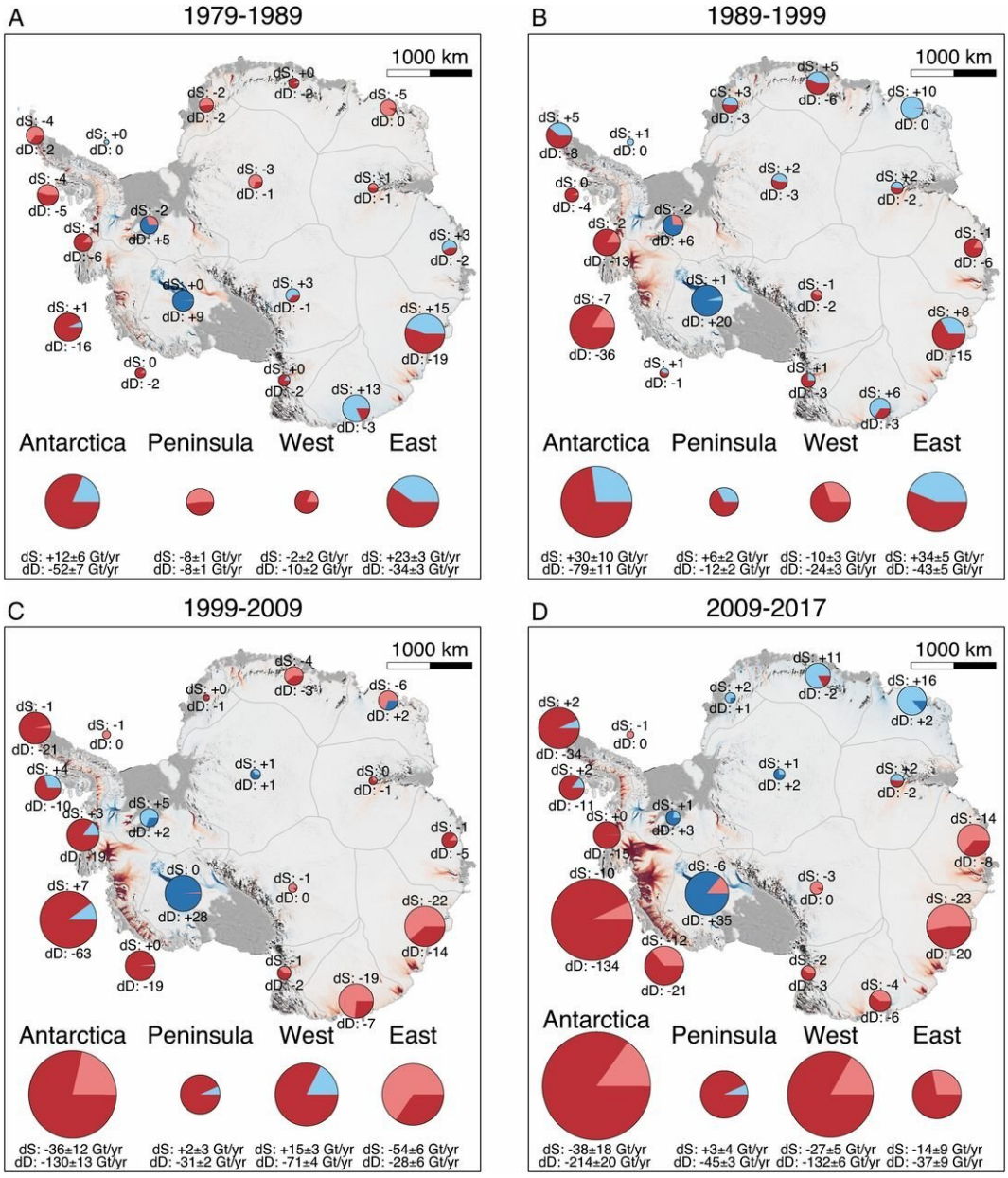


Figure 1.5: **Ice mass balance of Antarctica.** Ice mass balance of Antarctica using the component method (SMB, on grounded ice minus ice discharge, D, at the grounding line) for (A) 1979-1990, (B) 1989-2000, (C) 1999-2009, and (D) 2009-2017. The size of the circle is proportional to the absolute magnitude of the anomaly in D ($\delta D = SMB_{1979-2008}$ - D) or SMB ($\delta SMB = SMB$ - $SMB_{1979-2008}$). The color of the circle indicates loss in δD (dark red) or δSMB (light red) versus gain in δD (dark blue) or δSMB (light blue) in billions of tons (10^{12} kg) per year. Dark color refers to δD; light color refers to δSMB. Plots show totals for Antarctica, Antarctic Peninsula, West Antarctica, and East Antarctica. Background is the total mass balance spread into the drainage basins. This figure was taken from Rignot et al. (2019).

1.1.5 Ice shelf basal melting

Warm, salty, subsurface CDW that is consistent with enhanced polar westerlies pushing CDW toward Antarctica to melt its floating ice shelves and destabilize the glaciers, where it sits below the more buoyant and cold freshwater from ice melt. Upon entering fjords, the CDW contributes to glacier dynamics [36]. As the discharged meltwater is less dense than the surrounding ocean water, it rises vertically upon reaching the fjord. This vertical movement induces turbulent mixing, wherein the warm CDW combines with the meltwater and ascends buoyantly. This process results in a plume of relatively warm water that flows along the underside of the floating ice towards the ice front, intensifying melt at the ice-ocean interface near the GL [11, 66]. Consequently, this mechanism contributes to ice shelf thinning and constitutes a significant form of mass loss for certain glaciers [70].

The melting of floating ice can diminish the buttressing effect of ice shelves on glaciers, resulting in increased ice discharge and ultimately contributing to rising sea levels [105]. Furthermore, subglacial discharge plays a significant role in the ocean-driven melting of ice shelves [19, 30], yet it is often not incorporated into ice sheet models, potentially leading to inaccuracies in projections of future ice behavior and SLR. Runoff is not discharged uniformly at the GL but is dependent on the evolution of the subglacial hydrologic system. Modeling studies have demonstrated that subglacial discharge can amplify ice shelf melt [90, 57] and enhance melting at the calving front [16]. Recent research has also suggested that the intrusion of seawater beneath grounded ice via the subglacial hydrologic system can significantly increase melt rates and induce rapid GL retreat [81, 116]. Discrepancies between melt rates inferred from satellite data, field measurements, and ocean model calculations [12, 14, 33] could potentially be explained or mitigated by incorporating subglacial discharge in a more physically realistic manner.

Many ice shelves exhibit characteristic channels along their base in the direction of ice flow,

which some studies suggest are caused or enhanced by the irregular pattern of meltwater discharged from subglacial hydrology [41, 90]. These ice shelf channels have been associated with increased crevassing [2] and are believed to structurally weaken ice shelves [28, 69]. However, some research posits that these channels may have an overall stabilizing effect [50]. Several modeling studies have linked the presence of channels to enhanced fracture rates [90, 111], which may contribute to the eventual collapse of the ice shelf. Although the melting of floating ice does not directly contribute to SLR, it can diminish the buttressing effect of ice shelves on glaciers. This reduction in buttressing can ultimately increase total ice discharge, thereby contributing to sea-level rise.

1.2 Dissertation objectives

The global concern of SLR, which is projected to become increasingly critical over the next century, necessitates the use of models for accurate projections. We rely on models to project the rate of SLR, including from melting ice sheets, but those models lack crucial components needed for precise estimation of freshwater contributions to the oceans. In particular, numerical ice sheet models typically omit short-term variability in GL positions (e.g., due to tides) and fail to incorporate basal melt processes upstream of the GL to represent these glaciers [91], which brings considerable uncertainty for the SLR projection. This study aims to observe and understand IGZ dynamics of Amery Ice Shelf and Berry Glacier, how it affects ice-ocean interaction, glacier dynamics, and in turn the contribution of ice sheets to SLR. There are two central questions we aim to address: (1) How much does the IGZ migrate horizontally in response to changes in oceanic tide on different time scales, and how does the drainage of seawater intrusion/glacier geometry influence IGZ? and (2) What is the impact of IGZ migration on ice-ocean interactions, glacier dynamics, and the sensitivity of glacier speed to ocean thermal forcing?

1.3 Chapter overviews

In chapter 2, we investigate the dynamics of the IGZ of the Amery Ice Shelf using DInSAR. Our focus is on understanding the variations in the GL position in response to tidal forcing, with implications for glacier dynamics and contributions to SLR. By analyzing the Sentinel-1 time series data from 2018, we observe significant kilometer-scale GL migration that is not in phase with the oceanic tide, and identify two distinct migration states that switch intermittently over periods of several weeks. This study reveals that the migration of the GL is considerably more extensive than previously estimated, particularly in the Mellor and Lambert estuaries, where we detect migrations of 15.7 km and 10.7 km, respectively, which is substantially influenced by the underlying glacier geometry. The presence of subglacial channels and the associated seawater intrusions further amplify the IGZ length, particularly in estuaries with deep bed troughs. These findings suggest that the IGZ is not a fixed boundary, as traditionally assumed in ice sheet models, but rather a dynamic region influenced by subglacial hydrology and oceanic interactions. The presence of seawater intrusions within the subglacial channels, which reach thicknesses of 2-20 cm, underscores the complexity of the ice-ocean interface and its potential to enhance basal melting. Such interactions highlight the need to incorporate variable GL positions and enhanced melt rates in physical models to improve the accuracy of SLR projections from Antarctic ice mass loss.

In chapter 3, we explore the rapid retreat of the IGZ of Berry Glacier, West Antarctica, utilizing a time series of ERS-1/2, ALOS-2 PALSAR, Sentinel-1, and COSMO-SkyMed DInSAR data spanning from 1996 to 2021. This study focuses on the substantial IGZ migrations, which have increased from 0.6 km in 1995/1996 to 18.0±0.9 km in 2020-2021, marking one of the longest IGZs observed in Antarctica. Our analysis indicates a significant retreat of 18.1±0.4 km over 25 years, with the glacier's ice thickness decreasing by 17±1 m/yr and its speed increasing by 64±5%. Consequentially, Berry Glacier had experienced a substantial increase in ice discharge, from 0.9 Gt/yr in 1996 to 7.5 Gt/yr in 2022, resulting in a cumula-

tive mass loss of 131±23 Gt over the 25-year period, with 90% of this loss due to increased ice discharge.These changes are primarily attributed to enhanced basal melting driven by the influx of warm CDW via favorable bathymetric channels. The bathymetry on the continental shelf includes deep troughs that facilitate CDW access, promoting significant basal melting and contributing to the glacier's rapid retreat. Our findings underscore the critical role of oceanic heat flux and subglacial topography in driving the observed changes in Berry Glacier, highlighting the need for comprehensive models that incorporate these factors to improve predictions of future ice sheet behavior and sea level rise.

In chapter 4, we investigate the melt rates in the kilometer-size IGZ of Amery Ice Shelf, employing a time series of satellite data from the ICESat-2 mission. This study documents the GL migration and basal melt rates of the Lambert-Mellor-Fisher Glaciers system, a major drainage system in East Antarctica. We confirm that the GL migrates at tidal frequencies over an IGZ that spans 10 to 15 km, two orders of magnitude larger than expected for GLs on a rigid bed. The melt rates stay low on the floating ice shelf (9 m/yr) while the highest ice shelf melt rates are recorded within the IGZ overlaid on estuaries, with values ranging from 101±35 to 255±51 m/yr along channels, which is caused by the high speed of seawater intrusion. On the western part of the glaciers system, the melt rate exhibits a significant reduction, ranging from 34±12 to 48±17 m/yr. This deceleration may be attributed to lower thermal forcing caused by higher bed elevation, as well as the Coriolis effect, which facilitates the influx of relatively warmer oceanic waters from the east, leading to the melting of the grounded ice within the IGZ, and subsequently, the outflow of these waters to the west. These high melt rates contrast with the traditional plume model of GL melt, which predicts zero melt. Our results highlight the importance of incorporating kilometer-wide IGZs and vigorous ice-ocean interactions into numerical models to better predict glacier dynamics and contributions to SLR in a warming climate.

Chapter 2

Grounding zone of Amery ice shelf, Antarctica, from differential synthetic-aperture radar interferometry

2.1 Abstract

We employ a time series of Sentinel-1 differential radar interferometry data from 2018 to detect the variability in grounding line position of the Fisher, Mellor and Lambert glaciers, which drain about 47 billion tons of ice per year from East Antarctica. We observe kilometer-scale tidal migration, two orders of magnitude larger than expected for ice flowing over a hard bed. The migration is not in phase with changes in oceanic tide. In two estuaries underlaid by subglacial channels, we observe two states of migration that switch on and off over time scales of several weeks. The range of vertical motion reveals a water column

thickness of 2-20 centimeters. Such intrusions of seawater over wide grounding zones are not accounted for in physical models. Including them will add vigorous melting of grounded ice that will enhance the sensitivity of glaciers to ocean warming and increase projections of mass loss.

2.2 Introduction

The Antarctic Ice Sheet has contributed to sea level rise in recent decades [79], but there is considerable uncertainty about the projections of its evolution in the coming century [93]. A region of particular importance for mass budget and force balance assessments is the grounding line (GL), or the transition boundary between grounded and floating ice. Ice that crosses the GL starts to float on ocean waters and displaces sea water. Changes in the position of the GL have a profound effect on the regime of basal friction of a glacier, which is a major control on glacier speed [65]. When the GL retreats, the basal resistance to flow will be reduced, which may be conducive to glacier speed up depending on bed geometry and feedback processes. Conversely during an advance, the resistance to flow will increase, which may be conducive to glacier slow down. The GL is also important in terms of ice-ocean interaction. In the proximity of the GL with warm circumpolar deep water, ice melts in contact with ocean waters at rates that exceed the glacier surface mass balance by one to two orders of magnitude [80]. At the GL per se, however, the default assumption for most physical models is that ice melt is zero and the GL position is fixed [91].

Several methods exist to delineate GL positions, including GPS, tilt-meter, satellite altimetry [9], but the most precise method is satellite radar interferometry [77]. Satellite altimetry measures vertical motion in the 5-10 cm range along flight tracks. Satellite radar interferometry measures vertical motion at the 2-3 mm level, over entire swaths, typically greater than 100 km in width. In the past, satellite radar interferometry suitable for grounding

line mapping, i.e. with a short repeat cycle to maintain coherence of the radar signal with multiple consecutive repeat, were available only sporadically, collected by synthetic aperture radar (SAR) missions that had not been designed for this type of analysis. This situation changed with the launch of Sentinel-1a (S1) in 2014 at a 12-day repeat cycle to routinely observe the ice sheets [68]. The situation was improved to a 6-day repeat with the launch of S1b in 2016 flown in tandem with S1a. The S1 mission is the first mission that allows us to look at GL migration repeatedly, on short time scales, for many years. Unfortunately, S1b terminated its mission in December 2021 due to power issues.

In this study, we investigate the changes in grounding line position over a tidal cycle. These changes in position make up a zone, which we call the ice grounding zone (IGZ). For some authors, the GZ refers to the region of tidal flexure where ice adjusts to full hydrostatic equilibrium. In our terminology, this zone is called the flexure zone or ocean grounding zone, which is fundamentally different from the IGZ. Furthermore, in most physical models, the IGZ is reduced to a single GL position, i.e. the length of the IGZ is a single model element. Here, we document that the length of IGZ is much greater than a single model element.

We revisit the assumption of zero-length IGZ in this study. We analyze the 2018 migration of the GL, or IGZ, of the Amery Ice Shelf, a major glacier system in East Antarctica (Figure 1a) that is fed by three glaciers: the Lambert, Fisher and Mellor glaciers. Together these glaciers drain a sector of the ice sheet that holds an ice volume above sea level equivalent to an 8-m global sea level rise. This part of Antarctica offers high signal coherence for radar interferometry compared to other sectors, due to low precipitation rates, low temperature, and low flow speed. The Amery Ice Shelf system is in a state of mass balance at present and has probably been for the past 4 decades [79], hence providing a reference framework for a stable glacial environment in Antarctica. We report on the results of the observed IGZ, compare it with oceanic tides, bed and surface slopes, and discuss the importance of the

results for understanding and projecting glacier evolution in a changing climate.

2.3 Data and Methods

2.3.1 Sentinel-1 interferogram

We employ S1 radar interferometry data, acquired at the C-band frequency (5.6 cm wavelength), on a 6-day repeat cycle, to map the GL of the Fisher, Mellor, and Lambert glaciers in year 2018. The primary acquisition mode of the radar over land is the Interferometric Wide Swath (IW) mode, a Terrain Observation with Progressive Scans SAR (TOPS) mode [88]. The azimuth (along track) pixel spacing is 13.9 m, the slant range (across track) pixel spacing is 2.4 m. Ground resolution is 20 m in azimuth and 5 m in ground range [85]. We use 3 (A, B, and C each separated by 6 days or one cycle) to 4 radar images (A, B, separated by 6 days, and C, D separated by 6 days but acquired more than 6 days after B) to form a double-difference interferogram (either AB + BC or AB - CD) that reveal the differential tidal motion of floating ice during these 3 to 4 epochs. We assume that the ice horizontal motion is constant in between passes, so the differences in ice motion reveal the short-term vertical motion of the ice due to tidal flexing [78]. We detect the GL at the upstream end of a dense set of interferometric fringes caused by vertical motion of floating ice forced by tidal changes (Fig. 2.1c-d). We map the GL in 68 high-quality double-difference interferograms. As phase quality in the interferograms is not uniform across the scene, GL mapping is not complete in all 68 interferograms. From the envelop of 68 GL positions, we define an IGZ for year 2018, which is limited by the most upstream and downstream positions of the GL among all 68 delineations.

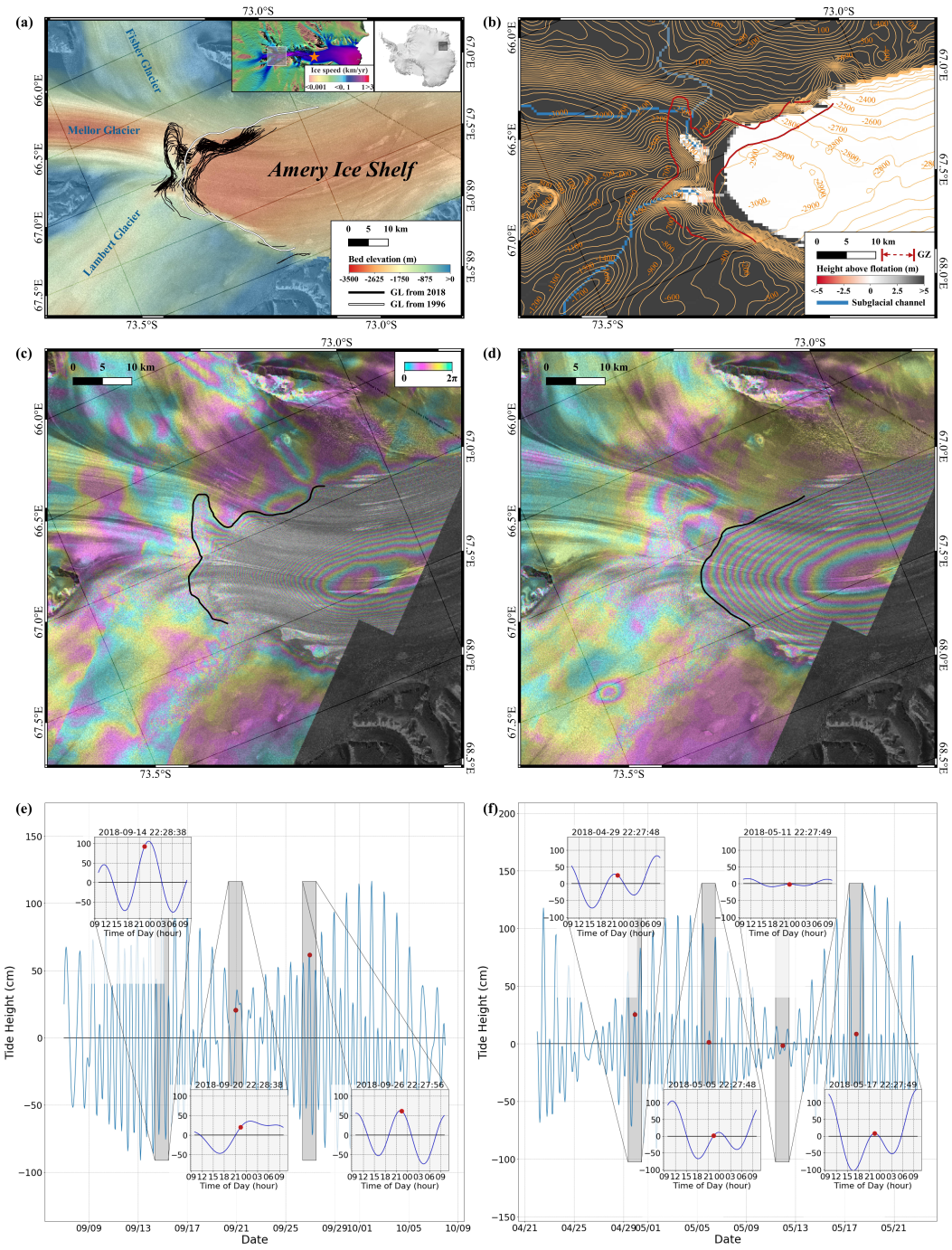


Figure 2.1: **Grounding line positions of Amery Ice Shelf, East Antarctica.** (a) 68 GL positions (black) of the Lambert, Fisher and Mellor glacier system, Amery Ice Shelf in year 2018 from S1 DInSAR data and one reference GL (white) in year 1996 from ERS-1/2 data [72] overlaid on the BedMachine bed topography [53]. Star in the inset map of ice speed denotes the location where tidal height is calculated; (b) grounding zone (red) in year 2018 overlaid on a map of height above flotation. Double-difference interferograms for the most c) upstream d) downstream positions of the GL (black line) overlaid on radar brightness; (e-f) tidal height (red dot) at the time of acquisitions used to form the interferograms in (c-d).

2.3.2 Tide model and atmospheric pressure

Floating ice moves up and down with changes in oceanic tides and atmospheric pressure. We calculate the tidal state using the CATS2008 model [61] (Fig. 2.1e-f), which is a regional high-resolution ocean tide model with a precision of 5 cm [27]. The inverse barometer effect (IBE) correction is the isostatic response of ocean surface height to changes in atmospheric pressure at a rate of 1 cm/hPa [62]. We calculate IBE from anomalies in mean sea level pressure reconstructed by the fifth generation of ECMWF atmospheric reanalyses of the global climate (ERA-5), which provides hourly outputs, at 31 km horizontal resolution, from the Earth surface to 0.01 hPa [31]. We calculate a mean pressure over the entire year 2018 and use that as a reference to deduce the anomalies in pressure and calculate the IBE correction.

2.3.3 Surface, bed and thickness slopes

To calculate surface α, bed β, and thickness λ slopes, we use BedMachine Antarctica v2 (BMv2) where ice surface elevations are represented as solid-ice equivalent [53]. BMv2 derives bed elevation and ice thickness using a mass conservation algorithm in regions of fast ice flow and kriging and/or streamline diffusion in the interior to fill in the gaps between radio-echo sounding data [53]. Downstream of the grounding line, BMv2 uses the International Bathymetric Chart of the Southern Ocean Version 2.0 (IBCSOv2) at 500-m spacing [18]. We calculate the slopes along the direction of GL migration over a length scale equal to 3 times the ice thickness, unless we detect an obvious and relevant change in slope that requires us to calculate the slope over a shorter segment.

2.3.4 Grounding zone length from flotation

If ice is in hydrostatic equilibrium, the GL should migrate horizontally in proportion to the change in sea level height multiplied by a coefficient γ, which depends on surface and bed slopes and the densities of ice and seawater: $\gamma = (1 - \frac{\rho_i}{\rho_w})\beta + \frac{\rho_i}{\rho_w}\alpha$ where $\rho_i = 917$ kg/m^3 and $\rho_w = 1027$ kg/m^3 are the density of ice and seawater respectively. In reality, the migration is amplified by a factor a compared to γ as discussed next due to bed deformation, bending flexure, and tidal pressure [48].

2.3.5 Subglacial channels

We calculate the position and freshwater fluxes of subglacial channels generated by basal friction and geothermal heat over the entire drainage basin using ISSM [40]. Basal friction is calculated by ISSM from model fitting of the measured ice velocity, heat transfer to the ice is modeled using an enthalpy approach, and with no surface runoff production. The reconstruction is performed at the grid spacing of BMv2. Fluxes are expressed in cubic meter per second. The goal of this calculation is simply to represent the positioning of the active subglacial channels versus the zones of migration of the grounding line.

2.4 Results

2.4.1 Grounding line migration and seawater intrusion

The availability of multiple GL measurements at different tidal states during the same calendar year allows the identification of the IGZ (Fig. 2.1b - 2.2a), or region where the GL migrates back and forth with changes in oceanic tides and atmospheric pressure. We mea-

sure the IGZ length by calculating the distance between the most retreated GL position and the least retreated position along the direction of migration (Fig. 2.2a). The widest IGZ in 2018 is $15.76^{+0.5}_{-2.}$ km along Mellor Estuary (ME). We name this region an "estuary" because it corresponds to a natural pathway on the bed for seawater intrusion as well as subglacial water outflow. The smallest IGZ length is $2.6^{+0.3}_{-0.09}$ km (Fig. 2.2a). The IGZ length reaches a maximum of $10.7^{+1.0}_{-0.9}$ km along the Lambert Estuary (LE). These two wide IGZs coincide with two inland estuaries, i.e. pronounced valleys in bed topography that extend in the inland direction where ice is thicker than in the surrounding areas (Fig. 2.1b). At these estuaries, we calculate subglacial freshwater fluxes of respectively, 461 m^3/s and 562 m^3/s, which is several times larger than for the other channels.

Based on the vertical deformation of ice measured with radar (Fig. 2.1c), we estimate the water column thickness when the GL is at its most retreated position. The thickness varies from zero at the upstream limit, by definition, to a few 10s of cm at the other end of the IGZ, which is the most advanced position of the GL. The variation in height is quasi linear versus distance on the broader part of the IGZ, consistent with an elastic flexing of the ice, and several times slower in the upper part of the estuaries (Fig. 2.1). This change in climbing rate of the flexure zone is manifest as an increase in fringe spacing (360° change in phase) toward the upper end of the estuaries. Taking the double-difference interferogram in Fig. 2.1c as an example, the vertical displacement caused by seawater in the Mellor Estuary is 4 fringes (count downstream from the GL), or a water column of 12 cm (Fig. 2.2b). Although the intruding seawater column is thin, its speed of travel will be significant because seawater has to travel several kilometers in 6 hours. If we assume that the tide reaches the upper GL position in one cycle (from the lowest tidal height to the acquisition time), seawater intrusion in Fig. 2.2b will be 2.9 km/h or 80 cm/s. The slowest speed will be 0.5 km/h or 14 cm/s.

The particularly deep ice (∼2500 m) at the GL of Amery Ice Shelf is particularly susceptible to high melt because of the pressure dependence of the freezing point of seawater. At 2,500 m

depth and 34.5 psu, the freezing point of seawater is depressed by 1.9°C to about -3.9°C. With an in-situ temperature of the ocean at -1.9°C [26], which is relatively cold, this corresponds to a thermal forcing of +2°C, which is significant. With high current speeds, we expect high entrainment speeds and high melt rates.

2.4.2 Grounding zone length and slopes

For comparison, we calculate the IGZ length based on hydrostatic equilibrium [108] along 7 profiles. The expected IGZ length, or Hydrostatic Equilibrium (HE) IGZ, is $\Delta L_{HE} = \Delta h[\beta + \frac{\rho_i}{\rho_w}(\alpha - \beta)]^{-1}$ where Δh is the change in tidal height. Surface α and bed β slopes are determined along the profile tracks and averaged over an interval of several ice thickness (Fig. 2.3d-j). For the regions with wide IGZ, the slope is mostly retrograde. Elsewhere, the slopes are mostly prograde. When we compare the results with the observed length of the IGZ (Fig. 2.2a), we find an amplification, a, of ten, well beyond errors. The ratio exceeds two orders of magnitude in the estuaries. On average, the interferograms indicate an IGZ length that is 71±40 larger than deduced from HE, which is about 200 m.

The GL is at its most retreated position at high tide, when ice is lifted off the bed by rising sea levels, and at its most advanced position at low tides, when ice is lowered by receding sea levels. Linear regression analysis between the interferogram-based vertical displacements and CATS2008 predictions corrected from IBE, shows a coefficient of determination of 0.995 and a root-mean-square error of 0.90 cm (Fig. 2.2c). Considering the uncertainty in bathymetry and tidal delay, we choose the middle point (250 km from the GL) between the GL and the open sea to calculate tides. We obtain a good fit with observations, which provides confidence that the interferograms and tidal models are reliable. The fit is not significantly modified if we alter the position of the tidal estimate by ±100 km. The IBE correction improves the model fit (without the IBE correction, the coefficient of determination drops

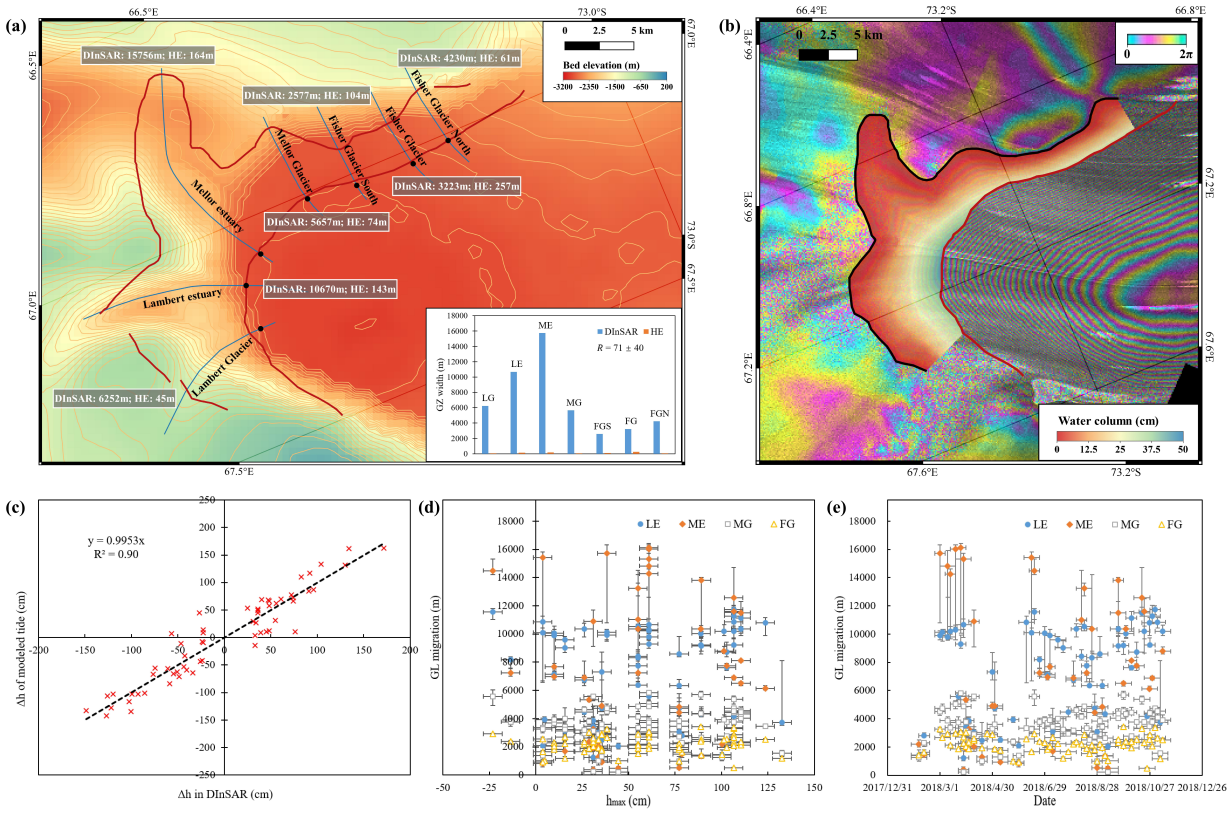


Figure 2.2: **Grounding line migration of Amery Ice Shelf, East Antarctica.** (a) Grounding zone (red) and location of 7 profiles (blue) along Lambert Glacier (LG), Lambert estuary (LE), Mellor estuary (ME), Mellor Glacier (MG), Fisher Glacier South (FGS), Fisher Glacier (FG), and Fisher Glacier North (FGN) overlaid on BedMachine bed topography starting at the black dot. Inset chart compares observed IGZ length versus modeled from flotation; (b) water column thickness within the IGZ in Fig. 2.1c; (c) modeled differential tidal height versus observed with interferometry. GL position versus (d) maximum tidal height during the 3 to 4 acquisition times at LE, ME, MG, and FG profiles and (e) versus time.

to 0.932 with a root-mean-square error 0.78).

Despite the agreement in differential displacement of the ice surface, we detect no correlation between absolute GL position and maximum tidal height, h_{max}, among the 3-4 epochs used to construct the interferograms (Fig. 2.2d). Our hypothesis is that the most retreated position corresponds to the maximum tide, h_{max}, here up to 130 cm. The migration along Mellor Estuary varies from 375 m to 16,130 m versus 1,242 m to 11,731 m along Lambert Estuary. The migration at Mellor and Fisher glaciers are, respectively, 206 m to 5,827m and 502 m to 3,425 m, hence comparatively short. None of these migrations occur in phase with the oceanic tide. Looking in more detail, however, we find a periodic migration pattern between two GL positions, one far upstream and one closer to the remainder of the IGZ. When the GL reaches the upstream stage, both GL positions stay in that mode for many weeks, before resuming a downstream migration. The re-advances bear no obvious relationship with the tide. The switch in position does not coincide with a period of lower tides (Fig. 2.2e). These switches on and off, however, occur simultaneously in the two estuaries, which suggests that the tidal state remains a major control on their evolution.

We compare the IGZ length with α, β, and λ. For Mellor and Lambert estuaries, once the intrusive seawater climbs past the initial, shallow, prograde bed slopes, it enters a domain of several kilometers in length with retrograde bed slopes of 4.1% and 1.4%, respectively (Fig. 2.3e-f). For the other profiles, the seawater intrusions are not able to overcome the prograde bed slopes of 23% to 61% at the beginning (Fig. 2.3d, g-j). We use the average slope across the prograde regions to characterize the slopes for the small IGZ length and the average slope of the most upstream part of the domain to characterize slopes for the widest IGZ length. Our results indicate a quasi-exponential relationship between IGZ length and slopes (Fig. 2.3a-c). The highest correlation is recorded with bed slope, followed by ice thickness slope, and surface slope. The correlation between surface slope and IGZ length is lower, in part because the agreement is especially poor for the Mellor Estuary which runs transverse

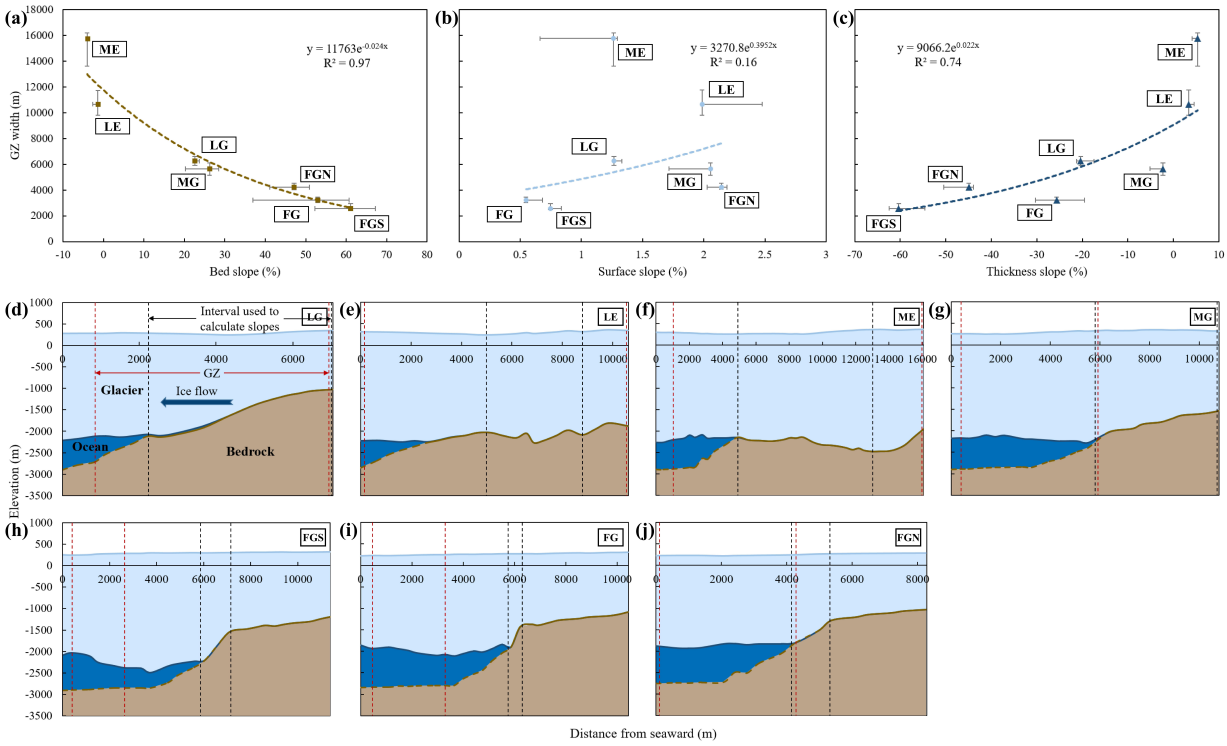


Figure 2.3: **Grounding zone length versus bed, surface, and thickness slopes.** (a-c) Comparison of IGZ length versus bed, surface, and thickness slopes using BMv2; (d-j) surface, ice draft, and bed elevations along the seven profiles with IGZ boundary (red dotted line) and domain of calculation of slopes (black dotted line). For bed elevation, we separate areas where mass conservation has been applied (brown solid) versus bed elevation from IBCSO2 (brown dotted).

to the direction of ice flow (Fig. 2.3b). Similarly, the poor correlation between IGZ length and thickness slope is caused by Mellor Estuary.

As a side result, our observations call into question IBCSOv2. Where BMv2 indicates a thick water column, our data reveals GL migration, i.e. ice partially grounded. The absolute error in bed elevation reaches 500 m, with IBCSOv2 being too deep. As a first guess, we suggest that the seafloor depth be forced to match the depth of the ice draft over the entire IGZ of the glacier. Additional data should be collected to revise the remainder of the ice shelf cavity.

2.5 Discussion

Our analysis of interferometric SAR data from 2018 indicates that the GL of Amery Ice Shelf migrates inconsistently with changes in oceanic tides, with large migration in Mellor and Lambert estuaries along retrograde slopes, much less in the remainder of the GL, but considerably more than expected from flotation of ice on a hard bed. Our interpretation is that the bed troughs with retrograde slopes facilitate intrusion once seawater leaps over the edge of the prograde slopes (Fig. 2.3). The magnitude of the migration is considerable. Previous work at Denman Glacier revealed a maximum migration on the western flank, along a deep trough with a retrograde slope, of 5.4 km [8]. Here, the 15-km retreat of the GL in Mellor Estuary is one of the largest on record in Antarctica. On average, the IGZ length is 70 times wider than expected from HE. Also, we emphasize again that the IGZ is the region where the GL itself migrates back and forth rather than the interval between the limit of tidal flexure and the landward limit of the hydrostatic zone of free-floating ice shelf. For instance, the largest value recorded for the IGZ of Amery previously, about 12 km [23], is actually the length of the flexure zone.

A 13 x wider IGZ length was reported for Getz Ice Shelf, in West Antarctica [51]. This work indicates that Getz is not an isolated case, but probably the norm. There are several potential explanations for the wider IGZ, including the fact that ice interacts with a deformable bed instead of a hard bed [83]. Wide un-grounding may also be interpreted as the propagation of an elastic crack through the ice [108]. Finally, bending stresses may migrate horizontally as the tide migrates to facilitate a wider retreat [113]. Resolving this issue is beyond the scope of our study. There could be multiple additional factors at play, e.g. bed topography details, geologic makeup of the bed, the presence of subglacial channels, which we do not know at this time and require further work.

The volume of seawater transported in these estuaries is not large because water thickness is measured in centimeters to several 10 cm, but the water flow may reach considerable speeds over one tidal cycle. We estimate flow speeds in the range of 14 to 80 cm/s, which will cause vigorous ocean heat transport to the ice base because ice melt is proportional to the thermal forcing from the ocean multiplied by the entrainment speed. Such entrainment speed is typical of strong plumes beneath an ice shelf and areas of vigorous melt [41]. Most current physical models assume a fixed grounding line with zero melt of grounded ice [93]. Our observations contradict this assumption. There are two major consequences for the ice sheet modeling. One is that grounded ice will melt in the grounding zone during tidal flushing, i.e. we cannot assume a fixed grounding line with zero melt. Second, ocean thermal forcing is applied over a considerable region, hence affecting resistance to flow from basal friction. If the ocean warms up, the melting of grounded ice will increase, the ice will become ungrounded, which will lead to an acceleration in ice flow because the region affected by the change will be large. Conversely, if no grounded ice is removed because the grounding line is fixed, the glacier will only be affected by ocean warming from a reduction in side drag as the ice shelf thins, which will have a lower impact on glacier speed. If tidal flushing stops when water gets trapped in the estuaries, the entrainment speed will be zero, which will limit heat transfer to the ice and the melt rates.

The GL is not migrating in phase with the tide, which is surprising, and there is an asymmetry between incoming and outgoing tides, as noted elsewhere [114]. For the incoming tide, a hydrodynamic pressure gradient applied across the subglacial cavity will force ocean water into the IGZ, driving the inland migration of the GL. As the tide recedes, the water at the IGZ will not drain instantly, but may be trapped in the hydrological network against gravity. This ocean water may remain in the subglacial environment for a long period of time, possibly several weeks. The drainage speed will be controlled by the effective resistance to flow through the hydrological network and the small along-slope component of gravity. There is a possibility that the intruding seawater will be drawn into the subglacial water system at low tide, and then force its way farther inland as a brackish mixture when the pressure gradient reverses at high tide [113]. This asymmetry may lead to the accumulation of the trapped water across multiple tidal cycles or a lag in GL advance. In the Amery Ice Shelf, the intruding seawater is trapped for an entire month on occasion. If the drainage is slow, the GL may be fixed at the high tide position, disconnecting the response of grounded ice to ocean tides, and yielding low melt rates of grounded ice. Such trapping of seawater is prominent in the ME and LE troughs. Eventually, the cavity opens up to let the seawater drain. We do not know what physical process causes the sudden drainage of trapped water. One possibility is a slow buildup of water mass from the continuous inflow of subglacial water, until a threshold is reached that forces the pressurized subglacial water to raise the glacier surface and connect with the ocean again.

In the modeling of grounding line migration as an elastic crack, the relationship between crack growth (here GL migration) and thickness slope is quadratic [109], as observed here. Seawater intrusion will be favored on shallow thickness slopes and it may be possible to predict the IGZ length. Along estuaries, where bed slope varies, a detailed understanding of water intrusion will require detailed hydrodynamic modeling.

It will be important to examine other regions of Antarctica to see if the same level of

migration occurs elsewhere. The answer is likely to be positive given the prior study of Getz Ice Shelf and the fact that the bed of Amery Ice Shelf does not have an exceptional character in Antarctica. The inclusion of a wide IGZ with vigorous ice melt will impact projections of sea level rise from physical models. Earlier simulations suggested that the mass loss from a glacier could be enhanced by a factor of two using wide grounding zones with vigorous melt [113]. In that regard, it will be of interest to study the melt regime of ice in the IGZ to further constrain the physical models. Such a study will require a dense time series of digital elevation models over several years, which is not available to us at this time.

2.6 Conclusions

A detailed mapping of the GLs of Amery Ice Shelf, East Antarctica, conducted with differential interferometry, reveals a complex, inconsistent, but large pattern of GL migration. In year 2018, we detect 15.7 km and 10.7 km migration on Mellor and Lambert estuaries, respectively, along mostly retrograde slopes. The retreat is less on the remainder of the GL, which exhibits mostly prograde slopes, but remains one order of magnitude larger than expected from hydrostatic equilibrium over a hard bed. Several alternative explanations for the GL migration are possible. The non-linear relationship between GL migration and tide and the existence of switches in GL position over time between two states indicates non-linearities in cavity and estuary filling at tidal frequencies, as discussed in [114]. Such asymmetry allows intrusive seawater to be trapped inland, with possibly less impact on ice melt. Conversely, a wide IGZ with strong incoming tidal flow will melt basal ice vigorously. This tidal interaction is not represented in current physical models. Our observations suggest the use of variable GLs instead of fixed GL in physical models and require calculation of potential enhanced melt rates with the dynamic GLs in future work, which will likely improve sea level rise projection from the glaciers.

Chapter 3

Rapid retreat of Berry Glacier, West Antarctica, from satellite radar interferometry and other data

3.1 Abstract

We employ a time series of ERS-1/2, ALOS-2 PALSAR, Sentinel-1, and COSMO-SkyMed differential synthetic-aperture radar interferometry data from 1996 to 2021 to document the short and long-term migrations of the grounding line (GL) of Berry Glacier, West Antarctica, a major tributary of Getz Ice Shelf that controls 10% of its ice discharge. In 2019-2021, we find a short-term GL migration of 18.0±0.9-km, which is exceptional. It implies a major revision of the bed topography of the terminal valley which is 1,300 m deeper than previously known. The tidal migration oscillates between three states controlled by bed topography. Seawater intrusions are not always followed by seawater extrusions, i.e. a portion of the seawater/melt water mixture gets trapped during the tidal cycle. Over the period 1996 to

2021, the most-inland position of the GL retreated by more than 18 km, or 0.7 km/yr, ice thickness decreased by 17±1 m/yr, ice sped up by 64±5%, and the mass loss totalled 131±23 Gt. We attribute the rapid retreat to enhanced ocean heat flux from warm Circumpolar Deep Water (CDW) via favorable bathymetric channels into a deep ice shelf cavity, carved by vigorous km-sized seawater intrusions beneath the glacier that cause accelerated basal melt.

3.2 Introduction

The Antarctic Ice Sheet has been a major contributor to sea level rise over the past four decades [79], but projections of its evolution in the coming century are effected by large uncertainties [93]. Central to these uncertainties is the modeling of the evolution of the grounding line (GL), i.e., the transition boundary between grounded and floating ice. Ice that crosses the GL becomes afloat in the ocean waters and displaces sea level. Changes in the position of the GL affect the regime of basal friction of the glacier, which in turn controls its speed, ice discharge, and mass loss [65]. During a GL retreat, basal resistance may drop and result in a glacier speed up. Conversely, during a GL advance, resistance to flow may increase and result in a glacier slow down. Near the GL, a number of Antarctic glaciers are in contact with warm, salty waters of Circumpolar Deep Water (CDW) origin that melt ice rapidly [80]. Most numerical ice sheet models do not account for a short-term variability in GL position (e.g., due to tides) and do not apply basal melt upstream of the GL to represent these glaciers [91]. In this study, we revisit this assumption with novel InSAR observations.

Global Positioning System (GPS), tilt-meters, satellite altimetry [9], and satellite radar interferometry [77] have been used to delineate GL positions. Altimetry detects vertical motion below a satellite track with a precision of 5-10 cm. Radar interferometry (InSAR) detects vertical motion over a 100-km wide swath with a 2-3 mm accuracy. InSAR GL

mapping started in 1995-1996 with the Earth Remote Sensing Satellites 1 and 2 (ERS-1/2) at a 1-day repeat cycle and resumed in 2014 with Sentinel-1a (S1a) at a 12-day repeat cycle [68] and Sentinel-1b (S1b) in 2016, at a 6-day repeat cycle for the S1 constellation until December 2021. Here, we also include data from the ALOS-2 PALSAR in 2008-2009 and a time series from the COSMO-SkyMed (CSK) constellation at a 1-day repeat cycle in 2020-2021. We characterize the short and long-term variability in GL position of Berry. The short-term variability defines an "Ice Grounding Zone (IGZ)".

We use a machine learning (ML) approach from [51] to map the tidal-induced variability in GL position around Antarctica (Fig. 3.1) in 22,713 interferograms, which represents all 6-day and 12-day interval DInSAR interferograms acquired in year 2019 from Sentinel1-a/b. In the ML results, Berry Glacier, in West Antarctica, stands out with a significant length of IGZ. Berry Glacier drains a sector 5,593 km^2 in size into the Getz Ice Shelf, Antarctica (Fig. 3.2). Getz drains an area of 85,900 km^2, with a 22-cm sea level rise equivalent. Berry controls 10% of the ice flux into Getz. Berry flows at 760 m/yr at the GL and holds an ice volume equivalent to a 1.5-cm global sea level rise. High melt rate of Getz Ice Shelf caused by undiluted warm, salty CDW makes it the largest producer of ice shelf melt water in Antarctica [34].

3.3 Data and Methods

3.3.1 Double-difference interferogram

We use ERS-1/2 (Supplementary Fig. A.8a-b), ALOS-2 PALSAR (Supplementary Fig. A.8c-g), S1a/b and CSK radar interferometry data to delineate the GL of Berry Glacier from 1996 to 2021. ERS-1/2 operated on a 1 day cycle in 1995–1996 during the tandem mission and on a 35-day cycle otherwise, at the C-band frequency (wavelength of 5.6 cm),

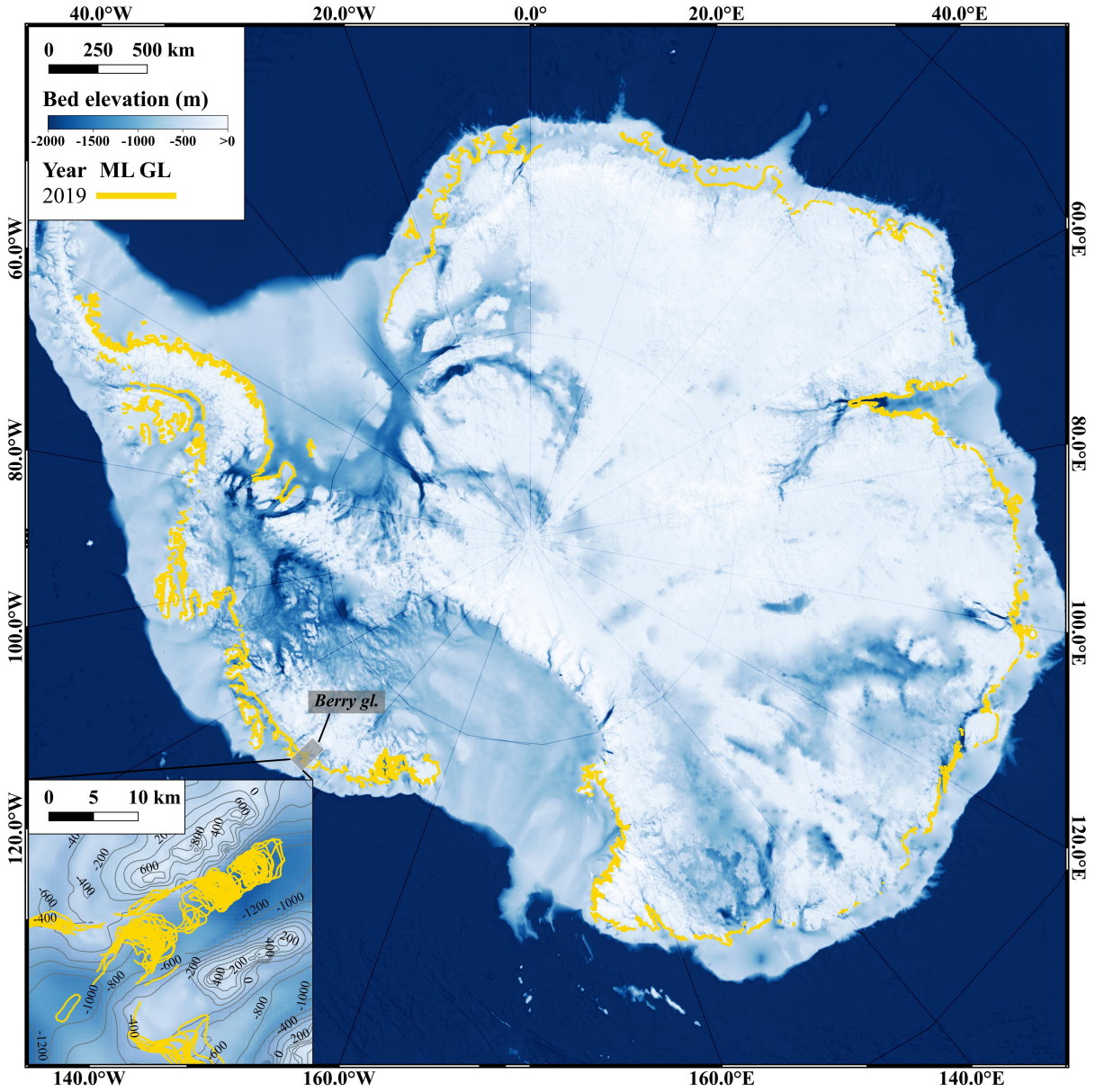


Figure 3.1: **Grounding line from machine learning covering Antarctica.** Antarctic grounding line delineation (yellow) from machine learning with Sentinel-1 double-difference InSAR in year 2019.

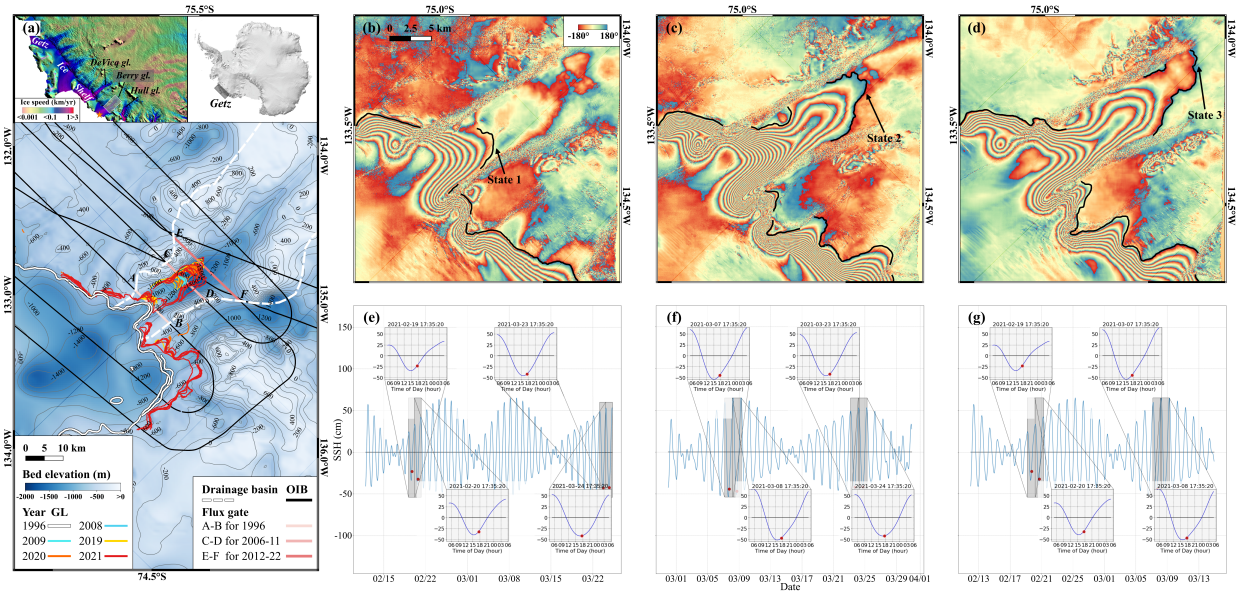


Figure 3.2: **Grounding line positions of Berry Glacier, West Antarctica.** (a) 88 GLs (location in inset) from year 1996 (white) from ERS-1/2, 2008 (blue)/2009 (cyan) from ALOS-2 PALSAR, 2019 (yellow) from Sentinel-1, and 2020 (orange)/2021 (red) from CSK radar interferometry overlaid on bed topography from BedMachine v3.7 (outside IGZ) [53] and derived from a WorldView DEM (inside IGZ) assuming flotation color coded from -2000 m (blue) to 0 m (white). Star in inset shows where we calculate tides [61] and inverse barometer effect. Black lines are Operation IceBridge (OIB) tracks from 2011-2016. Pink lines are flux gates for ice discharge. White dash lines delineate the drainage basin. (b-d) CSK-derived GL positions (black line) between three states; (e-g) SSH (red dot) at the time of acquisitions in (b-d). Insets shows SSH 12 hours prior and after the 3 (to 4) acquisition times.

with a spatial resolution of 13 × 4 m, respectively, in slant-range (across-track) and azimuth (along-track). ALOS-2 PALSAR operates at L-band (wavelength of 24 cm) with a 41.5° look angle off nadir, 7.5 m × 4.1 m resolution (slant-range × azimuth), a 70 km swath width, and a 46-day repeat cycle. S1 data is acquired at the C-band frequency (wavelength of 5.6 cm), at a 6-day repeat cycle, in Interferometric Wide Swath (IW) mode based on Terrain Observation with Progressive Scans SAR (TOPS) technology [88]. The azimuth spacing is 13.9 m versus a slant-range spacing of 2.4 m, equivalent to a ground resolution of 20 m in azimuth and 5 m in range [85]. CSK is a constellation of 4 × low Earth orbit satellites operating at X-band (wavelength of 3.1 cm) at a slant-range spacing of 3 m and with a 16-day repeat cycle. The SAR images are formed by concatenating 3 × CSK STRIPMAP-HIMAGE overlapping frames, each 40 km × 40 km, at 3 m posting both azimuth and range directions [46]. We difference 3 or 4 radar images to form a DInSAR interferogram that reveals the differential tidal motion of floating ice during 3 to 4 epochs. This approach enables us to separate the short-term vertical motion of the ice caused by tidal flexing from the constant horizontal ice motion between passes [78]. The GL is located at the upstream end of a densely set of interferometric fringes (Fig. 3.2b-d). We map the GL in 88 × high-quality double-difference interferograms. As phase quality varies, GL mapping is not complete in all 88 interferograms. We define GL positions for the years 1996, 2008 and 2009, and an IGZ for the years 2019-2021.

3.3.2 Tidal height calculation and correction

Floating ice flexes in response to variations in oceanic tides and atmospheric pressure. To quantify the tidal state, we use the CATS2008 model, a high-resolution ocean tide model with a precision of 5 cm [61] (Fig. 3.2e-g). We calculate the inverse barometer effect (IBE) correction, at a rate of 1 cm/hPa [62], using anomalies in mean sea level pressure from the fifth generation of ECMWF atmospheric reanalyses of the global climate (ERA5), with

hourly outputs, at 31 km horizontal resolution [31]. We use the mean pressure for the period 2019-2021 as a reference for the anomalies.

3.3.3 Grounding zone length from hydrostatic equilibrium

If ice is in hydrostatic equilibrium, the IGZ length is $\Delta L_{HE} = \Delta h[\beta + \frac{\rho_i}{\rho_w}(\alpha - \beta)]^{-1}$, where Δh is the variation in tidal height, surface α and bed β slopes are determined along the thickness gradients averaged over several ice thickness, and $\rho_i = 917$ kg/m^3 and $\rho_w = 1{,}028$ kg/m^3 are the density of ice and seawater, respectively [108]. To calculate α and bed β, we use BMv3.7 surface elevation in solid-ice equivalent [52]. BMv3.7 employs a mass conservation algorithm in regions of rapid ice flow and a streamline diffusion method elsewhere to reconstruct ice thickness and bed elevation [53]. Downstream of the GL, BMv3.7 matches the International Bathymetric Chart of the Southern Ocean Version 2.0 (IBCSOv2) [18]. Slopes are calculated along the direction of GL migration over a length scale of 3 × ice thickness.

3.3.4 Ice velocity and surface height data

Ice velocity is from MEaSUREs at 450 m grid spacing from 1996 to 2022 [56, 54]. We use measurements of changes in surface elevation from ATL14 (land-ice DEM) and ATL15 (land-ice height change) ICESat-2 gridded products, and MEaSUREs ITS_LIVE Antarctic Grounded Ice Sheet Elevation Change. ICESat-2 yields a foundational DEM at 100-m posting and quarterly elevation-difference surfaces at 1-km resolution that document surface elevation changes in reference to this DEM [101, 102]. MEaSUREs products offer monthly ice sheet elevation changes derived from 5 × radar altimetry missions (Geosat, ERS-1 and -2, Envisat and CryoSat-2) and 2 × laser altimetry missions (ICESat and ICESat-2) at 2 km resolution [58].

3.3.5 Ice mass balance calculation

Using $\partial h/\partial t$ along flowlines, inferred from the ICESat-2 ATL15 and the MEaSUREs elevation change products, our analysis identifies that the IGZ reaches to state 2 starting around 2006 and progresses to state 3 by 2012. Consequently, we select the track locations from the Operation IceBridge (OIB) missions in 2016, 2012 and 2011 to serve as flux gates for the periods 1996, 2006-2011, and 2012-2022, respectively [43]. The OIB missions employ airborne laser altimetry (Airborne Topographic Mapper, ATM) alongside radar depth sounders (Multichannel Coherent Radar Depth Sounder, MCoRDS) to ascertain ice surface elevation and thickness in fine resolution [103, 104, 59, 60, 42]. Leveraging ice thickness acquired from OIB in conjunction with the $\partial h/\partial t$ obtained from ICESat-2 and MEaSUREs, we calculate the ice thickness at the designated flux gates for 1996-2022. By integrating these measurements with velocity in the direction perpendicular to the flux gates, we determine the annual ice discharge. We estimate the uncertainty in ice discharge by considering values located within $\pm$1 km of the flux gates.

Annual SMB in Berry Glacier basin is deducted from the Regional Atmospheric Climate Model Version p2.3 (RACMOp2.3) [110], which provides SMB data at 2-km resolution with 0.1 m/yr error. We use the average SMB from the years 1979-2004 as a reference, $SMB_{1979-2004}$, to calculate anomalies in ice discharge, δD, and SMB, δSMB. Anomalies in total mass balance, $\delta M = \delta SMB$ - δD are independent of $SMB_{1979-2004}$.

3.3.6 Ice bottom and bed topography

We use the ICESat-2 DEM and a WorldView DEM from Sep 6, 2019 to deduce ice bottoms in IGZ based on hydrostatic equilibrium. Along profiles overlapping on OIB tracks, we utilize ice surface elevation from ATM minus thickness from MCoRDS to get the ice bottom. For comparison, we compute the bottom elevations from flotation from ATM surface and a

DEM in the same year of the ATM constructed from ICESat-2 reference DEM and elevation change products. Firn air content is removed with BMv3.7 for all the DEMs. We assume that the actual bed topography coincides with the ice bottom in the IGZ.

Along profiles A-B, C-D and C-F, partial bed layers are marked with question mark because the picked OIB ice bottom is questionable based on MCoRDS echo strength profiles (Supplementary Fig. A.2a-c).

We notice that level 2 data of OIB is not as robust as level 1 data, especially for 2011 OIB. This might be the reason causing hundreds of meters difference between the bed from BMv3.7 and ice bottoms in the IGZ if we use BMv3.7 level 2 data for bed topography.

3.3.7 Ice basal melt rates

Ice basal melt rate is calculated from ICESat-2 products at 100 m grid spacing from 2019 to 2022 [102, 101]. We apply an Eulerian approach to calculate the melt rates at point locations from mass conservation [94] because the ATL15 product only provides a time history of changes about a reference DEM (ATL14 product). In the Eulerian description, the melt rate $\dot{b} = \dot{a} - \frac{\partial H}{\partial t} - (H(\nabla \cdot \mathbf{u}) + \mathbf{u} \cdot (\nabla H))$, where $\dot{a}$ is surface mass balance, H is ice thickness, $\mathbf{u}$ is velocity, $\nabla \cdot \mathbf{u}$ is the velocity divergence, and ∇H is the thickness gradient. This approach requires spatial filtering to mitigate the effect of ice thickness heterogeneities travelling along the glacier. We use a spatial filter of 5 km. We assume that ice is in hydrostatic equilibrium within the IGZ because the ice surface is lifted up at high tide from seawater intrusion and the ice surface is within 1 to 2 m of flotation (Fig. 3.2). Since the ice in the IGZ is not completely floating, the melt rates calculated with hydrostatic equilibrium may be overestimated, and the degree of overestimation depends on how flotation actually works within the IGZ. Using DEMs with a one-year time separation, we define a "limit of viability" zone that excludes ice elements that were fully grounded during the integration

period, i.e., a zone equal to half the annual displacement in IGZ length (Fig. 3.7b). The surface elevation changes are combined with SMB data from RACMOp2.3 (0.1 m/yr error). Flow divergence is calculated using annual ice velocities (1 m/yr error).

3.4 Results

3.4.1 Grounding line migration

Using interferometric SAR data, we find that the length of the IGZ increased from 0.6-km in 1995/1996 to 18.0±0.9 km in 2020-2021 (Fig. 3.2). The length of the IGZ in 2020-2021 ranks among the longest in Antarctica [21, 13, 51]. Calculations of ice thickness assuming hydrostatic equilibrium [108] from the surface elevation in BedMachine v3.7 (BMv3.7) [52] indicate that the IGZ should only be 150-200 m long (Fig. 3.3). This discrepancy imposes a major revision of the bed topography, which is not derived from mass conservation in this region in BMv3.7 but interpolated.

In terms of long-term migration, the upper limit of the GL retreated 18.1±0.4 km from 1996 to 2021, i.e. the lower portion of the 2021 IGZ occasionally matches the upper limit of the 1996 IGZ. During 2009-2021 alone, the GL retreated 7.0±0.4 km, or 0.5 km/yr (Fig. 3.2) and also migrated laterally 3 km to the West into a tributary glacier.

We find an excellent agreement between the vertical motion of the ice surface measured with double-difference InSAR (DInSAR) and changes in oceanic tide calculated using the CATS2008 tidal model [61] corrected for changes in atmospheric pressure, or inverse barometer effect (IBE), calculated using ERA5 pressure fields [31], i.e., a net change in sea surface height (SSH) (Fig. 3.3c). We find no correlation between the GL position and SSH (Fig. 3.3d), however, i.e., the GL does not migrate in phase with SSH. Instead, the GL oscillates

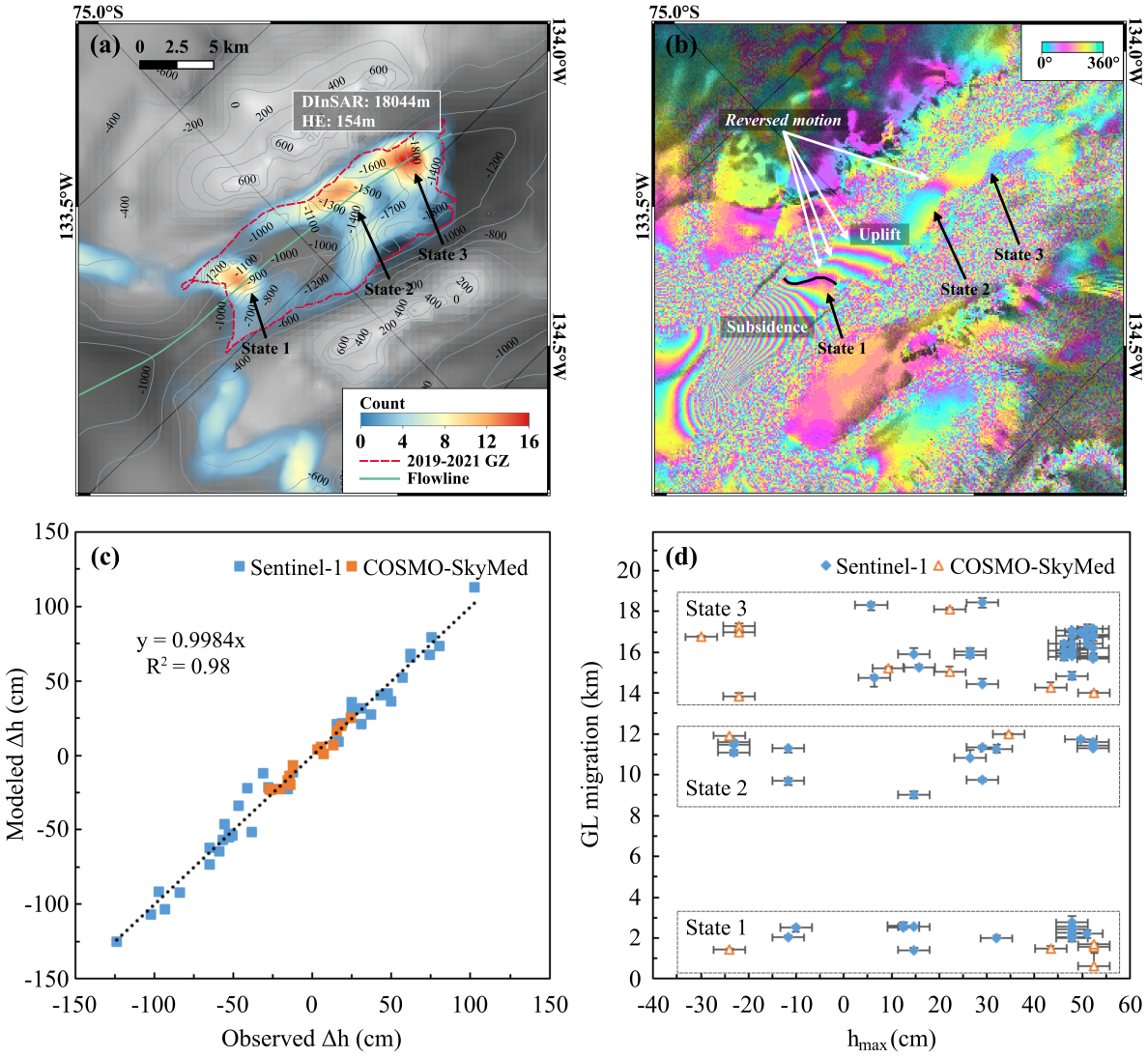


Figure 3.3: **Grounding line migration of Berry Glacier, West Antarctica.** (a) GL density and IGZ (red dotted line) in 2019-2021 and center flowline (green) overlaid on bed topography; (b) Sentinel-1 double-difference InSAR with GL position (black) and deformation fringes upstream revealing that water trapped in the previous cycle is moving out; (c) modeled differential SSH versus InSAR observations; (d) GL position versus maximum SSH for three states during the 3 (to 4) acquisition times.

between three states: 1) state 1 near the 1996 IGZ, 2) state 2 along a retrograde portion of the new bed about 6 km upstream of state 1, and 3) state 3 at the southern limit of the 2021 IGZ or another 2 km further inland. The three states stand out in the density map of GL positions (Fig. 3.3a). The GL is predominantly in state 1 in 1996, reaches state 2 around year 2008, and spends most of its time around state 3 in recent years.

3.4.2 Ice dynamics

We compare the GL retreat over the time period 2006-2022 with changes in ice surface elevation, h, ice thickness, H, and ice speed, V. Between state 1 and 2, h decreased by 24 m, equivalent to a reduction in thickness H of 222 m, or a 13 m/yr thinning in H, increasing to 35 m along the west flank, or a 19 m/yr thinning in H (Fig. 3.4a). The glacier speed increased by 65 m/yr at the center versus 136 m/yr on the west flank (Fig. 3.4b). The glacier speed is maximum (760 m/yr) between the 1996 and 2008 GLs (Supplementary Fig. A.1), but changes in speed and elevation in that region are small (Supplementary Fig. A.1a-c). Glacier speed up is detected principally from the 2008 GL up to 28 km past the upper part of the 2021 IGZ (Fig. 3.4b). The speed up averages 134 m/yr with a maximum at 224 m/yr. The surface elevation decreased by 36 to 59 m (Fig. 3.4a). Along profile G-H, the surface elevation decreased and the glacier speed increased, with the largest change at the IGZ boundary with 290 m thinning and a speed up from 448 to 665 m/yr, or 48% (Fig. 3.4c,e). Along profile C-D, the speed accelerated by 52% from 1996 to 2022, accompanied by rapid thinning, especially on the central and western sides (Fig. 3.4d,f). On average, the glacier thinned by 17±1 m/yr (h change of 47±3 m) and sped up by 64±5%. The pattern of thinning does not coincide exactly with the pattern of speed up, in part because the retreat expands laterally along slower-moving tributaries [89].

As a result of thinning and speed up, we calculate that anomalies in ice discharge increase

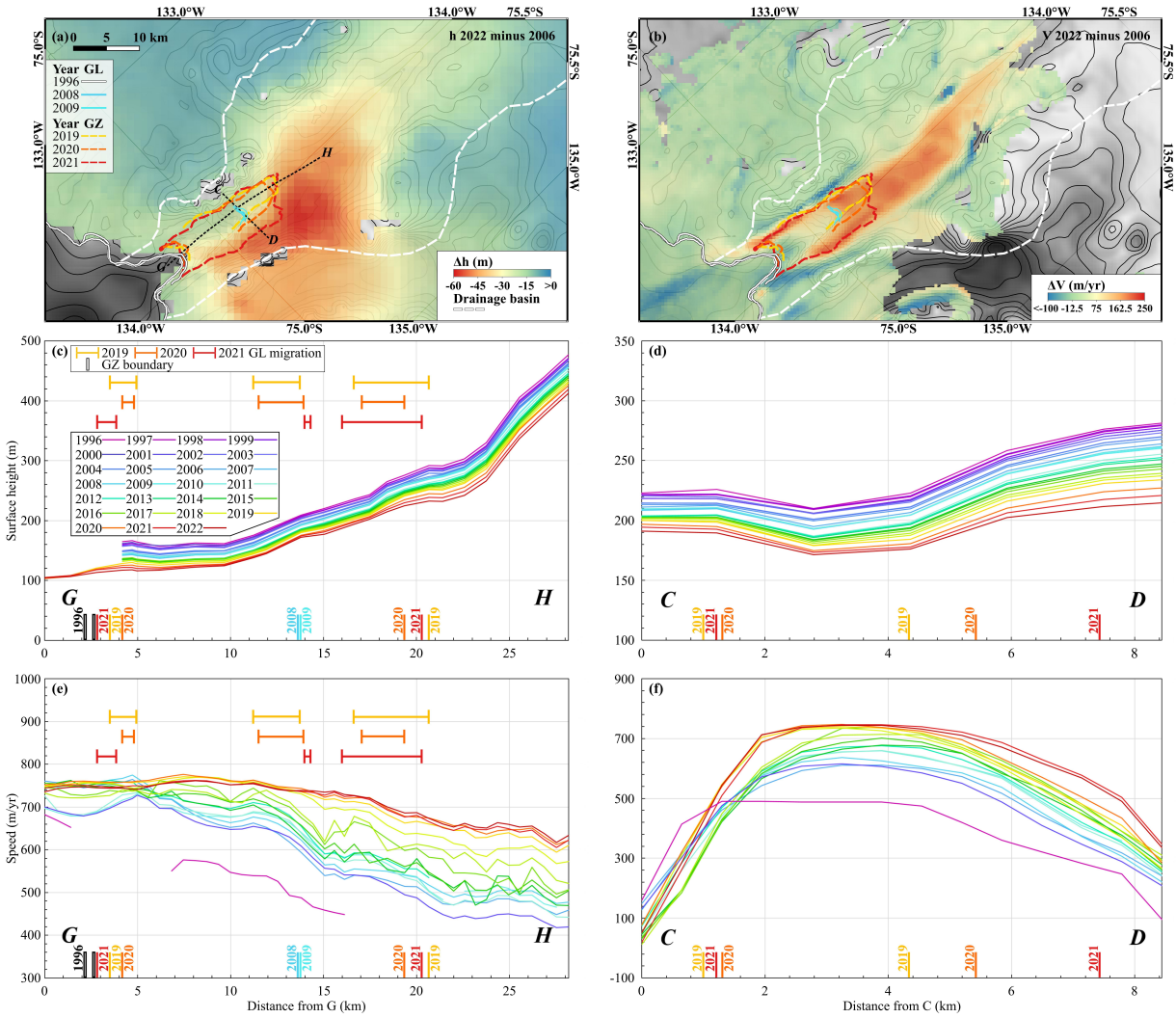


Figure 3.4: **Spatial and temporal changes in surface elevation, h, and speed, V, of Berry Glacier, West Antarctica.** (a) h and (b) V between 2006 and 2022 with GLs in 1996 (white)/2008 (blue)/2009 (cyan) and IGZ boundaries in 2019 (yellow)/2020 (orange)/2021 (red). Year 2006 is the reference for (a-b); (c,d) h along profiles G-H and C-D from 1996 to 2022 with IGZ boundaries (vertical and horizontal bars); (e,f) V along profiles G-H and C-D for year 1996 to 2022 (gaps in 1997-2005, 2007 and 2013).

from 0.9 Gt/yr in 1996 to 7.5 Gt/yr in 2022 (Fig. 3.5a). The anomalies in surface mass balance remain stable at -0.5 Gt/yr for 1996 to 2022 versus the reference period of 1979-2004 (Fig. 3.5a). For the period 1996-2022, annual anomalies in mass balance, M, therefore increase from -1.3 Gt/yr to -8.6 Gt/yr, or a factor 6.6, which is considerable compared to other glaciers in Antarctica [79]. In 25 years, Berry Glacier has lost a cumulative mass of 131±23 Gt (Fig. 3.5b), with 90% due to the increase in ice discharge (118±8 Gt; Fig. 3.5b).

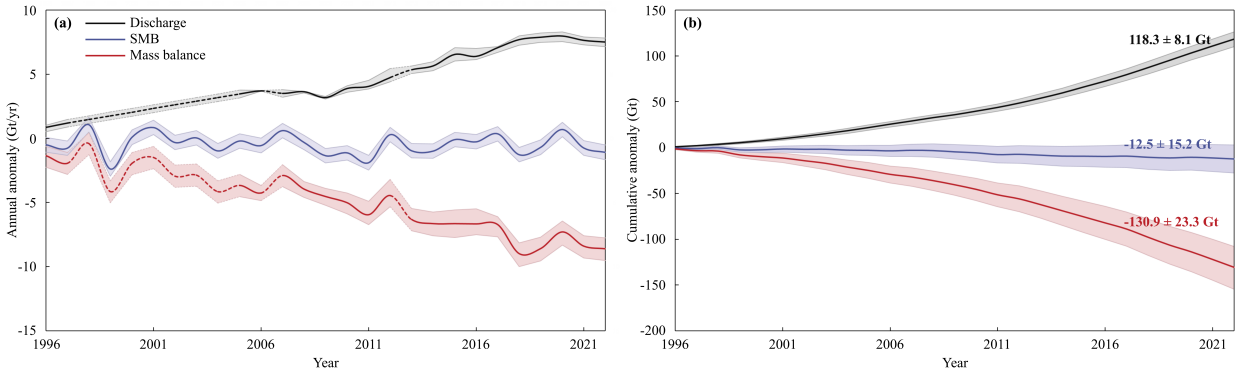


Figure 3.5: **Cumulative anomalies in ice discharge (D), surface mass balance (SMB), and mass balance (M) of Berry Glacier, West Antarctica from 1996-2022.** (a) Annual anomalies in D, SMB and M with error bars in gigatons. Linear interpolation is used to fill discharge gaps (dashed) in 1997-2005, 2007 and 2013; (b) cumulative anomalies in D, SMB and M for 1996-2022. The balance discharge is $SMB_{1979-2004} = 4.3 \pm 0.2$ Gt/yr.

3.4.3 Implications for bed topography

We reconstruct the bed topography based on the minimum depth of ice that ensures flotation over areas where we detect ice flexing during the tidal cycle. Ice base elevations deduced from ICESat-2 and WorldView (WV) digital elevation models (DEMs) are consistent with one another (Fig. 3.6a) and the same applies for ATM 2009-2019 data and reconstructed DEMs of the same period (Fig. 3.6b). The calculated basal elevations are, however, much lower, up to 1,300 m, than those reconstructed in BMv3.7 (Fig. 3.6). The bed elevation from BMv3.7 matches MCoRDS thickness profiles only in the upstream part of the 2021 IGZ (Fig. 3.6a), which indicates that some OIB thickness profiles may have been misinterpreted

as too shallow. Indeed, a closer inspection of the OIB radar echograms indicates only weak bed returns at the glacier center, hence a large uncertainty in bed depth (Supplementary Fig. A.2). Here, we deduce a much deeper bed that turns out to be more consistent with a prior gravity inversion [15].

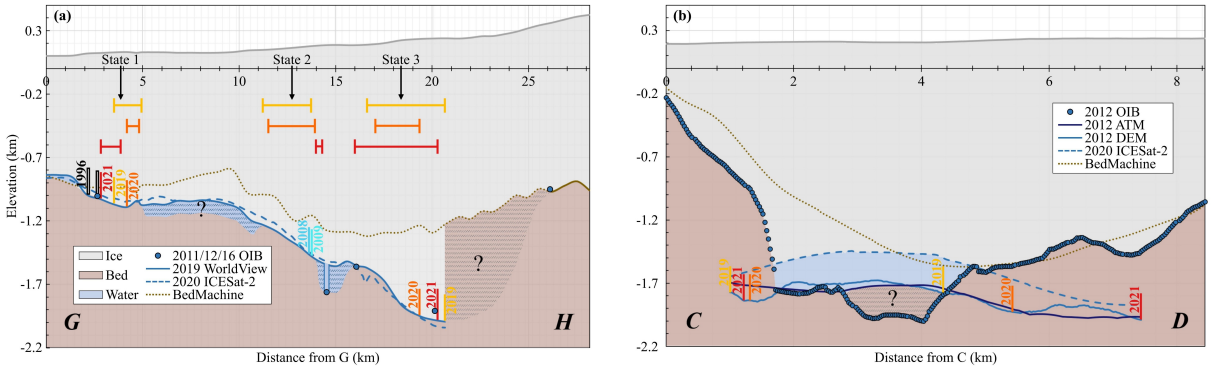


Figure 3.6: **Surface elevation, h, and bed topography, b, along the profiles.** (a,b) h (grey line) from WorldView (WV) (a) and Airborne Topographic Mapper (ATM) (b), ice draft (blue line) deduced from WV (a) and a DEM (b), and bed elevation, b (brown line) from BMv3.7 along G-H and C-D. Blue dash line marks flotation from ICESat-2 on Jan 1, 2020; blue solid line is ice bottom deduced, respectively, from WV on Sep 6, 2019 (a) and a DEM from ICESat-2 (b); dark blue line is ice bottom deduced from ATM in 2012 (b); blue dot is ice bottom from OIB. Dots in (a) are respectively for Nov 5, 2016 (state 1), Oct 27, 2012 (near state 2), Nov 2, 2016 (between states 2 and 3, and outside IGZ) and Oct 17, 2011 (state 3). Acquisition time of the dots in (b) is Oct 27, 2012 as well.

Comparing the spatial distribution of GL positions with the new bed topography along profile G-H (Fig. 3.6a), we find that the GL has migrated over a mostly retrograde bed. A series of bed depressions between the three states creates zones of apparent water trapping at low tide. Water trapping is expected from a resistance to outflow from the hydrological network and along-slope gravity gradients as in [114]. In several interferograms where the GL stands at state 1 or 2, we detect fringes of opposite sense motion upstream, e.g. 11.5 cm (3.7 fringes of S1 DInSAR) in Fig. 3.3b, which indicate the draining of seawater trapped during a prior tidal cycle.

3.4.4 Basal melting regime

Basal melt rates, $\dot{b}$, may be calculated from a mass conservation approach using ice velocity, thickness, and surface mass balance [94]. We use a time series of yearly change in ice surface elevation from ICESat-2, surface mass balance data from RACMOp2.3, ice velocity from MEaSUREs, ice thickness from hydrostatic equilibrium, and an Eulerian framework for mass conservation. We find that the highest melt values in the entire Getz Ice Shelf domain are recorded in the IGZ of Berry (Fig. 3.7). The basal melt rate ranges from -30 to 90 m/yr in the IGZ and averages 49 m/yr over the IGZ area of 26 km^2. High values are found along steep retrograde slopes. Low values are found on flatter parts of the bed and at the locations of the bed ridges that control the 3 GL states.

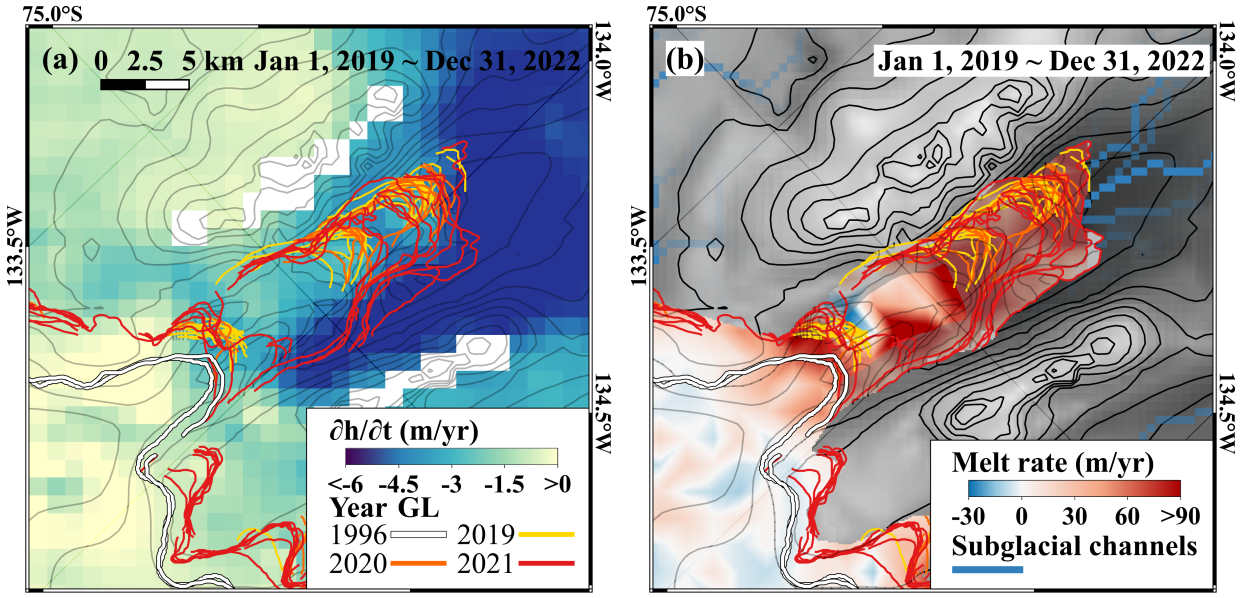


Figure 3.7: **Height-change rate, $\partial h/\partial t$, and basal melt rate, $\dot{b}$, of Berry Glacier, West Antarctica from 2019-2022.** (a) $\partial h/\partial t$ from 2019 to 2022 color-coded from -6 to 0 m/yr with the GL positions of 1996 and 2019-2021; (b) $\dot{b}$ from 2019 to 2022 with the GL positions and limit of viability of the calculation (translucent grey) overlaid on bed topography with 100-m contours.

Over the past 25 years, a cavity several 100 m's thick has formed beneath Berry, up to 300 m in thickness near state 2 (Fig. 3.6b, Supplementary Fig. A.3b-d). A time series of Landsat

images confirms that anomalies, or bumps, in surface elevation present in the earlier part of the record, indicative of a grounded part of the glacier, progressively disappear in the region of ungrounding, consistent with ice becoming afloat (Supplementary Fig. A.4).

3.5 Discussion

Warm, dense CDW is present on the continental shelf in front of the ice shelf to provide a source of ocean heat [34]. The bathymetry on the continental shelf in front of Berry includes favorable, deep, wide channels for CDW to reach Berry. We delineate a thalweg along the western Getz from the ice shelf front to east of 134°W and Berry that likely provides access of CDW to the IGZ [15] (Supplementary Fig. A.5). Warm water with a salinity of >34.5 psu and bottom temperature of 0.5–0.9°C is present at the front of the western Getz [5, 49]. A time series of CTD measurements also shows that ocean temperature at 1,000 m depth at the ice shelf front increased from 0.1°C in 1994 to 0.7°C in 2007 [34], i.e., the ocean heat flux reaching Berry must have increased during that time period. We compare the melt rates within 10 km downstream of the IGZ on the west Getz Ice Shelf from 2019-2022 (this study) with rates inferred for the 2003-2008 [74] and 2010-2018 time periods [1]. We note that the previous results do not cover the IGZ of Berry because it was not known at that time. The results show that the melt rate near the IGZ of Berry has been increasing from 9.1 m/yr in 2003-2008 to 14.9 m/yr in 2019-2022. The melt values are much higher than for other glaciers and the difference has increased with time, from 1.3 × larger in 2003-2008 to 1.7 × larger in 2019-2022 when we compare Berry with DeVicq Glacier, the largest neighboring glacier flowing into Getz (Supplementary Fig. A.6). The melt rates in the IGZ of Berry are the largest of the entire Getz Ice Shelf.

From the vertical motion of ice measured with interferometry (Fig. 3.2b-d), we estimate the thickness of seawater intrusions in the IGZ to vary from 0 at state 3 to the full tidal range

at state 1 or 0.6 m. The vertical displacements at the entry of the IGZ of 1, 4 and 4.7 CSK fringes translate into a change in water column of 1.4, 5.5 and 6.5 cm, respectively (Fig. 3.21b-d). With a tidal amplitude of ±0.6 m, we expect the average water thickness of the intrusions to be about 0.6 m (from 1.2 m at the entrance to 0 m at the end). With an IGZ 114 km^2 in size, the water flux will be 6.9×10^7 m^3 in 6 hours, with a density of 1,028 kg/m^3. The ocean thermal forcing is +3.6°C at 1,000 m depth based on the CTD from 2018. These values yield an ocean heat transfer of 1×10^{15} J. If all of the heat is used to melt ice, we get a maximum freshwater flux production of 141 mSv or an average melt rate of 39 m/yr within the IGZ. This value is lower than our inferred melt rate from remote sensing of 49±18 m/yr, but within error bars. More likely, the effective thickness of the water intrusions is larger than 0.6 m and the melt process has an efficient closer to 20-30% [25].

Our results have major implications for ice sheet modeling. Most ice sheet models do not account for a short-term variability in GL position and assume zero melt at the GL [93]. Our observations show that this is not the case for Berry Glacier. Instead, we find an 18-km long IGZ that experiences some of the largest melt rates of the entire Getz Ice Shelf, about 49 m/yr on average. If the inflow of warmer CDW increases, the melting of basal ice increases, basal friction is reduced over a large area, which may explain the retreat, speed up, thinning, and further retreat of the glacier.

Pioneer modeling studies [64, 113, 81] have already shown that including km-scale seawater intrusions in an ice sheet model increases the projections of mass loss, sometimes considerably, by a factor two. The same conclusion should apply for Berry Glacier. Prior ocean modelling studies have also shown that ice-ocean interaction in a coupled ocean-ice model are less efficient than in models using a parameterized melting rate [91]. This situation is also applicable to Berry Glacier because the new ice shelf cavity formed over a complex bed topography, thereby yielding an IGZ of exceptional length. This region awaits more detailed surveys to better constrain the shape of the cavity and the ocean state in the cavity.

3.6 Conclusions

A detailed mapping of the GL migration of Berry Glacier, West Antarctica, reveals a rapid retreat (0.7 km/yr) that created a new ice shelf cavity and an 18.0±0.9-km wide IGZ along a region of mostly retrograde bed slopes, with a bed topography far deeper than previously known. The non-linear GL migration with changes in sea surface height suggests that seawater intrusions, while extending 18 km, are not totally efficient and can lead to seawater trapped during extrusion, as manifest by the three GL positions along the ice shelf cavity. With the rapid retreat of the IGZ, the glacier has lost a considerable amount of mass, sped up by 64% and retreated 18 km. The mass loss extends far into the basin of Berry Glacier. The rapid retreat of the glacier is attributed to increased oceanic heat flux from warm CDW, which was facilitated by the presence of favorable bathymetric channels on the continental shelf that directed this water into the ice shelf cavity. Additionally, the presence of vigorous kilometer-scale intrusions beneath the glacier significantly enhanced the melt rate, leading to more rapid melt in comparison to neighboring glaciers.

Chapter 4

Melt rates in the kilometer-size ice grounding zone of Amery ice shelf, East Antarctica

4.1 Abstract

The grounding line (GL) marks the transition boundary between grounded and floating ice. Ice that crosses the GL becomes afloat in the ocean waters and displaces sea level. The short-term variability of GL defines what we call an "Ice Grounding Zone (IGZ)". The melt rate at the junction of the ocean with grounded ice or within the IGZ is, however, not well known. Here, we employ a time series of satellite radar interferometry data from Sentinel-1 to document the GL migration, and data from ICESat-2 mission to derive the basal melt rates of Amery Ice Shelf, in East Antarctica. We confirm a kilometer-long (10-15 km) IGZ, which is two orders of magnitude larger than expected for GLs on a hard bed. Over 2019-2022, the highest ice shelf melt rates are recorded within the IGZ overlaid on estuaries with

values from 31±11 to 255±51 m/yr while the melt rates stay low on the floating ice shelf (9 m/yr). Such high melt rates brought by high speed of seawater intrusions in kilometer-long IGZs contrast with the traditional plume model of GL melt which predicts zero melt. High rates of simulated basal melting in grounded glacier ice in numerical models will increase the glacier sensitivity to ocean warming and potentially double projections of sea level rise.

4.2 Introduction

The Antarctic Ice Sheet has experienced significant ice loss over the past few decades, contributing notably to global sea level rise (SLR). Since 1992, the Antarctic Ice Sheet has contributed approximately 7.6 mm to global SLR [106]. This mass loss is primarily driven by enhanced basal melting due to warmer ocean temperatures and ice discharge from the margins of the ice sheet, with relatively minor contributions from changes in surface melt or snowfall accumulation [79]. The primary cause of ice loss has been the incursion of warm Circumpolar Deep Water (CDW) beneath the floating ice shelves, which leads to increased basal melting and the subsequent retreat of grounded ice [86, 37]. This process is further exacerbated by the weakening of ice shelves, which reduces their buttressing effect, allowing the grounded ice to flow more rapidly into the ocean [84]. For glaciers that terminate in floating ice shelves rather than directly calving into the ocean, the physical mechanisms driving ice loss are complex and challenging to observe, but they are believed to be similar in nature [69]. Warmer ocean waters that erode the base of grounded ice reduce the resistance to flow, causing the glaciers to accelerate and contribute to SLR. Most ice sheet models include parameterizations of basal melt, often assuming negligible melt at the grounding line (GL), particularly when the GL remains stable and does not migrate with tidal influences [20, 92]. It has been specifically recommended that models avoid applying melt in mesh elements that span the GL [91].

Previous modeling studies have raised questions about the assumption of a GL with zero melt. A coupled glacier–ice shelf–ocean plume model was employed to consider oceanic influence extending several kilometers upstream of the GL, rather than just hundreds of meters [64]. At that time, indirect evidence included bright radar reflections from sounding echoes upstream of the GL, suggesting the presence of seawater extending inland beneath the ice for several kilometers, which gradually faded to weaker reflections typical of ice overlying a thin layer of freshwater [116]. Model simulations indicated that applying ice melt across kilometer-scale ice grounding zone (IGZ) would significantly reduce glacier stability and double the mass loss compared to that predicted by standard simulations. A flexural model of elastic ice on an elastic bed was developed, which proposed that kilometer-scale intrusions of seawater at tidal frequencies could occur along subglacial water channels upstream of the GL, driven by variations in ice flexure [113]. More recently, layered seawater intrusions under grounded ice got simulated and such a configuration was estimated to increase mass loss by up to a factor of two [81]. Despite these advances in modeling, the physical processes driving melt under the grounded portion of the Antarctic Ice Sheet are still represented in simplified forms in many ice sheet models, typically assuming a GL with no melt [10].

Several recent studies utilizing radar interferometry data have identified the presence of broad, kilometer-scale IGZ in Antarctica, particularly on Pine Island Glacier [46], Thwaites Glacier [47], Getz Ice Shelf [51], and other regions of the continent. For Thwaites Glacier, thinning rates observed over time using TanDEM-X digital elevation models (DEMs) indicated significant basal melt in regions where the glacier has recently ungrounded [47].

In this work, we employ a time series of dense, high-resolution observations of ice motion from Sentinel-1 (S1) and ice surface elevation from ICESat-2 mission to document the GL variability of the Lambert-Mellor-Fisher Glaciers system, a major marine-terminating glacier system feeding into the Amery Ice Shelf in East Antarctica (Fig. 4.1). The Amery Ice Shelf is one of the largest ice shelves in Antarctica, draining an area of approximately 1,432,000 km^2

through the Lambert Glacier, which is the largest glacier in the world by volume [22]. The ice volume of the Lambert Glacier alone is significant, with its drainage basin contributing substantially to potential global SLR [79]. Together with neighboring glacier systems, such as the Mellor and Fisher Glaciers, the region represents a critical area for understanding potential rapid SLR from Antarctica due to its extensive grounding below sea level [74]. Until recently, the Amery Ice Shelf system was considered relatively stable, with the GL showing minimal movement. However, observations have indicated that the GL of the Lambert-Mellor-Fisher Glaciers system migrates at kilometer-scale in 2018 [13]. This migration has been attributed to a combination of factors, including warmer ocean waters intruding beneath the ice shelf and increasing air temperatures in the region, which have accelerated basal melting and contributed to the destabilization of the glacier system [79]. Additionally, the floating ice shelf, which plays a crucial role in buttressing the grounded ice, has shown signs of thinning, further contributing to the observed GL retreat [63].

In prior studies, we used differential interferometric synthetic aperture radar (DInSAR) data from S1 to map the short-term GL migration in year 2018. In 2014, the European Space Agency launched the C-band Sentinel-1a (S1a) satellite on a 12-day repeat cycle, which was followed by the launch of Sentinel-1b (S1b) in 2016. Together, S1a and S1b provide a 6-day repeat cycle, delivering the first continuous stream of DInSAR data with such temporal frequency. Here, we used 140 scenes of S1 data from 2019 to obtain the changes in IGZ between different years.

To map the ice sheet surface elevation, we use a monthly time series of surface height changes from the National Aeronautics and Space Administration (NASA) ICESat-2 mission for the period 2019 to 2022 [102, 101]. In combination with ice velocity and surface mass balance, these data are employed in a Eulerian mass conservation framework to calculate ice shelf melt rates [94]. Previous attempts at mapping ice shelf melt rates using optical-derived DEMs conservatively stopped several kilometers seaward from the GL to be sure to remain

in a region of hydrostatic equilibrium [117]. Here, we delineate the IGZ, i.e., a region of tidal migration of the GL caused by seawater intrusion, and we calculate basal melt rates in the kilometer-size IGZ.

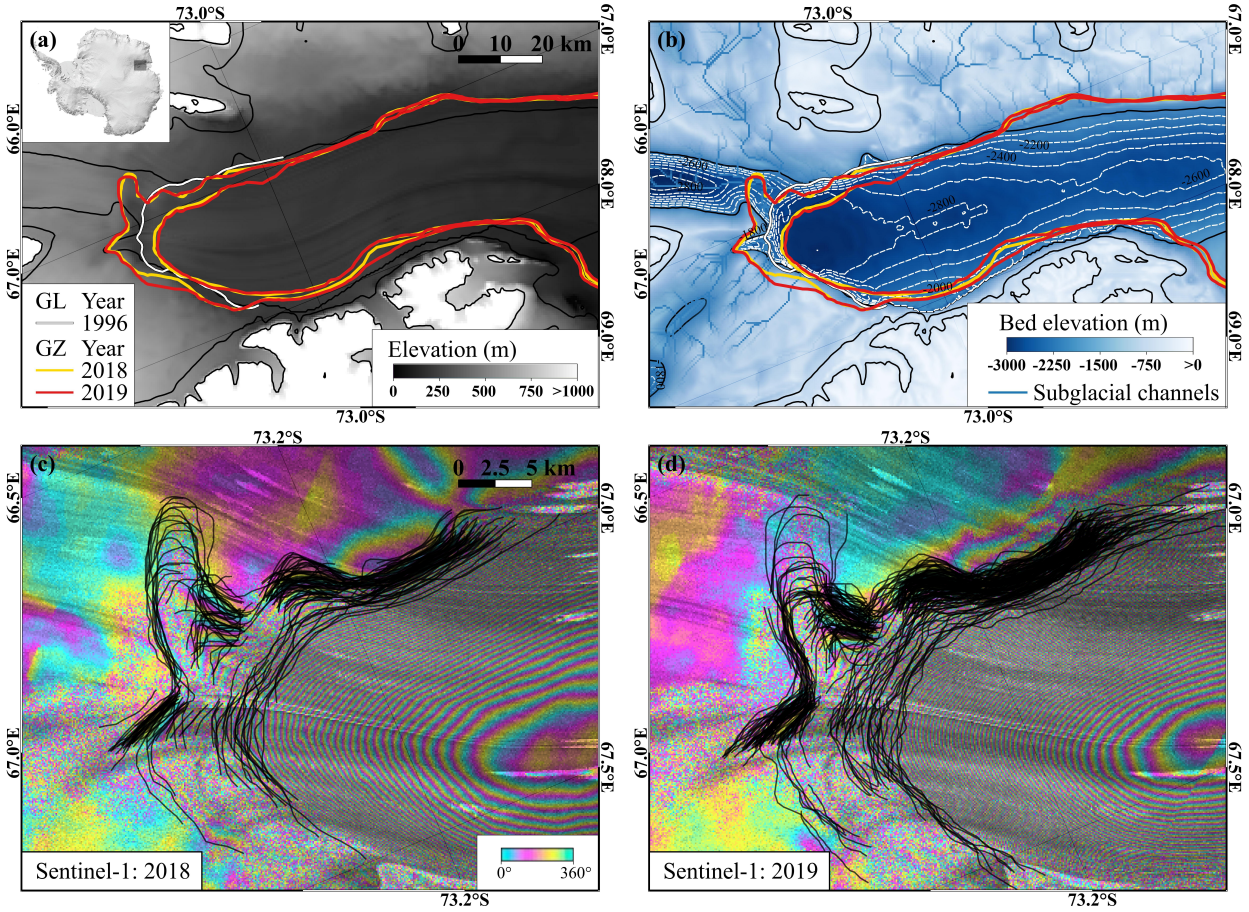


Figure 4.1: **Multi-year grounding line positions of Amery Ice Shelf, East Antarctica.** (a) Ice grounding zone color-coded from 2018 to 2019 with one GL reference from 1996 overlaid on surface topography from BedMachine v3.7 (BMv3.7) [53]; (b) bathymetry from BMv3.7 color-coded from 0- (white) to 3000-m depth (dark blue), with 200-m depth contours and subglacial channels (blue); differential radar interferograms and corresponding grounding line positions from (c) 2018 and (d) 2019 from Sentinel-1.

4.3 Data and Methods

4.3.1 Ice grounding zone mapping

We use mappings of the GL from S1 double-difference interferograms acquired from 2018-2019 on 6-day repeat cycle to delineate IGZ. From 2018 to 2019, the IGZ remains stable (Fig. 4.1). Therefore, we use the differential interferograms together from 2018-2019 to define the IGZ since 2018.

4.3.2 Ice velocity

We use measurements of annual ice velocity from MEaSUREs at 450 m grid spacing from 2019 to 2022 [56, 54]. Velocities are used to calculate flow divergence.

4.3.3 Ice melt rates

The Eulerian approach is applied to express mass conservation on floating ice shelves and infer bottom melt rates, which calculates melt rates at specific locations using mass conservation principles [94]. This method necessitates spatial smoothing to mitigate the impact of heterogeneity in ice thickness as the glacier moves. A spatial filter of 4,500 meters is employed for this purpose. To achieve precise melt rate estimates, a time separation of one year between observations is desirable. The approach operates under the assumption that the ice is in hydrostatic equilibrium. Within the IGZ, ice is in hydrostatic equilibrium because the ice surface is lifted by seawater intrusion during high tide, maintaining the ice surface within 2 to 3 meters of flotation (Fig. 4.2). For DEMs separated by one year, we eliminate a "limit of viability" zone to exclude ice elements that were fully grounded during the integration period, defining this zone as half the annual displacement in length (Fig. 4.2).

Elevation changes derived from the ICESat-2 are combined with surface mass balance data from RACMOv2.3p, which has an error margin of 0.1 m/yr [110]. Ice flow divergence is calculated using annual ice velocity data, with an error margin of 1 m/yr. To assess the uncertainty in melt rate estimates, we assume that the errors in the components of the mass balance equation are uncorrelated, unbiased, and follow a Gaussian probability distribution. This approach yields a mean value of uncertainty range of 36%.

4.4 Results

4.4.1 Ice grounding zones

Compared with the 2018 IGZ [13], the spatial shape and size of the 2019 IGZ remain largely unchanged. In 2019, the longest IGZ measured $15.2^{+0.4}_{-0.7}$ km along the Mellor Estuary (Fig. 4.1), corresponding to a natural pathway on the bedrock that facilitates seawater intrusion and subglacial water outflow. The IGZ length reached a maximum of $12.4^{+0.4}_{-0.6}$ km along the Lambert Estuary (Fig. 4.1). These two extensive IGZs align with prominent inland estuaries, characterized by pronounced valleys in the bed topography extending inland, where the ice is thicker compared to the surrounding regions. The GLs in the Lambert and Mellor Glaciers significantly migrate along areas of retrograde slopes, where bed elevation decreases in the inland direction. In contrast, the migration is less pronounced in other areas where the bed slope is prograde.

4.4.2 Basal melting and ice dynamics

The melt rates derived from the time series of surface height changes from ICESat-2 data, analyzed with an Eulerian approach, indicate that the highest melt rates are recorded within

the ice shelf IGZ, rather than farther out on the ice shelf. The most intense basal melting is observed in the Lambert Glacier (LG) and Lambert Estuary (LE) regions, where average melt rates reach 173±43 m/yr, with peak values around 255±51 m/yr (Fig. 4.2, Fig. 4.3). This highlights the significant vulnerability of this sector to ocean-driven melt processes. On the east side of Mellor Estuary (ME), another high melt region is identified, with average rates of 101±35 m/yr (Fig. 4.2, Fig. 4.3). Moving westward from the west side of ME, basal melt rates decrease markedly, which is likely due to lower thermal forcing brought by the shallower bed elevation in the west, as well as the Coriolis force driving relatively warm water into the IGZ from the eastern part of the system and out from the west, melting the grounded ice as it passes through. In the Mellor Glacier (MG) and Fisher Glacier (FG) regions, basal melt rates average 48±17 m/yr and 34±12 m/yr, respectively, though these rates remain higher than the melt rates on the floating ice, which average 9 m/yr (Fig. 4.2, Fig. 4.3). The results from 2019 to 2022 remain consistent even when applying different levels of spatial smoothing (4,000, 5,000, and 5,500 m).

We analyze the cumulative thinning of points within the IGZ (Fig. 4.4d-g). Point LG, located at the center of the IGZ of Lambert Glacier, thinned at 0.2±0.1 m/yr, while point MG, at the center of the IGZ of Mellor Glacier, thinned at a rate of 0.7±0.1 m/yr (Fig. 4.4). Given that these two points are partly afloat, the surface thinning of 0.8 m and 2.8 m over four years, respectively, translates into a total thickness reduction of 7.4 m and 26.0 m. However, these values are significantly lower than what would be expected from basal melting alone. We attribute this discrepancy to dynamic thickening, i.e., a longitudinal convergence of grounded ice caused by ice flow deceleration (Fig. 4.4c). As the ice flows from land to sea, it moves over a prograde slope at the two estuaries, causing a reduction in ice flow speed. This convergence can substantially counterbalance the thinning effects caused by basal melting.

At point ME, the most significant thinning rate of 1.5±0.1 m/yr is observed (Fig. 4.4),

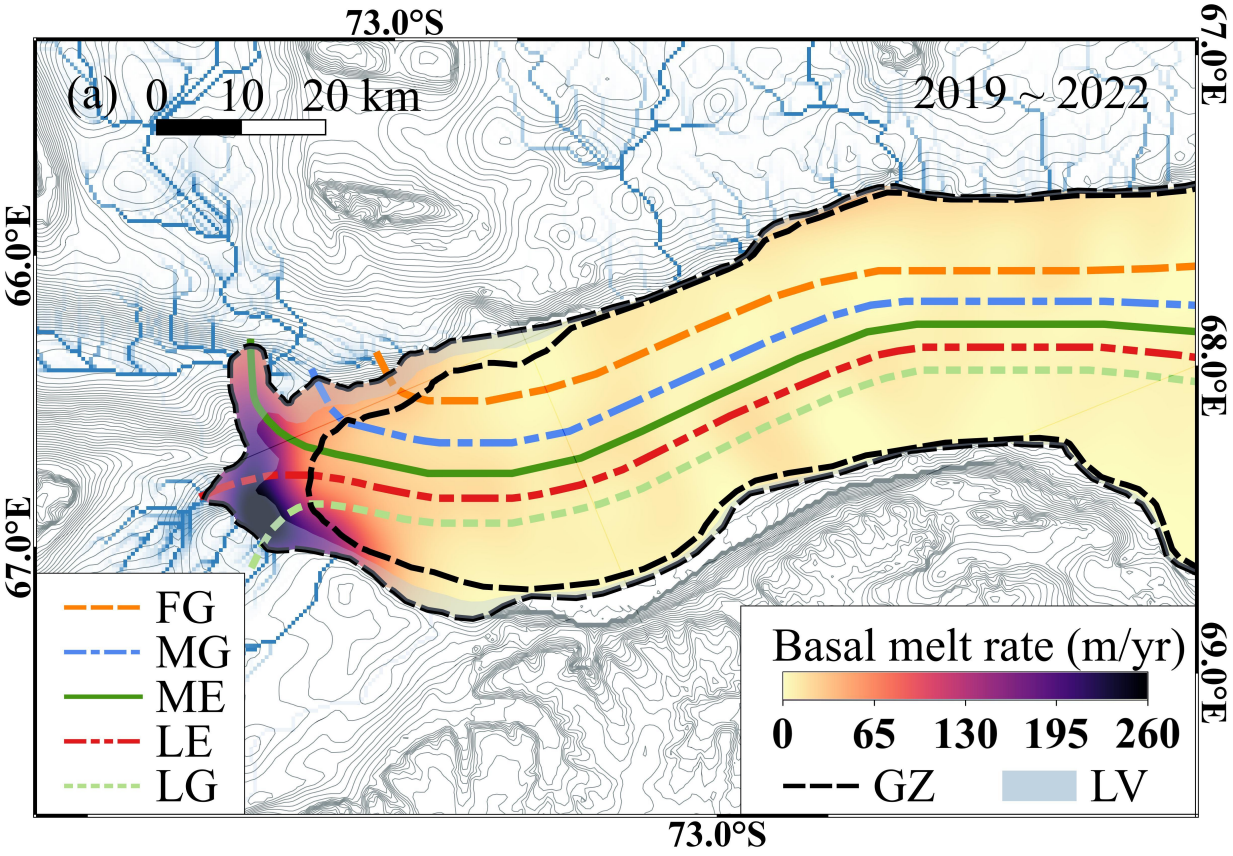


Figure 4.2: **Basal melt rate, $\dot{b}$, of Amery Ice Shelf, East Antarctica from 2019-2022.** $\dot{b}$ in meters per year on the floating ice of Amery Ice Shelf, East Antarctica for 2019 to 2022 with ice grounding zone (IGZ, dotted black), limit of viability (LV, translucent blue band), subglacial channels (blue), and profiles for Fisher Glacier (FG, dotted yellow), Mellor Glacier (MG, dotted blue), Mellor Esturary (ME, green), Lambert Esturary (LE, dotted red), and Lambert Glacier (LG, dotted light green).

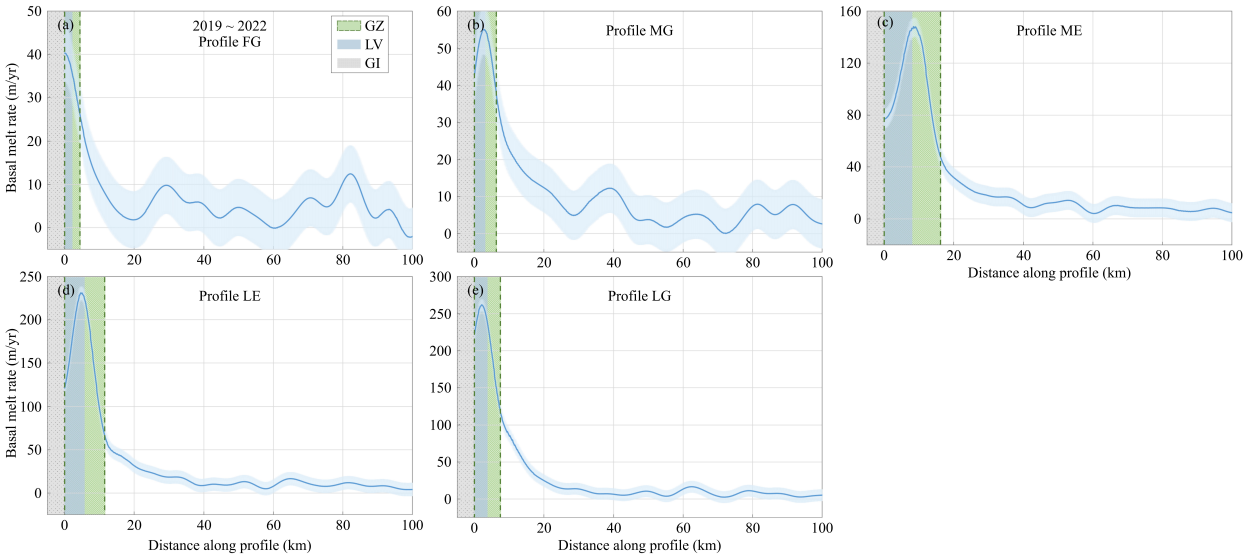


Figure 4.3: **Basal melt rate, $\dot{b}$, along profiles.** (a–e) are $\dot{b}$ calculated along profile (a) FG, (b) MG, (c) ME, (d) LE, and (e) LG. Profile locations are color-coded in Fig. 4.2. In (a–e), the green forward diagonal-hatched column is the ice grounding zone (IGZ), the vertical light blue band is limit of viability (LV), and the grey dotted-hatched column is grounded ice (GI).

suggesting that seawater intrusions may have already penetrated this region. In contrast, point FG shows no change in surface elevation (Fig. 4.4), which we suspect is due to the extreme precipitation brought by atmospheric rivers and the relaxation of bending stresses as the GL retreated. On the one hand, the atmospheric rivers have a disproportionately large impact on precipitation in East Antarctica, especially in the region near the southern extent of the Amery Ice Shelf [115]. On the other hand, the bending stresses typically push the ice below hydrostatic equilibrium just seaward of the GL, and their relaxation may result in a gain or stabilization in surface elevation rather than the expected decrease from ice melt [113]. A similar surface elevation response was observed at Thwaites Glacier, Antarctica, during its retreat, where the ice surface elevation increased downstream of the IGZ, despite radar soundings indicating a reduction in total ice thickness [47]. As bending stresses are not accounted for in our calculations of ice melt, our remote sensing results may underestimate the actual magnitude of ice melt during the retreat.

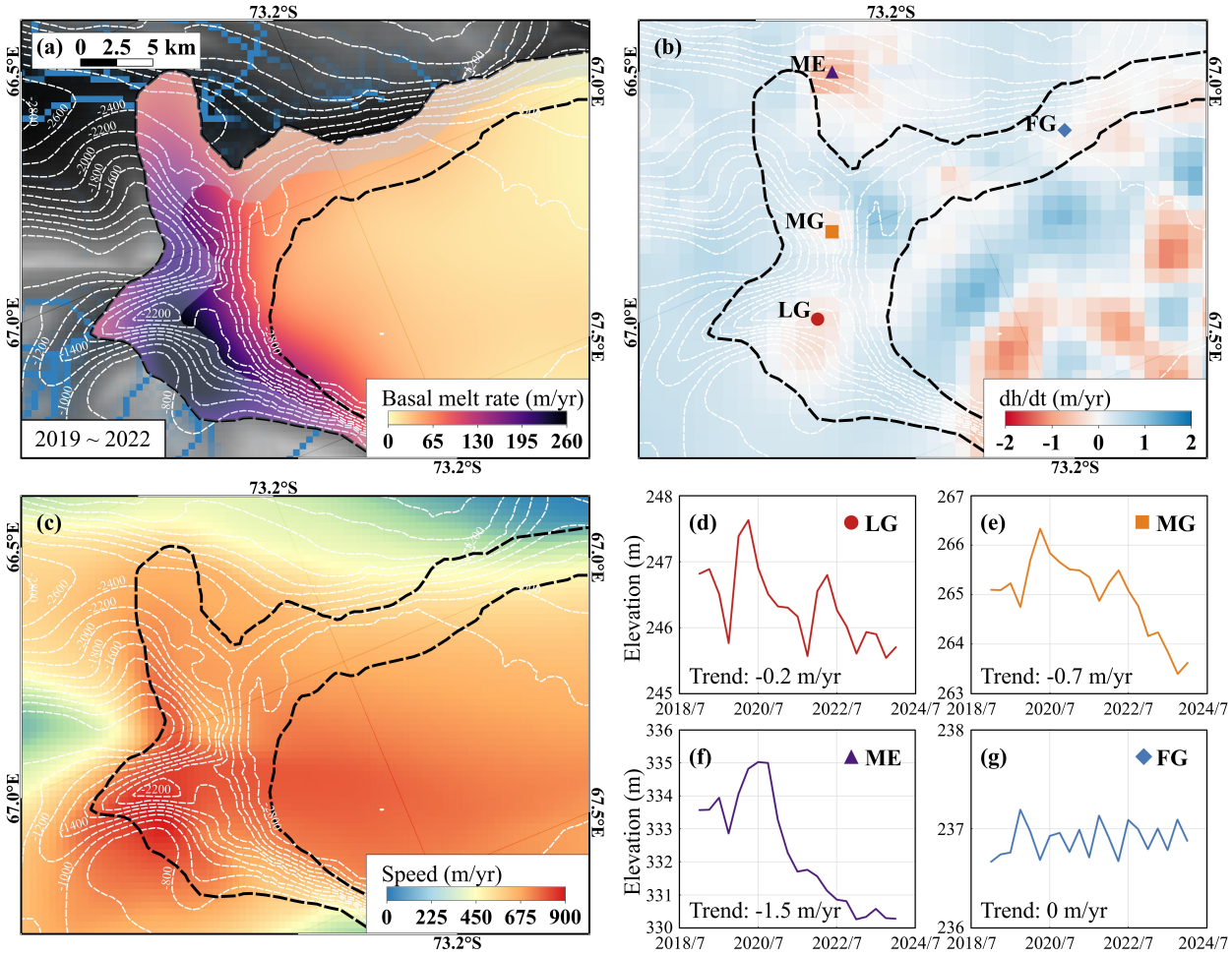


Figure 4.4: **Basal melt rate, $\dot{b}$, height-change rate, dh/dt, and flux divergence, $\nabla \cdot (H\mathbf{u})$, of Amery Ice Shelf, East Antarctica from 2019-2022.** (a) $\dot{b}$ near the ice grounding zone of Lambert-Mellor-Fisher Glaciers from 2019-2022 with the position of the ice grounding zone (dotted line) and limit of viability (blue) for the calculation of melt rates where ice is floating; (b) dh/dt from 2019-2022 color-coded from -2 m/yr to +2 m/yr; (c) $\nabla \cdot (H\mathbf{u})$ from 2019-2022; (d-g) time series of surface elevation at points LG, MG, ME, and FG in (b) to document the ice surface evolution on floating ice (points LG, MG, and FG) vs. grounded ice (point ME).

4.5 Discussion

Our results have significant implications for the modeling of glaciers terminating in ocean waters. Previous efforts to estimate melt rates have typically excluded the region within 5 km downstream of the GL. In this study, we extend these calculations to include the IGZ by documenting the full extent of the GL migration. We exclude from our calculations a narrow band where the ice transitions from grounded to floating within the time separation of the surface height changes, which is approximately one year (with a limit of viability of about 1/2 year of ice motion, as shown in Fig. 4.2, Fig. 4.3). Our findings reveal that the melt rates within the IGZ are, in fact, the highest anywhere on the ice shelf. We are confident that the observed vertical motion of the ice in the IGZ is due to seawater intrusion and not, for example, flexural bending upstream of a fulcrum located at a fixed GL. This is because such ice motion above the fulcrum would produce a vertical displacement opposite in sign to that driven by tidal forces [113].

The traditional plume model for ice shelf melt predicts peak melt rates approximately 10 to 15 km downstream from a fixed GL [100, 99], a pattern not observed in this study. Instead, we observe that the GL of the Lambert-Mellor-Fisher Glaciers system migrates over significant distances in response to tidal forcing, which facilitates the rapid transfer of a large amount of ocean heat beneath the grounded ice. This transfer speed can be approximated by dividing the length of the IGZ by the tidal cycle, approximately 6 hours. Thermodynamics dictates that the ice melt rate is determined by the product of the heat capacity of water, C_p, times the ocean thermal forcing, $T - T_f$, and the entrainment speed, e, of the water along the ice boundary. In the IGZ, the entrainment speed of pressurized water is equivalent to the rate at which the cavity beneath the ice opens, estimated at 15 km in 6 hours, or approximately 70 cm/s. This high flow speed will promote vigorous melt, justifying the elevated melt rates observed in the IGZ. This behavior contrasts with the zero melt assumed at fixed GLs in some ice sheet models. As suggested by previous studies [93, 91, 64, 81], the presence of wet,

broad IGZs has significant implications for SLR projections.

Several modeling studies have suggested that a wide IGZ with high melt rates could potentially double the projections of glacier loss [64, 113, 81, 39]. This heightened sensitivity of the ice sheet to oceanic and atmospheric forcing may help account for the inability of earlier models to replicate the rapid rates of SLR observed during past interglacial periods [29], as well as the generally underestimated ice loss simulated by ISMIP models during the recent historical period [4].

Our results suggest that high melt rates should be applied in kilometer-size IGZs rather than assuming zero melt for the Lambert-Mellor-Fisher Glaciers system. The glacier configurations of Lambert-Mellor-Fisher are not unique to Antarctica and may be representative of many other glaciers terminating in ice shelves across the continent, as well as similar systems in Greenland. Wide, heterogeneous IGZs have already been documented in Antarctica [46, 47, 51, 13]. These wide IGZs may be subjected to high melt rates due to vigorous tidal flushing. In contrast, narrow IGZs may experience limited tidal flushing and, consequently, reduced ice melt, as indicated by other studies [32]. Additionally, seawater may become trapped at low tide [114], limiting heat exchange and further reducing ice melt. To improve our understanding and predictions, it is essential to investigate these physical processes in greater detail.

4.6 Conclusions

Utilizing a time series of satellite observations of ice surface elevation and millimeter-scale vertical motion of ice as it approaches flotation at tidal frequencies, we confirm that the GL of the Lambert-Mellor-Fisher Glacier system migrates over a significantly larger zone than anticipated, i.e., spanning 10 to 15 km rather than a few hundred meters. Through a

Eulerian analysis using surface height change data from ICESat-2, our findings reveal that the IGZ experiences the highest melt rates anywhere on the ice shelf, with averages ranging from 34±12 m/yr on the western side of the system to 101±35 to 173±43 m/yr on the eastern side. These results suggest a need for revisions in the representation of ice melt rates at GLs in numerical ice sheet models. Specifically, we recommend that these models incorporate subshelf melt schemes that account for melting on elements at and upstream of the GL. Such modifications are expected to adjust basal friction in these regions, which could, in turn, increase the glacier's sensitivity to external forcing. Consequently, these revisions are likely to result in higher projections of glacier mass loss and accelerated rates of SLR, potentially by as much as a factor of two. We recommend for further research to explore the physical processes occurring within the IGZ, given its crucial influence on glacier dynamics.

Chapter 5

Conclusions

5.1 Summary of results

The work described in this dissertation aims to enhance the understanding of grounding line (GL) dynamics and their implications for ice mass balance. This is achieved through comprehensive studies on Berry Glacier in West Antarctica and the Amery Ice Shelf in East Antarctica. We aim to document short-term and long-term migrations of GL, and quantify the ice-ocean interactions and mass loss of the glaciers. By examining the interactions between oceanic tides and ice dynamics, particularly focusing on the impacts of Circumpolar Deep Water (CDW) and subglacial processes, we seek to improve projections of future glacier behavior and its contribution to sea level rise (SLR).

Previous studies have often relied on limited temporal data and simplified models that do not account for the short-term variability induced by tidal changes. Most models assume static GL and do not incorporate basal melt in the ice grounding zone (IGZ). These assumptions have led to underestimations of IGZ retreat rates and the associated mass loss.

To overcome these limitations, our research employs a robust dataset comprising ERS-1/2, ALOS-2 PALSAR, Sentinel-1, and COSMO-SkyMed differential synthetic-aperture radar interferometry from 1996 to 2021. DInSAR is used to delineate GL positions by detecting vertical motion with high precision. We also utilize ICESat-2 and data from Operation IceBridge to reconstruct bed topography based on surface height and hydrostatic equilibrium. Furthermore, data from the ICESat-2 mission are employed to compute basal melt rates in the IGZ. The integration of multiple data sources allows for a comprehensive analysis of GL dynamics.

By integrating data from multiple radar sources over 25 years, we achieve a high-resolution temporal analysis of GL behavior. The use of DInSAR allows for accurate mapping of short-term GL variations, revealing a much larger, dynamic and complex IGZ influenced by tidal cycles than previously understood. Our revised bed topography model, based on comprehensive elevation data, uncovers previously undetected subglacial valleys and features. This detailed approach provides a clearer picture of the interactions between oceanic tides, subglacial processes, and ice dynamics. Specifically, our findings on the role of seawater intrusion and complex bed topography in modulating GL retreat provide new insights into the mechanisms driving Antarctic ice mass loss. Additionally, the documented wide IGZs, and heterogeneous and vigorous basal melting challenge the assumptions of static GLs in current physical models, suggesting the need for incorporating dynamic GLs in future models. Collectively, this work advances the understanding of GL dynamics in both Berry Glacier and the Amery Ice Shelf, providing essential data and insights for improving predictive models and addressing the challenges posed by climate change.

5.1.1 Chapter 2 main findings

In chapter 2, we examined the dynamic changes in the IGZ of the Amery Ice Shelf, utilizing a time series of Sentinel-1 DInSAR data from 2018. Our study focused on the Fisher, Mellor, and Lambert glaciers, which collectively drain approximately 47 billion tons of ice annually from East Antarctica. We observed substantial tidal migrations of the IGZ, with variations up to 15 km, which are two orders of magnitude larger than expected for ice flowing over a hard bed. In particular, the Mellor and Lambert estuaries exhibit the widest GZs, attributed to the retrograde bed slopes and the presence of subglacial channels facilitating seawater intrusion. These migrations are not in phase with oceanic tides, indicating complex interactions between the ice and underlying subglacial channels. The analysis identified two distinct migration states that switch intermittently over several weeks, with vertical motion revealing a water column thickness ranging from 2 to 20 cm. This research underscored the importance of incorporating these interactions into physical models, as such intrusions of seawater over wide IGZs can enhance the sensitivity of glaciers to ocean warming, thereby increasing projections of mass loss. We also documented a quasi-exponential relationship between GZ width and bed slopes, highlighting the critical role of glacier geometry in determining the extent of GL migration. This study contributed to a more comprehensive understanding of the complex dynamics within the subglacial environment and their implications for future SLR projections.

5.1.2 Chapter 3 main findings

In chapter 3, we investigated the rapid retreat of the GL of Berry Glacier, West Antarctica, using a comprehensive time series of differential synthetic-aperture radar interferometry data from 1996 to 2021. The GL of Berry Glacier, a major tributary of the Getz Ice Shelf, displayed significant short-term and long-term migrations, with a recorded short-term mi-

gration of 18.0±0.9 km due to oceanic tide variations, necessitating a major revision of the bed topography to reveal a previously unknown subglacial valley 1,300 m deeper than earlier estimations. This migration was not in phase with the tide, instead oscillating between three distinct states governed by spatial variations in bed topography. Our findings indicated that seawater intrusions alternate with extrusions and trapping of seawater. Over the 25-year study period, the GL retreated over 18 km, averaging 0.7 km/year, with concurrent ice thinning by 17±1 m/year and a 64±5% increase in glacier speed, resulting in a total mass loss of 131±23 Gt. The retreat was attributed to enhanced heat flux from warm CDW entering through favorable bathymetric channels on the continental shelf and beneath the ice shelf, coupled with kilometer-sized seawater intrusions beneath the glacier.

5.1.3 Chapter 4 main findings

In chapter 4, we utilized a multi-year dataset to examine the intricate dynamics within the IGZ of Amery Ice Shelf. Our analysis, using a time series of satellite radar interferometry data, confirmed that the GL migrates over a significantly broad zone, spanning 10 to 15 km. The IGZ remained stable between 2018 and 2019. This migration occurs at tidal frequencies, resulting in melt rates within the IGZ that are markedly higher than those further downstream on the ice shelf. Specifically, melt rates within the IGZ range from 31±11 to 255±51 m/yr while the rate is averagely 9 m/yr on the floating ice shelf, indicating that the high speed intrusion significantly contributes to the melting of grounded ice, bringing a vigorous ice-ocean interaction. Our results indicated that the GL migration and associated melt rates have profound implications for glacier dynamics and SLR projections. We recommended revising numerical ice sheet models to incorporate more accurate representations of melt rates and GL processes to improve future SLR predictions. This study underscored the critical need for continued observation and modeling of the IGZ to better understand its impact on the stability of the Antarctic Ice Sheet and global SLR.

5.2 Future outlooks

This work showcases the rapid migration of the GL at different time scales, as well as the complex ice-sea interactions within the IGZ. With the launch of NISAR in 2025, there will be an opportunity to map the GL from DInSAR covering the entire Antarctica. Starting in early 2025, the data from the NASA/Indian Space Research Organization (ISRO) NISAR, which is the first mission dedicated to InSAR, will be available to measure Earth's changing ecosystems, dynamic surfaces, and ice masses with a full coverage of Antarctica every 12 days at the L-band frequency. The platform will include an S-band system which can also be used to GL mapping. NISAR is a mission dedicated to InSAR, with controlled baseline and south looking mode over Antarctica. The L-band frequency will provide higher temporal coherence of the signal than at C- and X-bands. The mission will provide a large increase in data availability beyond S1a/b and CSK. With NISAR, a larger number of DInSAR data per year are expected because the same area will be imaged from several different tracks. Combined with surface height change data from the ICESat-2 mission, basal melt rates in the IGZ around the entire Antarctica also will be calculated to improve the understanding of the ice-sea interactions.

This information will be essential to improve ice sheet models and revise projections because it will affect the representation of IGZ and reduction in buttressing force. At present, ice sheet models assume no melt at the IGZ, no IGZ width, and no seawater intrusion [91]. The same models indicate that the numerical treatment of melt in areas adjacent to the IGZ strongly impacts the sensitivity of the model to ocean thermal forcing. Hence, introducing melt in the IGZ is expected to have a major influence on glacier modeling [91], and in particular will project large mass losses. Adding horizontal coupling of the IGZ response to tides and thickness gradients into the ice sheet model, and adding melt in the IGZ will be exciting work to determine how a modification of the distribution of melt rates in an IGZ impacts glacier evolution, glacier speed, and retreat rates. If these objectives can be

achieved, new insights will be gained into the dynamics of the most important part of an ice sheet for SLR projections, i.e., the IGZ. These new insights will assist numerical models into projecting more realistic SLR and likely higher numbers.

Bibliography

[1] S. Adusumilli, H. A. Fricker, B. Medley, L. Padman, and M. R. Siegfried. Interannual variations in meltwater input to the southern ocean from antarctic ice shelves. *Nature Geoscience*, 13(9):616–620, 2020.

[2] K. E. Alley, T. A. Scambos, M. R. Siegfried, and H. A. Fricker. Impacts of warm water on antarctic ice shelf stability through basal channel formation. *Nature Geoscience*, 9(4):290–293, 2016.

[3] S. Anandakrishnan, D. Voigt, R. Alley, and M. King. Ice stream d flow speed is strongly modulated by the tide beneath the ross ice shelf. *Geophysical Research Letters*, 30(7), 2003.

[4] A. Aschwanden, T. C. Bartholomaus, D. J. Brinkerhoff, and M. Truffer. Brief communication: A roadmap towards credible projections of ice sheet contribution to sea level. *The Cryosphere*, 15(12):5705–5715, 2021.

[5] K. Assmann, E. Darelius, A. K. Wåhlin, T.-W. Kim, and S. H. Lee. Warm circumpolar deep water at the western getz ice shelf front, antarctica. *Geophysical Research Letters*, 46(2):870–878, 2019.

[6] C. B. Begeman, S. M. Tulaczyk, and A. T. Fisher. Spatially variable geothermal heat flux in west antarctica: Evidence and implications. *Geophysical Research Letters*, 44(19):9823–9832, 2017.

[7] R. Bindschadler, H. Choi, A. Wichlacz, R. Bingham, J. Bohlander, K. Brunt, H. Corr, R. Drews, H. Fricker, M. Hall, et al. Getting around antarctica: new high-resolution mappings of the grounded and freely-floating boundaries of the antarctic ice sheet created for the international polar year. *The Cryosphere*, 5(3):569–588, 2011.

[8] V. Brancato, E. Rignot, P. Milillo, M. Morlighem, J. Mouginot, L. An, B. Scheuchl, S. Jeong, P. Rizzoli, J. L. Bueso Bello, et al. Grounding line retreat of denman glacier, east antarctica, measured with cosmo-skymed radar interferometry data. *Geophysical Research Letters*, 47(7):e2019GL086291, 2020.

[9] K. M. Brunt, H. A. Fricker, L. Padman, T. A. Scambos, and S. O'Neel. Mapping the grounding zone of the Ross Ice Shelf, Antarctica, using ICESat laser altimetry. *Annals of Glaciology*, 51(55):71–79, 2010.

[10] C. Burgard, N. C. Jourdain, R. Reese, A. Jenkins, and P. Mathiot. An assessment of basal melt parameterisations for antarctic ice shelves. *The Cryosphere*, 16(12):4931–4975, 2022.

[11] C. Cai, E. Rignot, D. Menemenlis, and Y. Nakayama. Observations and modeling of ocean-induced melt beneath petermann glacier ice shelf in northwestern greenland. *Geophysical Research Letters*, 44(16):8396–8403, 2017.

[12] G. Catania, C. Hulbe, and H. Conway. Grounding-line basal melt rates determined using radar-derived internal stratigraphy. *Journal of Glaciology*, 56(197):545–554, 2010.

[13] H. Chen, E. Rignot, B. Scheuchl, and S. Ehrenfeucht. Grounding zone of amery ice shelf, antarctica, from differential synthetic-aperture radar interferometry. *Geophysical Research Letters*, 50(6):e2022GL102430, 2023.

[14] E. Ciracì, E. Rignot, B. Scheuchl, V. Tolpekin, M. Wollersheim, L. An, P. Milillo, J.-L. Bueso-Bello, P. Rizzoli, and L. Dini. Melt rates in the kilometer-size grounding zone of petermann glacier, greenland, before and during a retreat. *Proceedings of the National Academy of Sciences*, 120(20):e2220924120, 2023.

[15] J. R. Cochran, K. J. Tinto, and R. E. Bell. Detailed bathymetry of the continental shelf beneath the getz ice shelf, west antarctica. *Journal of Geophysical Research: Earth Surface*, 125(10):e2019JF005493, 2020.

[16] S. J. Cook, P. Christoffersen, J. Todd, D. Slater, and N. Chauché. Coupled modelling of subglacial hydrology and calving-front melting at store glacier, west greenland. *The Cryosphere*, 14(3):905–924, 2020.

[17] R. M. DeConto, D. Pollard, R. B. Alley, I. Velicogna, E. Gasson, N. Gomez, S. Sadai, A. Condron, D. M. Gilford, E. L. Ashe, et al. The paris climate agreement and future sea-level rise from antarctica. *Nature*, 593(7857):83–89, 2021.

[18] B. Dorschel, L. Hehemann, S. Viquerat, F. Warnke, S. Dreutter, Y. Schulze Tenberge, D. Accettella, L. An, F. Barrios, E. A. Bazhenova, J. Black, F. Bohoyo, C. Davey, L. de Santis, C. Escutia Dotti, A. C. Fremand, P. T. Fretwell, J. A. Gales, J. Gao, L. Gasperini, J. S. Greenbaum, J. Henderson Jencks, K. A. Hogan, J. K. Hong, M. Jakobsson, L. Jensen, J. Kool, S. Larin, R. D. Larter, G. L. Leitchenkov, B. Loubrieu, K. Mackay, L. Mayer, R. Millan, M. Morlighem, F. Navidad, F.-O. Nitsche, Y. Nogi, C. Pertuisot, A. L. Post, H. D. Pritchard, A. Purser, M. Rebesco, E. Rignot, J. L. Roberts, M. Rovere, I. Ryzhov, C. Sauli, T. Schmitt, A. Silvano, J. E. Smith, H. Snaith, A. J. Tate, K. Tinto, P. Vandenbossche, P. Weatherall, P. Wintersteller, C. Yang, T. Zhang, and J. E. Arndt. The International Bathymetric Chart of the Southern Ocean Version 2 (IBCSO v2), 2022.

[19] C. Dow, N. Ross, H. Jeofry, K. Siu, and M. Siegert. Antarctic basal environment shaped by high-pressure flow through a subglacial river system. *Nature Geoscience*, 15(11):892–898, 2022.

[20] L. Favier, G. Durand, S. L. Cornford, G. H. Gudmundsson, O. Gagliardini, F. Gillet-Chaulet, T. Zwinger, A. Payne, and A. M. Le Brocq. Retreat of pine island glacier controlled by marine ice-sheet instability. *Nature Climate Change*, 4(2):117–121, 2014.

[21] B. I. Freer, O. Marsh, A. E. Hogg, H. A. Fricker, and L. Padman. Modes of antarctic tidal grounding line migration revealed by ice, cloud, and land elevation satellite-2 (icesat-2) laser altimetry. *The Cryosphere*, 17(9):4079–4101, 2023.

[22] H. A. Fricker, I. Allison, M. Craven, G. Hyland, A. Ruddell, N. Young, R. Coleman, M. King, K. Krebs, and S. Popov. Redefinition of the amery ice shelf, east antarctica, grounding zone. *Journal of Geophysical Research: Solid Earth*, 107(B5):ECV–1, 2002.

[23] H. A. Fricker, R. Coleman, L. Padman, T. A. Scambos, J. Bohlander, and K. M. Brunt. Mapping the grounding zone of the amery ice shelf, east antarctica using insar, modis and icesat. *Antarctic Science*, 21(5):515–532, 2009.

[24] H. A. Fricker, T. Scambos, R. Bindschadler, and L. Padman. An active subglacial water system in west antarctica mapped from space. *Science*, 315(5818):1544–1548, 2007.

[25] R. Gadi, E. Rignot, and D. Menemenlis. Modeling ice melt rates from seawater intrusions in the grounding zone of petermann gletscher, greenland. *Geophysical Research Letters*, 50(24):e2023GL105869, 2023.

[26] B. Galton-Fenzi, J. Hunter, R. Coleman, S. Marsland, and R. Warner. Modeling the basal melting and marine ice accretion of the amery ice shelf. *Journal of Geophysical Research: Oceans*, 117(C9), 2012.

[27] Q. Glaude, C. Amory, S. Berger, D. Derauw, F. Pattyn, C. Barbier, and A. Orban. Empirical removal of tides and inverse barometer effect on dinsar from double dinsar and a regional climate model. *IEEE Journal of Selected Topics in Applied Earth Observations and Remote Sensing*, 13:4085–4094, 2020.

[28] D. Goldberg, N. Gourmelen, S. Kimura, R. Millan, and K. Snow. How accurately should we model ice shelf melt rates? *Geophysical Research Letters*, 46(1):189–199, 2019.

[29] N. R. Golledge, Z. A. Thomas, R. H. Levy, E. G. Gasson, T. R. Naish, R. M. McKay, D. E. Kowalewski, and C. J. Fogwill. Antarctic climate and ice-sheet configuration during the early pliocene interglacial at 4.23 ma. *Climate of the Past*, 13(7):959–975, 2017.

[30] D. E. Gwyther, C. F. Dow, S. Jendersie, N. Gourmelen, and B. K. Galton-Fenzi. Subglacial freshwater drainage increases simulated basal melt of the totten ice shelf. *Geophysical Research Letters*, 50(12):e2023GL103765, 2023.

[31] H. Hersbach, B. Bell, P. Berrisford, S. Hirahara, A. Horányi, J. Muñoz-Sabater, J. Nicolas, C. Peubey, R. Radu, D. Schepers, et al. The ERA5 global reanalysis. *Quarterly Journal of the Royal Meteorological Society*, 146(730):1999–2049, 2020.

[32] P. R. Holland, H. F. Corr, D. G. Vaughan, A. Jenkins, and P. Skvarca. Marine ice in larsen ice shelf. *Geophysical Research Letters*, 36(11), 2009.

[33] R. H. Jackson, R. J. Motyka, J. M. Amundson, N. Abib, D. A. Sutherland, J. D. Nash, and C. Kienholz. The relationship between submarine melt and subglacial discharge from observations at a tidewater glacier. *Journal of Geophysical Research: Oceans*, 127(10):e2021JC018204, 2022.

[34] S. Jacobs, C. Giulivi, P. Dutrieux, E. Rignot, F. Nitsche, and J. Mouginot. Getz ice shelf melting response to changes in ocean forcing. *Journal of Geophysical Research: Oceans*, 118(9):4152–4168, 2013.

[35] S. S. Jacobs, A. Jenkins, C. F. Giulivi, and P. Dutrieux. Stronger ocean circulation and increased melting under pine island glacier ice shelf. *Nature Geoscience*, 4(8):519–523, 2011.

[36] A. Jenkins. Convection-driven melting near the grounding lines of ice shelves and tidewater glaciers. *Journal of Physical Oceanography*, 41(12):2279–2294, 2011.

[37] A. Jenkins, D. Shoosmith, P. Dutrieux, S. Jacobs, T. W. Kim, S. H. Lee, H. K. Ha, and S. Stammerjohn. West antarctic ice sheet retreat in the amundsen sea driven by decadal oceanic variability. *Nature Geoscience*, 11(10):733–738, 2018.

[38] I. Joughin, R. B. Alley, and D. M. Holland. Ice-sheet response to oceanic forcing. *Science*, 338(6111):1172–1176, 2012.

[39] S. Koellner, B. R. Parizek, R. B. Alley, A. Muto, and N. Holschuh. The impact of spatially-variable basal properties on outlet glacier flow. *Earth and Planetary Science Letters*, 515:200–208, 2019.

[40] E. Larour, H. Seroussi, M. Morlighem, and E. Rignot. Continental scale, high order, high spatial resolution, ice sheet modeling using the ice sheet system model (issm). *Journal of Geophysical Research: Earth Surface*, 117(F1), 2012.

[41] A. M. Le Brocq, N. Ross, J. A. Griggs, R. G. Bingham, H. F. Corr, F. Ferraccioli, A. Jenkins, T. A. Jordan, A. J. Payne, D. M. Rippin, et al. Evidence from ice shelves for channelized meltwater flow beneath the Antarctic Ice Sheet. *Nature Geoscience*, 6(11):945–948, 2013.

[42] C. Leuschen. IceBridge MCoRDS L1B Geolocated Radar Echo Strength Profiles, Version 1, 2011.

[43] J. A. MacGregor, L. N. Boisvert, B. Medley, A. A. Petty, J. P. Harbeck, R. E. Bell, J. B. Blair, E. Blanchard-Wrigglesworth, E. M. Buckley, M. S. Christoffersen, et al. The scientific legacy of nasa's operation icebridge, 2021.

[44] R. Massom and D. Lubin. *Polar remote sensing*, volume 2. Springer, 2006.

[45] R. Michel and E. Rignot. Flow of glaciar moreno, argentina, from repeat-pass shuttle imaging radar images: comparison of the phase correlation method with radar interferometry. *Journal of Glaciology*, 45(149):93–100, 1999.

[46] P. Milillo, E. Rignot, J. Mouginot, B. Scheuchl, M. Morlighem, X. Li, and J. T. Salzer. On the short-term grounding zone dynamics of pine island glacier, west antarctica, observed with cosmo-skymed interferometric data. *Geophysical Research Letters*, 44(20):10–436, 2017.

[47] P. Milillo, E. Rignot, P. Rizzoli, B. Scheuchl, J. Mouginot, J. Bueso-Bello, and P. Prats-Iraola. Heterogeneous retreat and ice melt of thwaites glacier, west antarctica. *Science Advances*, 5(1):eaau3433, 2019.

[48] P. Milillo, E. Rignot, P. Rizzoli, B. Scheuchl, J. Mouginot, J. L. Bueso-Bello, P. Prats-Iraola, and L. Dini. Rapid glacier retreat rates observed in west antarctica. *Nature Geoscience*, 15(1):48–53, 2022.

[49] R. Millan, P. St-Laurent, E. Rignot, M. Morlighem, J. Mouginot, and B. Scheuchl. Constraining an ocean model under getz ice shelf, antarctica, using a gravity-derived bathymetry. *Geophysical Research Letters*, 47(13):e2019GL086522, 2020.

[50] T. Millgate, P. R. Holland, A. Jenkins, and H. L. Johnson. The effect of basal channels on oceanic ice-shelf melting. *Journal of Geophysical Research: Oceans*, 118(12):6951–6964, 2013.

[51] Y. Mohajerani, S. Jeong, B. Scheuchl, I. Velicogna, E. Rignot, and P. Milillo. Automatic delineation of glacier grounding lines in differential interferometric synthetic-aperture radar data using deep learning. *Scientific Reports*, 11(1):4992, 2021.

[52] M. Morlighem. MEaSUREs BedMachine Antarctica, Version 3, 2022.

[53] M. Morlighem, E. Rignot, T. Binder, D. Blankenship, R. Drews, G. Eagles, O. Eisen, F. Ferraccioli, R. Forsberg, P. Fretwell, et al. Deep glacial troughs and stabilizing ridges unveiled beneath the margins of the Antarctic Ice Sheet. *Nature Geoscience*, 13(2):132–137, 2020.

[54] J. Mouginot, E. Rignot, B. Scheuchl, and R. Millan. Comprehensive annual ice sheet velocity mapping using landsat-8, sentinel-1, and radarsat-2 data. *Remote Sensing*, 9(4):364, 2017.

[55] J. Mouginot, B. Scheuchl, and E. Rignot. Mapping of ice motion in antarctica using synthetic-aperture radar data. *Remote Sensing*, 4(9):2753–2767, 2012.

[56] J. Mouginot, B. Scheuchl, and E. Rignot. MEaSUREs Annual Antarctic Ice Velocity Maps, Version 1, 2017.

[57] Y. Nakayama, C. Cai, and H. Seroussi. Impact of subglacial freshwater discharge on pine island ice shelf. *Geophysical Research Letters*, 48(18):e2021GL093923, 2021.

[58] J. Nilsson, A. Gardner, and F. Paolo. MEaSUREs ITS_LIVE Antarctic Grounded Ice Sheet Elevation Change, Version 1, 2023.

[59] J. Paden, J. Li, C. Leuschen, F. Rodriguez-Morales, and R. D. Hale. IceBridge MCoRDS L2 Ice Thickness, Version 1, 2010.

[60] J. Paden, J. Li, C. Leuschen, F. Rodriguez-Morales, and R. D. Hale. IceBridge MCoRDS L1B Geolocated Radar Echo Strength Profiles, Version 2, 2014.

[61] L. Padman, S. Y. Erofeeva, and H. A. Fricker. Improving Antarctic tide models by assimilation of ICESat laser altimetry over ice shelves. *Geophysical Research Letters*, 35(22), 2008.

[62] L. Padman, M. King, D. Goring, H. Corr, and R. Coleman. Ice-shelf elevation changes due to atmospheric pressure variations. *Journal of Glaciology*, 49(167):521–526, 2003.

[63] F. S. Paolo, H. A. Fricker, and L. Padman. Volume loss from antarctic ice shelves is accelerating. *Science*, 348(6232):327–331, 2015.

[64] B. Parizek, K. Christianson, S. Anandakrishnan, R. Alley, R. Walker, R. Edwards, D. Wolfe, G. Bertini, S. Rinehart, R. Bindschadler, et al. Dynamic (in) stability of thwaites glacier, west antarctica. *Journal of Geophysical Research: Earth Surface*, 118(2):638–655, 2013.

[65] F. Pattyn, A. Huyghe, S. De Brabander, and B. De Smedt. Role of transition zones in marine ice sheet dynamics. *Journal of Geophysical Research: Earth Surface*, 111(F2), 2006.

[66] T. Pelle, M. Morlighem, and J. H. Bondzio. Brief communication: Picop, a new ocean melt parameterization under ice shelves combining pico and a plume model. *The Cryosphere*, 13(3):1043–1049, 2019.

[67] H.-O. Pörtner, D. C. Roberts, V. Masson-Delmotte, P. Zhai, M. Tignor, E. Poloczanska, N. Weyer, et al. The ocean and cryosphere in a changing climate. *IPCC special report on the ocean and cryosphere in a changing climate*, 1155, 2019.

[68] P. Potin, B. Rosich, P. Grimont, N. Miranda, I. Shurmer, A. O'Connell, R. Torres, and M. Krassenburg. Sentinel-1 mission status, 2016. Proceedings of EUSAR 2016: 11th European Conference on Synthetic Aperture Radar, VDE, 6–9 June 2016.

[69] H. Pritchard, S. R. Ligtenberg, H. A. Fricker, D. G. Vaughan, M. R. van den Broeke, and L. Padman. Antarctic ice-sheet loss driven by basal melting of ice shelves. *Nature*, 484(7395):502–505, 2012.

[70] H. D. Pritchard, R. J. Arthern, D. G. Vaughan, and L. A. Edwards. Extensive dynamic thinning on the margins of the greenland and antarctic ice sheets. *Nature*, 461(7266):971–975, 2009.

[71] E. Rignot. Tidal motion, ice velocity and melt rate of petermann gletscher, greenland, measured from radar interferometry. *Journal of Glaciology*, 42(142):476–485, 1996.

[72] E. Rignot. Mass balance of East Antarctic glaciers and ice shelves from satellite data. *Annals of Glaciology*, 34:217–227, 2002.

[73] E. Rignot, J. L. Bamber, M. R. Van Den Broeke, C. Davis, Y. Li, W. J. Van De Berg, and E. Van Meijgaard. Recent antarctic ice mass loss from radar interferometry and regional climate modelling. *Nature Geoscience*, 1(2):106–110, 2008.

[74] E. Rignot, S. Jacobs, J. Mouginot, and B. Scheuchl. Ice-shelf melting around antarctica. *Science*, 341(6143):266–270, 2013.

[75] E. Rignot and S. S. Jacobs. Rapid bottom melting widespread near antarctic ice sheet grounding lines. *Science*, 296(5575):2020–2023, 2002.

[76] E. Rignot, J. Mouginot, M. Morlighem, H. Seroussi, and B. Scheuchl. Widespread, rapid grounding line retreat of pine island, thwaites, smith, and kohler glaciers, west antarctica, from 1992 to 2011. *Geophysical Research Letters*, 41(10):3502–3509, 2014.

[77] E. Rignot, J. Mouginot, and B. Scheuchl. Antarctic grounding line mapping from differential satellite radar interferometry. *Geophysical Research Letters*, 38(10), 2011.

[78] E. Rignot, J. Mouginot, and B. Scheuchl. Ice flow of the Antarctic Ice Sheet. *Science*, 333(6048):1427–1430, 2011.

[79] E. Rignot, J. Mouginot, B. Scheuchl, M. Van Den Broeke, M. J. Van Wessem, and M. Morlighem. Four decades of Antarctic Ice Sheet mass balance from 1979–2017. *Proceedings of the National Academy of Sciences*, 116(4):1095–1103, 2019.

[80] E. Rignot, D. G. Vaughan, M. Schmeltz, T. Dupont, and D. MacAyeal. Acceleration of Pine island and Thwaites glaciers, West Antarctica. *Annals of Glaciology*, 34:189–194, 2002.

[81] A. A. Robel, E. Wilson, and H. Seroussi. Layered seawater intrusion and melt under grounded ice. *The Cryosphere*, 16(2):451–469, 2022.

[82] S. H. Rosier and G. H. Gudmundsson. Tidal bending of ice shelves as a mechanism for large-scale temporal variations in ice flow. *The Cryosphere*, 12(5):1699–1713, 2018.

[83] R. Sayag and M. G. Worster. Elastic dynamics and tidal migration of grounding lines modify subglacial lubrication and melting. *Geophysical Research Letters*, 40(22):5877–5881, 2013.

[84] T. A. Scambos, R. E. Bell, R. B. Alley, S. Anandakrishnan, D. Bromwich, K. Brunt, K. Christianson, T. Creyts, S. Das, R. DeConto, et al. How much, how fast?: A science review and outlook for research on the instability of antarctica's thwaites glacier in the 21st century. *Global and Planetary Change*, 153:16–34, 2017.

[85] B. Scheuchl, J. Mouginot, E. Rignot, M. Morlighem, and A. Khazendar. Grounding line retreat of Pope, Smith, and Kohler Glaciers, West Antarctica, measured with Sentinel-1a radar interferometry data. *Geophysical Research Letters*, 43(16):8572–8579, 2016.

[86] S. Schmidtko, K. J. Heywood, A. F. Thompson, and S. Aoki. Multidecadal warming of antarctic waters. *Science*, 346(6214):1227–1231, 2014.

[87] C. Schoof. Ice sheet grounding line dynamics: Steady states, stability, and hysteresis. *Journal of Geophysical Research: Earth Surface*, 112(F3), 2007.

[88] A. Schubert, D. Small, N. Miranda, D. Geudtner, and E. Meier. Sentinel-1A product geolocation accuracy: Commissioning phase results. *Remote Sensing*, 7(7):9431–9449, 2015.

[89] H. L. Selley, A. E. Hogg, S. Cornford, P. Dutrieux, A. Shepherd, J. Wuite, D. Floricioiu, A. Kusk, T. Nagler, L. Gilbert, et al. Widespread increase in dynamic imbalance in the getz region of antarctica from 1994 to 2018. *Nature Communications*, 12(1):1133, 2021.

[90] O. Sergienko, D. Goldberg, and C. Little. Alternative ice shelf equilibria determined by ocean environment. *Journal of Geophysical Research: Earth Surface*, 118(2):970–981, 2013.

[91] H. Seroussi and M. Morlighem. Representation of basal melting at the grounding line in ice flow models. *The Cryosphere*, 12(10):3085–3096, 2018.

[92] H. Seroussi, Y. Nakayama, E. Larour, D. Menemenlis, M. Morlighem, E. Rignot, and A. Khazendar. Continued retreat of thwaites glacier, west antarctica, controlled by bed topography and ocean circulation. *Geophysical Research Letters*, 44(12):6191–6199, 2017.

[93] H. Seroussi, S. Nowicki, A. J. Payne, H. Goelzer, W. H. Lipscomb, A. Abe-Ouchi, C. Agosta, T. Albrecht, X. Asay-Davis, A. Barthel, et al. ISMIP6 Antarctica: a multi-model ensemble of the Antarctic ice sheet evolution over the 21st century. *The Cryosphere*, 14(9):3033–3070, 2020.

[94] D. E. Shean, I. R. Joughin, P. Dutrieux, B. E. Smith, and E. Berthier. Ice shelf basal melt rates from a high-resolution digital elevation model (dem) record for pine island glacier, antarctica. *The Cryosphere*, 13(10):2633–2656, 2019.

[95] A. Shepherd, L. Gilbert, A. S. Muir, H. Konrad, M. McMillan, T. Slater, K. H. Briggs, A. V. Sundal, A. E. Hogg, and M. E. Engdahl. Trends in antarctic ice sheet elevation and mass. *Geophysical Research Letters*, 46(14):8174–8183, 2019.

[96] A. Shepherd, E. R. Ivins, V. R. Barletta, M. J. Bentley, S. Bettadpur, K. H. Briggs, D. H. Bromwich, R. Forsberg, N. Galin, M. Horwath, et al. A reconciled estimate of ice-sheet mass balance. *Science*, 338(6111):1183–1189, 2012.

[97] M. Siegert, R. B. Alley, E. Rignot, J. Englander, and R. Corell. Twenty-first century sea-level rise could exceed ipcc projections for strong-warming futures. *One Earth*, 3(6):691–703, 2020.

[98] A. Silvano, S. R. Rintoul, B. Peña-Molino, W. R. Hobbs, E. van Wijk, S. Aoki, T. Tamura, and G. D. Williams. Freshening by glacial meltwater enhances melting of ice shelves and reduces formation of antarctic bottom water. *Science Advances*, 4(4):eaap9467, 2018.

[99] D. A. Slater, D. Felikson, F. Straneo, H. Goelzer, C. M. Little, M. Morlighem, X. Fettweis, and S. Nowicki. Twenty-first century ocean forcing of the greenland ice sheet for modelling of sea level contribution. *The Cryosphere*, 14(3):985–1008, 2020.

[100] D. A. Slater, P. Nienow, D. Goldberg, T. Cowton, and A. Sole. A model for tidewater glacier undercutting by submarine melting. *Geophysical Research Letters*, 44(5):2360–2368, 2017.

[101] B. E. Smith, T. C. Sutterley, S. Dickinson, B. P. Jelley, D. Felikson, T. Neumann, H. A. Fricker, A. Gardner, L. Padman, T. Markus, N. Kurtz, S. Bhardwaj, D. Hancock, and J. Lee. ATLAS/ICESat-2 L3B Gridded Antarctic and Arctic Land Ice Height Change, Version 3, 2023.

[102] B. E. Smith, T. C. Sutterley, S. Dickinson, B. P. Jelley, D. Felikson, T. Neumann, H. A. Fricker, A. Gardner, L. Padman, T. Markus, N. Kurtz, S. Bhardwaj, D. Hancock, and J. Lee. ATLAS/ICESat-2 L3B Gridded Antarctic and Arctic Land Ice Height, Version 3, 2023.

[103] M. Studinger. IceBridge ATM L1B Elevation and Return Strength, Version 2, 2013.

[104] M. Studinger. IceBridge ATM L2 Icessn Elevation, Slope, and Roughness, Version 2, 2014.

[105] S. Sun, F. Pattyn, E. G. Simon, T. Albrecht, S. Cornford, R. Calov, C. Dumas, F. Gillet-Chaulet, H. Goelzer, N. R. Golledge, et al. Antarctic ice sheet response to sudden and sustained ice-shelf collapse (abumip). *Journal of Glaciology*, 66(260):891–904, 2020.

[106] The IMBIE team. Mass balance of the antarctic ice sheet from 1992 to 2017. *Nature*, 558(7709):219–222, 2018.

[107] R. H. Thomas and C. R. Bentley. A model for holocene retreat of the west antarctic ice sheet. *Quaternary Research*, 10(2):150–170, 1978.

[108] V. C. Tsai and G. H. Gudmundsson. An improved model for tidally modulated grounding-line migration. *Journal of Glaciology*, 61(226):216–222, 2015.

[109] V. C. Tsai and J. R. Rice. Modeling turbulent hydraulic fracture near a free surface. *Journal of Applied Mechanics*, 2012.

[110] J. M. Van Wessem, W. J. Van De Berg, B. P. Noël, E. Van Meijgaard, C. Amory, G. Birnbaum, C. L. Jakobs, K. Krüger, J. T. Lenaerts, S. Lhermitte, et al. Modelling the climate and surface mass balance of polar ice sheets using racmo2–part 2: Antarctica (1979–2016). *The Cryosphere*, 12(4):1479–1498, 2018.

[111] D. G. Vaughan, H. F. Corr, R. A. Bindschadler, P. Dutrieux, G. H. Gudmundsson, A. Jenkins, T. Newman, P. Vornberger, and D. J. Wingham. Subglacial melt channels and fracture in the floating part of pine island glacier, antarctica. *Journal of Geophysical Research: Earth Surface*, 117(F3), 2012.

[112] I. Velicogna, T. C. Sutterley, and M. R. Van Den Broeke. Regional acceleration in ice mass loss from greenland and antarctica using grace time-variable gravity data. *Geophysical Research Letters*, 41(22):8130–8137, 2014.

[113] R. T. Walker, B. R. Parizek, R. B. Alley, S. Anandakrishnan, K. L. Riverman, and K. Christianson. Ice-shelf tidal flexure and subglacial pressure variations. *Earth and Planetary Science Letters*, 361:422–428, 2013.

[114] K. Warburton, D. Hewitt, and J. Neufeld. Tidal grounding-line migration modulated by subglacial hydrology. *Geophysical Research Letters*, 47(17):e2020GL089088, 2020.

[115] J. D. Wille, V. Favier, I. V. Gorodetskaya, C. Agosta, C. Kittel, J. C. Beeman, N. C. Jourdain, J. T. Lenaerts, and F. Codron. Antarctic atmospheric river climatology and precipitation impacts. *Journal of Geophysical Research: Atmospheres*, 126(8):e2020JD033788, 2021.

[116] E. A. Wilson, A. J. Wells, I. J. Hewitt, and C. Cenedese. The dynamics of a subglacial salt wedge. *Journal of Fluid Mechanics*, 895:A20, 2020.

[117] N. Wilson, F. Straneo, and P. Heimbach. Satellite-derived submarine melt rates and mass balance (2011–2015) for greenland's largest remaining ice tongues. *The Cryosphere*, 11(6):2773–2782, 2017.

Appendix A

Supplemental Information: Rapid retreat of Berry Glacier, West Antarctica, from satellite radar interferometry and other data

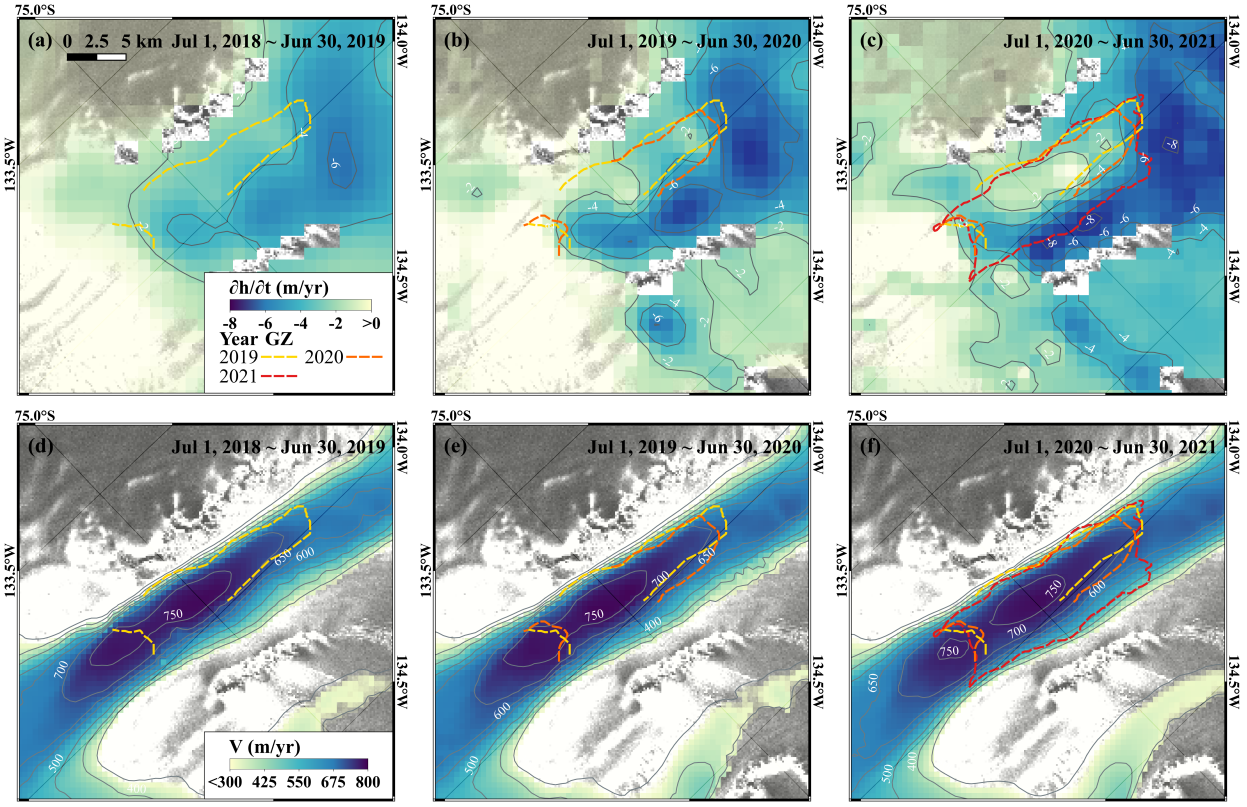


Figure A.1: **Annually height-change rate, $\partial h/\partial t$, and flow speed, V, of Berry Glacier.** $\partial h/\partial t$ (a-c) and V (d-f) in year 2019, 2020 and 2021 with IGZ boundaries for year 2019 (yellow), 2020 (orange), and 2021 (red).

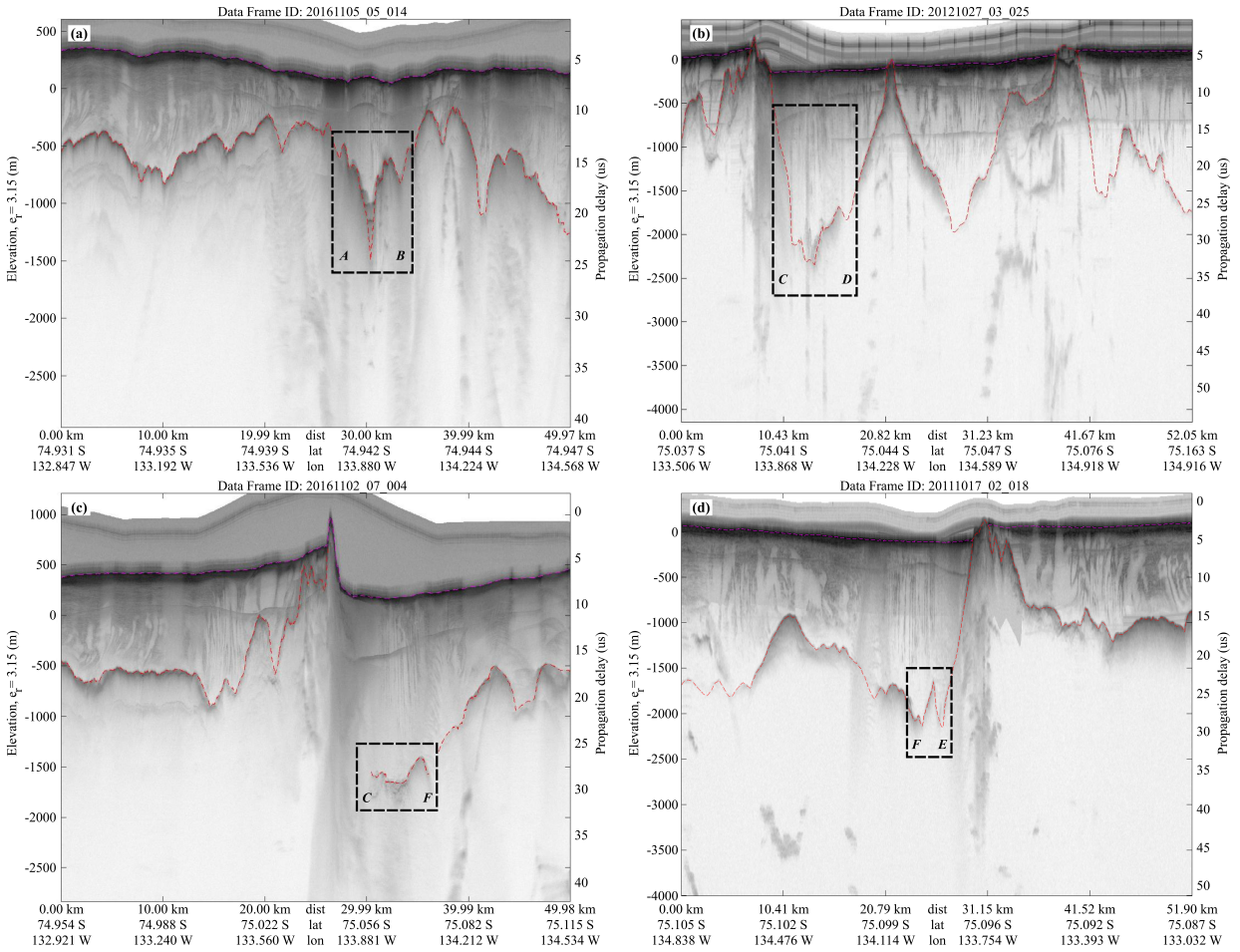


Figure A.2: **Echo strength profiles along OIB tracks.** Echo strength from Multichannel Coherent Radar Depth Sounder (MCoRDS) along profiles A-B (a), C-D (b), C-F (c) and F-E (d). Purple dash lines mark picked ice surface, h, and red dash lines represent picked ice bottoms. Black box contains the same spatial extent as in Fig. A.3. The direction of the profile in (d) is opposite to that of the profile in Fig. A.3d because the starting point of the frame of echo strength profile in (d) is in the west instead of the east.

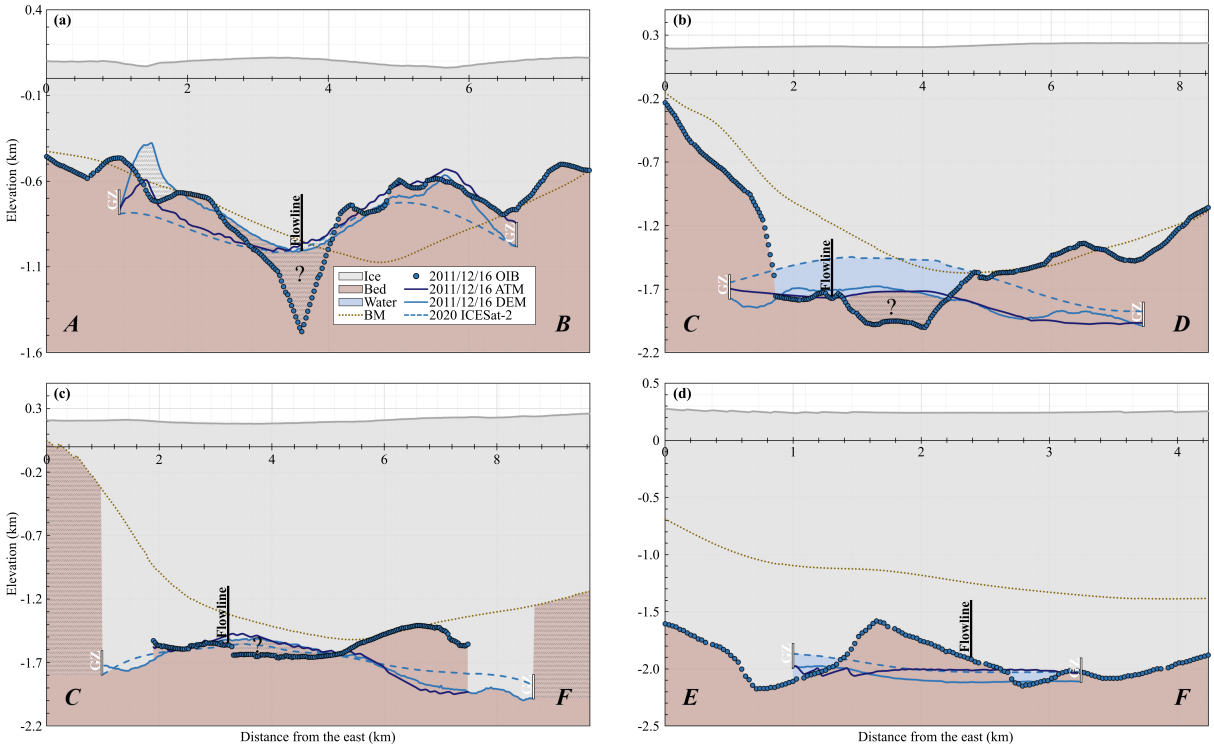


Figure A.3: **Profiles of ice surface, h, ice draft and bed topography, b, along OIB tracks.** h, ice bottom and b along profiles A-B (a), C-D (b), C-F (c) and E-F (d). h (grey line) from Airborne Topographic Mapper (ATM), ice draft (blue line) deduced from DEMs in the same year of OIB, and b (brown dotted line) from BMv3.7. Blue dash line marks flotation from ICESat-2 on Jan 1, 2020; blue solid lines are ice bottom deduced from DEMs computed from ICESat-2; dark blue line is ice bottom deduced from ATM; blue dots are ice bottoms from OIB. Bed layers marked with question marks are due to questionable picked ice bottoms based on echo strength profiles (Fig. A.2). Acquisition times of OIB are respectively from Nov 5, 2016 (a), Oct 27, 2012 (b), Nov 2, 2016 (c) and Oct 17, 2011 (d).

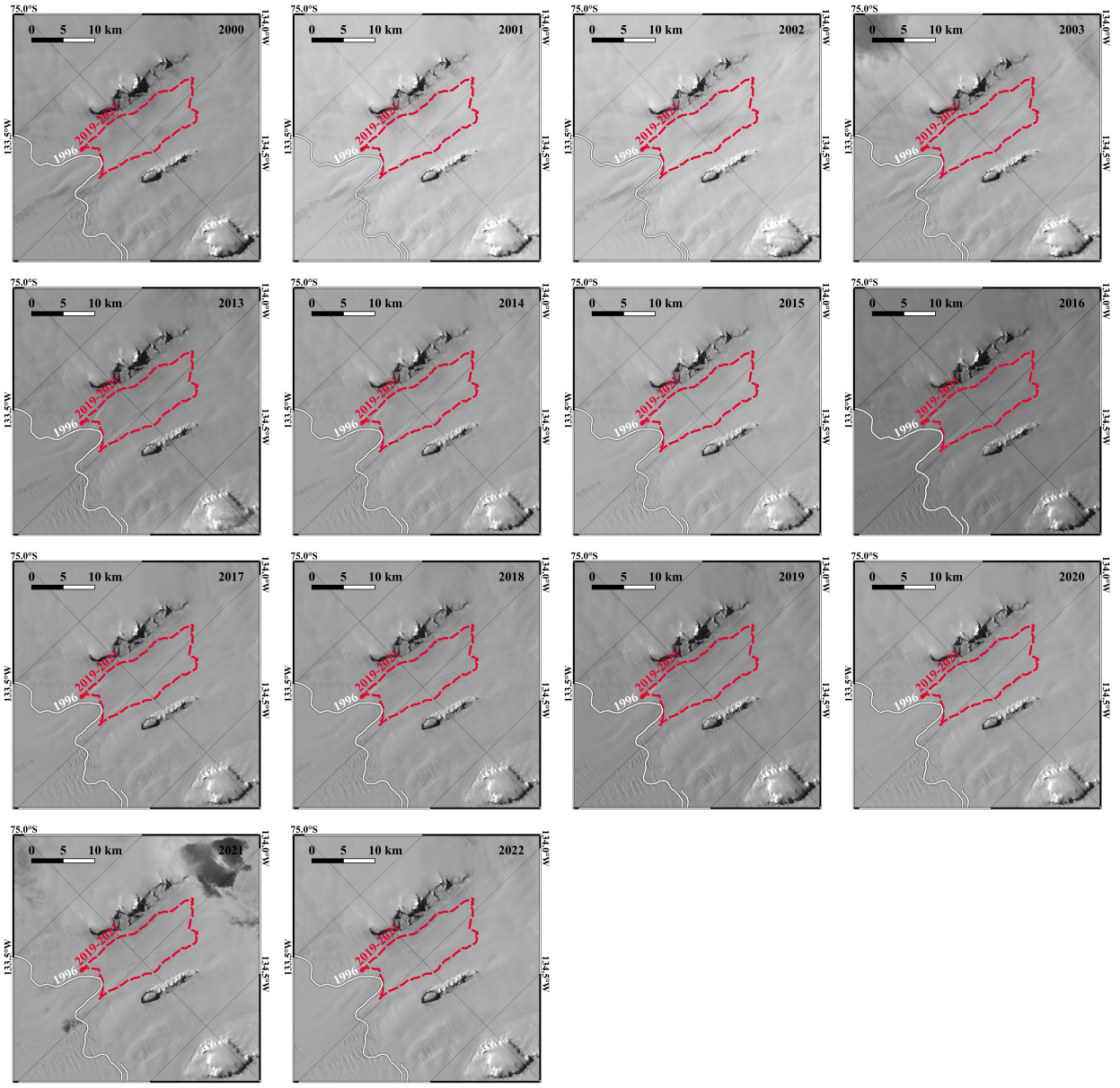


Figure A.4: **Disappeared surface bumps in IGZ.** A time series of Landsat 7/8 panchromatic band images with 1996 GL and 2019-2021 IGZ covering Berry Glacier, West Antarctica from 2000-2022 (gaps in 2004-2012).

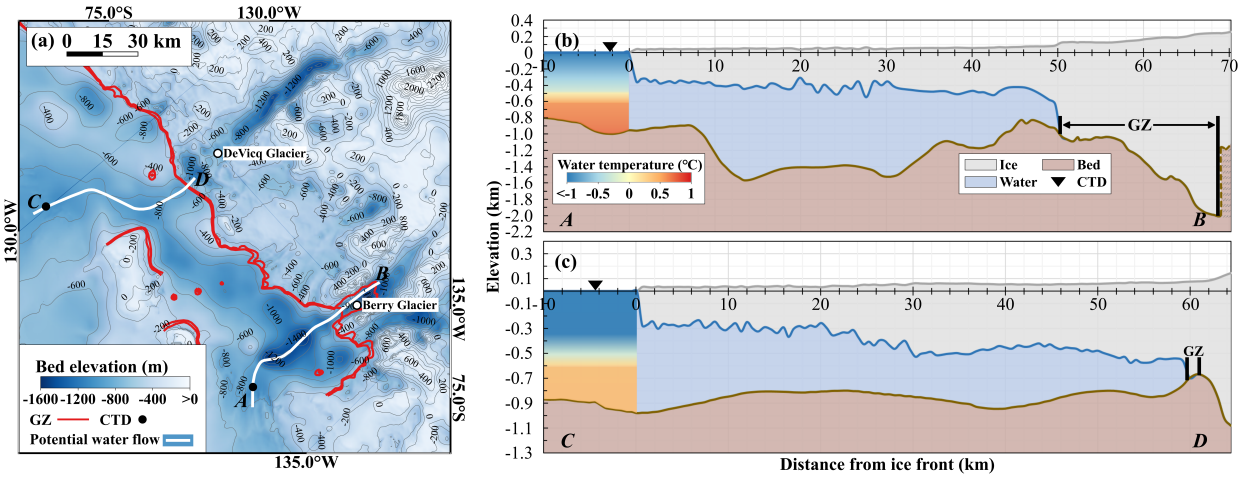


Figure A.5: **Bed topography, *b*, in the west Getz Ice Shelf.** (a) *b* in the west Getz Ice Shelf from BMv3.7 color coded from -1600 m (blue) to 0 m (white), with IGZ (red), CTD at ice front (black dots) and 200-m contours, showing the potential water path (white arrow) from the ice front to the IGZ of Berry and DeVicq; surface elevation, ice bottom and *b* from BMv3.7 along profiles A-B (b) and C-D (c) in (a). The ocean in front of the ice shelf front is color-coded with the water temperature from 2007 CTD [34].

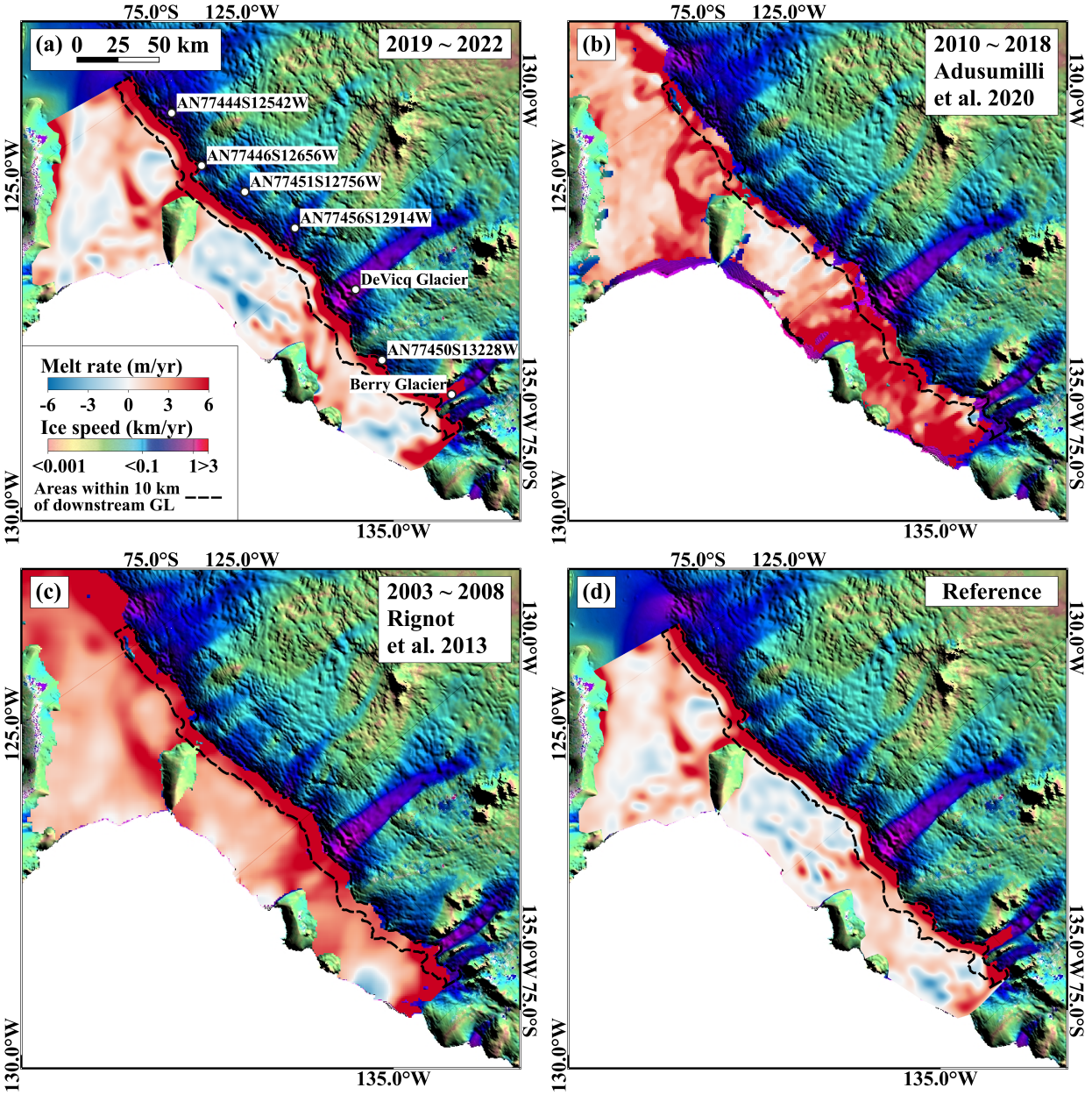


Figure A.6: **Basal melt rate, $\dot{b}$, on the west Getz Ice Shelf.** $\dot{b}$ over 2019-2022 (a), 2010-2018 from Adusumilli et al. 2020 [1] (b), and 2003-2008 from Rignot et al. 2013 [74] (c) overlaid on ice speed map with the names of ice flow; (d) reference of $\dot{b}$ calculated with $SMB_{1979-2004}$ and ice velocity in 2008 assuming $\partial h/\partial t = 0$. Black dash lines mark the areas within 10 km of downstream GL. The average $\dot{b}$ (m/yr) within the 10-km regions for each ice flows is shown in the following table.

Places	2019-2022	2010-2018	2003-2008	Reference
The entire 10-km regions	5.9	5.8	7.0	5.1
Berry Glacier	14.9	Null	9.1	11.8
AN77450S13228W	6.8	9.2	4.2	4.5
DeVicq Glacier	8.6	7.7	6.9	5.4
AN77456S12914W	6.0	5.6	6.1	5.1
AN77451S12756W	5.3	4.9	4.7	5.3
AN77446S12656W	7.4	6.7	6.4	5.4
AN77444S12542W	6.9	4.3	7.8	6.3

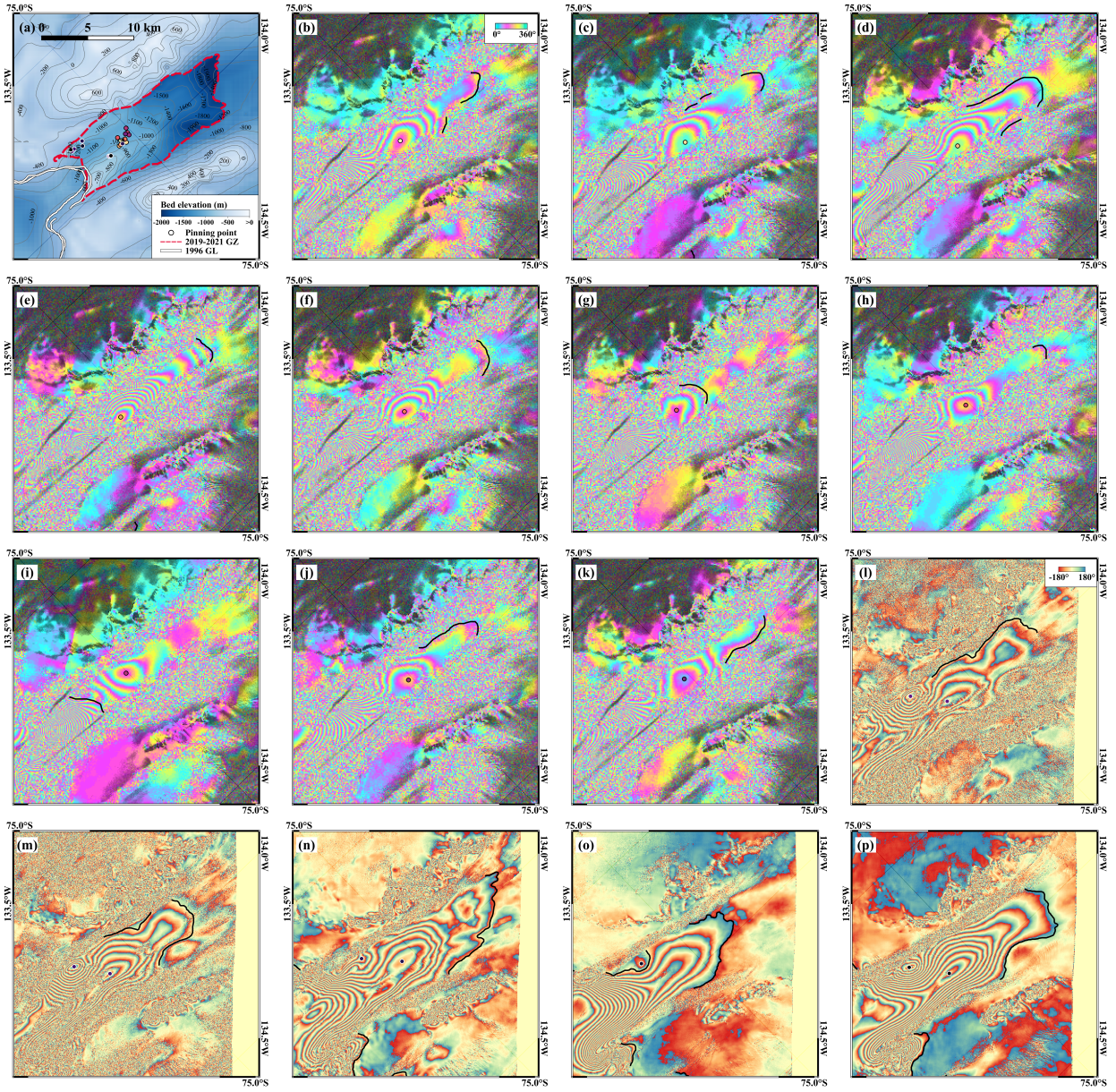


Figure A.7: **Pinning points in IGZ.** (a) Dots mark pinning points based on double-difference interferograms (b-p) in 2019-2021 IGZ overlaid on bed topography combining BMv3.7 (outside IGZ) and ice base from flotation using a WorldView DEM (inside IGZ) color coded from -2000 m (blue) to 0 m (white); GL positions (black line) and pinning points (dot) derived from S1 (b-k) and CSK (l-p). The color of dots in (b-p) respectively correspond to the colors of the points in (a).

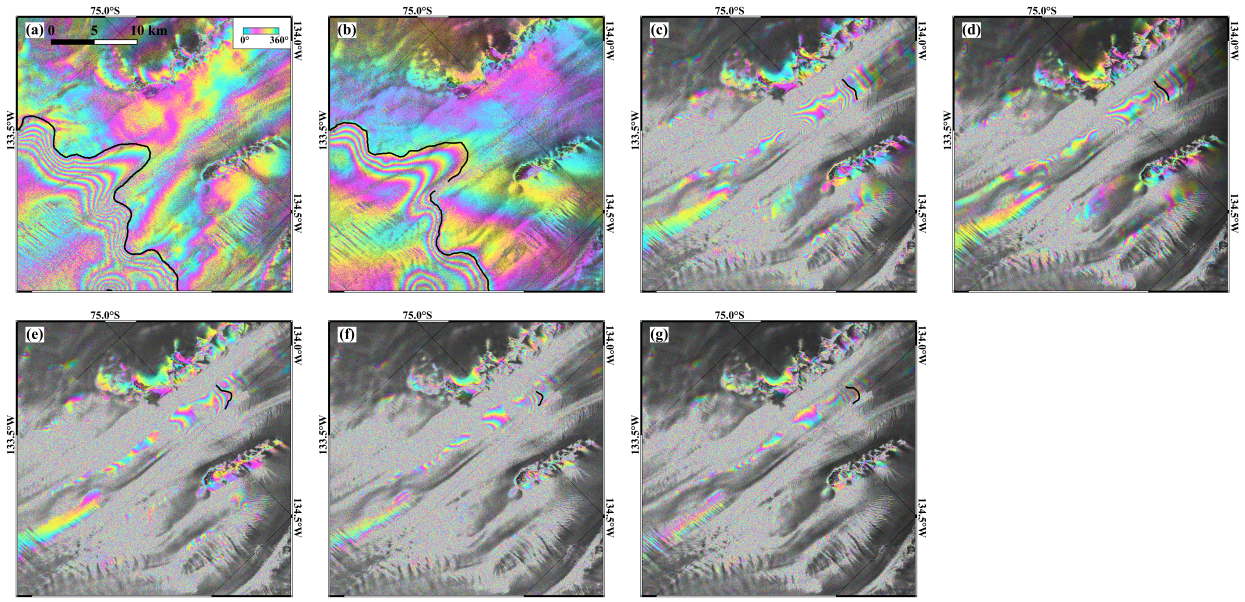


Figure A.8: **Interferograms from ERS-1/2 and ALOS-2 PALSAR.** (a-b) ERS-1/2 interferograms; (c-g) ALOS-2 PALSAR interferograms. Black lines mark GL positions. The information of orbit pairs used by the interferograms and their acquisition times is shown in the following table. The order of the rows from top to bottom in the table corresponds to the subfigure labels in the figure.

Data	Orbit Pairs	Dates
1996a ERS-1/2	23886/4213, 24387/4714	96-02-08/96-02-09, 96-03-14/96-03-15
1996b ERS-1/2	23929/4256, 24430/4757	96-02-11/96-02-12, 96-03-17/96-03-18
2008a ALOS-1	14242/14913, 14913/15584	08-09-26/08-11-11, 08-11-11/08-12-27
2008b ALOS-1	14417/15088, 15088/15759	08-10-08/08-11-23, 08-11-23/09-01-08
2009a ALOS-1	19435/20106, 20106/20777	09-09-17/09-11-02, 09-11-02/09-12-18
2009b ALOS-1	19610/20281, 20281/20952	09-09-29/09-11-14, 09-11-14/09-12-30
2009c ALOS-1	19785/20456, 20456/21127	09-10-11/09-11-26, 09-11-26/10-01-11